



ΠΑΝΕΠΙΣΤΗΜΙΟ
ΠΑΤΡΩΝ
UNIVERSITY OF PATRAS



MSc Program

"Biomedical Engineering"

MSc Thesis

of Evgenia Moustridi

Dipl. Electrical Engineer and Computer Engineer

A.M.: 1079079

*Predictive simulation of single-leg landing scenarios
for ACL injury risk factors evaluation*

Supervisor:

Prof. Moustakas Konstantinos

THESIS NUMBER:

08/02/2022

University of Patras, Electrical and Computer Engineering Department
Evgenia Moustridi
©2022 - All rights reserved

The thesis reports original material developed by Evgenia Moustridi and does not violate Intellectual Property Rights in any way. Reuse of existing material is properly referenced, while potential use of figures, graphs, etc is being reproduced after receiving the respective license from the IPR holder.

Abstract

The Anterior Cruciate Ligament rupture is a very common knee injury during sport activities. Landing after a jump is one of the most prominent human body movement scenarios that can lead to such an injury. The landing - related Anterior Cruciate Ligament (ACL) injury risk factors have been in the spotlight of research interest. Over the years, researchers and clinicians acquire knowledge about human movement during daily - life activities by organizing complex *in vivo* studies using Motion Capture equipment. The recorded motion data are further analyzed to estimate joint angles and forces and provide insight to the functionality and response of internal structures such as soft tissues, ligaments and muscles. Nevertheless, these experiments feature high complexity, costs and technical and most importantly physical challenges. Computational modeling and simulation overcomes all these limitations and allows for studying musculoskeletal systems. Specifically, predictive simulation approaches offer researchers the opportunity to predict and study new biological motions without the demands of acquiring experimental data. In this thesis, we present a pipeline that aims to predict and identify key parameters of interest that are related to ACL injury during single - leg landings. We examined the following conditions of single - leg landing: a) initial landing height, b) hip internal and external rotation, c) lumbar forward - backward leaning, d) lumbar medial - lateral bending, e) lumbar internal - external rotation, f) muscle forces permutations and g) effort goal weight. Identified on related research studies, we evaluated the following risk factors: vertical Ground Reaction Force, knee joint Anterior force, knee joint Abduction moment, and Quadricep / Hamstring force ratio. Our study clearly demonstrated that ACL injury is a rather complicated mechanism with many associated risk factors which are evidently correlated. Nevertheless, our results were mostly in agreement with other research studies regarding the ACL risk factors. Despite the limitations regarding the adopted modeling assumptions, our pipeline clearly showcased promising potential of predictive simulations to evaluate different aspects of complicated phenomena, such as the ACL injury. Therefore, further improvements can lead to the development of a workflow that can be used by physiotherapists and clinicians on adjusting rehabilitation and training plans based on subject - specific characteristics.

Keywords: Anterior Cruciate Ligament, ACL, ACL injury, drop - landing, single - leg landing, predictive simulation, Musculoskeletal modeling, Ground Reaction Forces, GRF, Knee joint Reaction forces

Περίληψη

Η ρήξη του Πρόσθιου Χιαστού Συνδέσμου (ΠΧΣ) είναι πολύ συχνός τραυματισμός της άρθρωσης του γονάτου κατά την διάρκεια αθλητικών δραστηριοτήτων. Η προσγείωση μετά από ένα άλμα είναι μια κίνηση του ανθρώπινου σώματος που μπορεί να οδηγήσει σε τέτοιου είδους τραυματισμό. Οι παράμετροι επικινδυνότητας ρήξης του ΠΧΣ που σχετίζονται με άλματα είναι στο επίκεντρο του ερευνητικού ενδιαφέροντος. Όλα αυτά τα χρόνια, οι ερευνητές και οι κλινικοί γιατροί αποκτούν γνώσεις σχετικά με τις καθημερινές κινήσεις του ανθρώπινου σώματος οργανώνοντας σύνθετες "in vivo" μελέτες με χρήση εξοπλισμού καταγραφής κίνησης. Τα δεδομένα κίνησης αναλύονται περαιτέρω ώστε να εκτιμηθούν οι γωνίες και οι δυνάμεις στις αρθρώσεις παρέχοντας με αυτό τον τρόπο μια εικόνα στη λειτουργία και την απόκριση των εσωτερικών δομών, όπως οι μαλακοί ιστοί, οι σύνδεσμοι και οι μύες. Ωστόσο, αυτά τα πειράματα χαρακτηρίζονται από υψηλή πολυπλοκότητα, και παρουσιάζουν μεγάλο κόστος, σύνθετες τεχνικές και κυρίως φυσικές προκλήσεις. Η υπολογιστική μοντελοποίηση και προσομοίωση επιτρέπει την μελέτη μυοσκελετικών συστημάτων ξεπερνώντας αυτούς τους περιορισμούς. Πιο συγκεκριμένα, οι μέθοδοι προσομοιώσεων με τεχνικές πρόβλεψης προσφέρουν στους ερευνητές την ευκαιρία να προβλέπουν και να μελετούν νέες βιολογικές κινήσεις χωρίς την απαίτηση καταγραφής πειραματικών δεδομένων. Σε αυτή τη διπλωματική παρουσιάζουμε μια μεθοδολογία που στοχεύει στην πρόβλεψη και αναγνώριση βασικών παραμέτρων που σχετίζονται με τραυματισμούς του ΠΧΣ κατά την εκτέλεση προσγειώσεων με ένα πόδι μετά από άλμα. Οι περιπτώσεις προσγείωσης με ένα πόδι που εξετάστηκαν ήταν οι ακόλουθες: α) αρχικό ύψος προσγείωσης, β) εσωτερική και εξωτερική περιστροφή του ισχίου, γ) οσφυϊκή κλίση προς τα εμπρός και προς τα πίσω, δ) οσφυϊκή κλίση προς τα δεξιά και προς τα αριστερά, ε) οσφυϊκή εσωτερική και εξωτερική περιστροφή, στ) μεταβολές μυϊκών δυνάμεων και τέλος ζ) επίπεδο ενεργοποίησης μυών. Βασιζόμενοι σε σχετικές ερευνητικές μελέτες αξιολογήσαμε τις ακόλουθες παραμέτρους κινδύνου: κατακόρυφη δύναμη αντίδρασης εδάφους, πρόσθια δύναμη στην άρθρωση του γονάτου, ροπή απαγωγής της άρθρωσης του γονάτου και λόγος δύναμης τετρακέφαλου μυός / οπίσθιου μηριαίου μυός. Η μελέτη μας έδειξε ξεκάθαρα την περιπλοκότητα του τραυματισμού του ΠΧΣ και την συσχέτιση του με πολλούς παράγοντες κινδύνου τραυματισμού. Παρ' όλα αυτά, τα αποτελέσματα μας ήταν ως επί το πλείστον σε συμφωνία με σχετικές ερευνητικές μελέτες όσον αφορά τους παράγοντες τραυματισμού του ΠΧΣ. Παρά τους περιορισμούς σχετικά με την υιοθετούμενη μοντελοποίηση, η μελέτη μας παρουσίασε υποσχόμενες δυνατότητες προσομοίωσης πρόβλεψης και αξιολόγησης διαφορετικών πτυχών περίπλοκων φαινομένων, όπως αυτό της ρήξης του ΠΧΣ. Περαιτέρω βελτιώσεις μπορούν να οδηγήσουν στην ανάπτυξη ενός εργαλείου που θα μπορεί να χρησιμοποιηθεί από φυσικοθεραπευτές και κλινικούς γιατρούς για την προσαρμογή σχεδίων αποκατάστασης και εκπαίδευσης με βάση συγκεκριμένα χαρακτηριστικά του κάθε υποκειμένου.

Λέξεις κλειδιά: Πρόσθιος Χιαστός, ΠΧΣ, ρήξη ΠΧΣ, προσγείωση, προσομοίωση πρόβλεψης, Δύναμη Αντίδρασης εδάφους, Δυνάμεις Αντίδρασης άρθρωσης

Acknowledgements

First of all, I would like to express my sincere gratitude to my thesis supervisor Prof. Konstantinos Moustakas for his guidance, support and trust for letting me be part of the Visualization and Virtual Reality Group.

Furthermore, I would like to express my gratitude and appreciation to phd candidate Konstantinos Risvas whose guidance, support and encouragement has been invaluable throughout this study.

In addition, I would like to express my acknowledgements to my sister, Maria and friends, for their support and continuous encouragement throughout the years of study and through the process of researching and writing this thesis.

Finally, I am grateful for my parents whose constant love and support keep me motivated and encourage me throughout the years of my studies. This accomplishment would not have been possible without them.

Table of Contents

Abstract	iii
Acknowledgements	v
1 Introduction	1
1.1 Thesis contribution	4
1.2 Thesis structure	5
2 Theoretical Background of Related Concepts	7
2.1 Lower - limb anatomy and biomechanics	7
2.1.1 Hip joint	9
2.1.2 Knee joint	9
2.1.3 Ankle joint	11
2.2 Muscle physiology, architecture and dynamics	11
2.3 ACL biomechanics, injury and treatment	15
2.3.1 Drop - Landing and potential ACL injury	17
2.4 Mathematics and physics concepts	18
2.4.1 Multibody dynamics	19
2.4.2 Trajectory Optimization problems	19
2.4.2.1 Shooting methods	20
2.4.2.2 Collocation methods	22
2.5 Literature Review	24
2.5.1 Landing height	24
2.5.2 Lower extremity alignment	25
2.5.3 Trunk orientation	27
2.5.4 Knee joint surrounding muscles	28
3 Methods	30
3.1 Dependencies	31
3.1.1 The OpenSim software	31
3.1.1.1 OpenSim models	33
3.1.2 The SCONE software	37
3.1.2.1 Objective functions	39
3.1.3 The MOCO tool	40
3.1.3.1 Objective functions	42
3.2 Predictive simulation of landing with SCONE	42
3.2.1 Simulation setup	42
3.3 Predictive simulation of landing with MOCO	44

3.3.1	Simulation setup	44
3.3.1.1	Model operations	45
3.3.1.2	Augmenting model complexity - MocoTrack	45
3.3.1.3	Predictive simulation settings - MocoStudy	47
3.3.1.4	Post - processing operations	47
3.3.2	Initial height case study	49
3.3.3	Hip rotation case study	50
3.3.4	Trunk orientation case study	52
3.3.5	Muscle force of knee joint agonists and antagonists case study	55
3.3.6	Moco Control goal weight case study	56
4	Results	57
4.1	Initial height case	57
4.2	Hip rotation case	61
4.3	Trunk orientation case	68
4.3.1	Trunk forward - backward leaning	68
4.3.2	Trunk medial - lateral bending	74
4.3.3	Trunk internal - external rotation	80
4.4	Muscle force of knee joint agonists and antagonists case	86
4.5	Moco Control goal weight case	89
5	Discussion	93
5.1	Initial height case	93
5.2	Hip rotation case	94
5.3	Trunk orientation case	95
5.4	Muscle force of knee joint agonists and antagonists case	96
5.5	Moco Control goal weight case	97
6	Conclusions	98
	Bibliography	100

List of Figures

1.1	Left: ACL rupture. Right: ACL rupture during change of direction.	1
1.2	Left: Inertial Measurement Units (IMUs). Right: Optical Motion Capture (mocap).	2
1.3	Visualization front-end composed of a musculoskeletal visualizer, real - time plotting, and footprint visualization. Reproduced from (Stanev et al., 2021).	3

2.1	The anatomical position, with the three reference planes and six fundamental directions. Reproduced from (Musculoskeletal Key 2016).	8
2.2	Anatomy and physiology of the lower human body. Reproduced from (HowToRelief 2021b ; Lower limb anatomy 2021c).	8
2.3	Presentation of hip joint Degrees of Freedom (DoFs). Reproduced from (Smith, Biery, and Gregor, 1990).	9
2.4	Presentation of knee joint DoFs. Reproduced from (BioDigital 2020a).	10
2.5	Overview of the knee anatomy. Reproduced from (JohnsHopkinsMedicine 2021d).	10
2.6	Ankle joint movements in three orthogonal planes. Reproduced from (Alcocer et al., 2012).	11
2.7	Hierarchical structure of skeletal muscle. Reproduced from (Thomas K. Uchida, 2021).	12
2.8	The active, passive and total force - length curves. The peak of active force F_o^M happens at the optimal fiber length l_o^M . Reproduced from (Thomas K. Uchida, 2021).	13
2.9	Muscle fiber force (left) and power (right) as functions of fiber velocity. Reproduced from (Thomas K. Uchida, 2021).	14
2.10	The Hill - type model of muscle - tendon complex. Reproduced from (Anderson and Pandy, 1999).	14
2.11	A computational model of activation dynamics that relates excitation (u(t)) to activation (a(t)). Reproduced from (Thomas K. Uchida, 2021)	15
2.12	The anterior cruciate ligament (ACL) is one of the key ligaments that help stabilize the knee joint. The ACL connects the femur to the tibia. Reproduced from (MayoClinic 2021a)	16
2.13	Mechanism of ACL rupture during change of direction. An increased injury is introduced with the foot planted, knee externally rotated or in valgus position and a varus or internal moment is applied. Reproduced from (Peter Brukner, 2016).	16
2.14	Representation of a drop - landing and displacement of the center of mass. The landing phase is considered from foot strike to the time instant of maximum knee flexion angle. The landing phase begins from the drop and ends at the end of collision stage. Reproduced from (Skinner, Zelik, and Kuo, 2015)	17
2.15	Single - Shooting and Multiple - Shooting methods. Reproduced from (Kelly, 2017b).	21
2.16	Feasible (left) and optimal (right) trajectories for a simple movement of a block using direct collocation method. Reproduced from (Kelly, 2017a).	23
3.1	Overview of the proposed simulation pipeline of this thesis. In the first layer, the implemented methods and software tools used in this thesis are presented. Next, in the second layer all the examined scenarios are introduced and finally in the third layer, the exported results are presented.	30

3.2	A joint connects two rigid body reference frames and is used to define the kinematic relationship between the rigid bodies. Reproduced from (SimTK - confluence 2011a).	32
3.3	The musculoskeletal model developed by Ajay Seth used for the predictive simulation of single - leg landing in SCONE. It has 9 DoFs and contact spheres to estimate Ground Reaction Forces (GRF).	33
3.4	"Gait2392" and "Gait2354" OpenSim musculoskeletal models used for the simulations conducted in Moco. Both models were developed by Darryl Thelen, Ajay Seth, Frank C. Anderson, and Scott L. Delp, used for the predictive simulation of single-leg landing in Moco.	34
3.5	Location of the body - segmental reference frames. Reproduced from (Delp et al., 1990)	35
3.6	Geometry of the knee. Reproduced from (Delp et al., 1990).	36
3.7	Schematic diagram of the musculoskeletal model with only the left side muscles. Foot - ground contact was modeled with five contact spheres per foot.	37
3.8	Overview of OpenSim Moco. It produces the optimal motion and muscle behavior for an OpenSim musculoskeletal model, given goals to achieve during the motion and/or reference data. Reproduced from (Dembia et al., 2020).	40
3.9	Organization of basic Moco classes. Overview of MocoStudy. Reproduced from (Dembia et al., 2020).	41
3.9	Initial state of the musculoskeletal model "Human0916" used for the predictive simulations in SCONE. Sagittal (right) and Frontal (left) planes.	43
3.10	Computation of the Center of Pressure. Reproduced by (YH, n.d.).	48
3.11	True origin of the Center of Pressure (CoP). Reproduced by (YH, n.d.).	49
3.12	Initial state of the model for different drop - landing heights.	50
3.13	Initial state of the model for 0°, 10°, 20° and 30° of hip internal rotation.	51
3.14	Initial state of the model for 0°, 10°, 20° and 30° of hip external rotation.	51
3.15	Initial state of the OpenSim model for different values of lumbar flexion - extension.	53
3.16	Initial state of the OpenSim model for different values of lumbar right - left bending.	54
3.17	Initial state of the OpenSim model for different values of lumbar internal - external rotation.	54
4.1	Hip, knee and ankle kinematics for the initial height case.	58
4.2	GRF and Ground Reaction Moments (GRM) for the initial height case study.	58
4.3	Knee joint Joint Reaction Forces (JRF) and Joint Reaction Moments (JRM) for multiple drop - landing heights.	59

4.4	Muscle forces and muscle force ratios for multiple drop - landing heights.	60
4.5	Hip, knee and ankle kinematics for various hip internal rotation angles.	62
4.6	GRF and GRM for various hip internal rotation angles.	62
4.7	Knee joint JRF and JRM for various hip internal rotation angles.	63
4.8	Muscle forces and muscle force ratios for various hip internal rotation angles.	64
4.9	Hip, knee and ankle kinematics for various hip external rotation angles.	65
4.10	GRF and GRM for various hip external rotation angles.	66
4.11	Knee Joint Reaction Forces (kJRF) and Knee Joint Reaction Moments (kJRM) for various hip external rotation angles.	66
4.12	Muscle forces and muscle force ratios for various hip external rotation angles.	67
4.13	Hip, knee and ankle kinematics for multiple lumbar flexion angles.	68
4.14	GRF and GRM for multiple lumbar flexion angles.	69
4.15	Knee joint JRF and JRM for multiple lumbar flexion angles.	70
4.16	Muscle forces and muscle force ratios for multiple lumbar flexion angle s.	70
4.17	Hip, knee and ankle kinematics for multiple lumbar extension angles.	72
4.18	GRF and GRM for multiple lumbar extension angles.	72
4.19	Knee joint JRF and JRM for multiple lumbar extension angles.	73
4.20	Muscle forces and muscle force ratios for multiple lumbar extension angles.	73
4.21	Hip, knee and ankle kinematics for multiple trunk right bending angles.	75
4.22	GRF and GRM for multiple trunk right bending angles.	75
4.23	Knee joint JRF and JRM for multiple trunk right bending angles.	76
4.24	Muscle forces and muscle force ratios for multiple trunk right bending angles.	76
4.25	Hip, knee and ankle kinematics for multiple trunk left bending angles.	77
4.26	GRF and GRM for multiple trunk left bending angles.	78
4.27	Knee joint JRF and JRM for multiple trunk left bending angles.	79
4.28	Muscle forces and muscle force ratios for multiple trunk left bending angles.	79
4.29	Hip, knee and ankle kinematics for multiple trunk internal rotation angles.	80
4.30	GRF and GRM for multiple trunk internal rotation angles.	81
4.31	Knee joint JRF and JRM for multiple trunk internal rotation angles.	81
4.32	Muscle forces and muscle force ratios for multiple trunk internal rotation angles.	82

4.33	Hip, knee and ankle kinematics for multiple trunk external rotation angles.	83
4.34	GRF and GRM for multiple trunk external rotation angles. . .	84
4.35	Knee joint JRF and JRM for multiple trunk external rotation angles.	84
4.36	Muscle forces and muscle force ratios for multiple trunk external rotation angles.	85
4.37	Hip, knee and ankle kinematics for scenarios of normal, weak and strong knee joint agonist antagonist muscles.	86
4.38	GRF and GRM for scenarios of normal, weak and strong knee joint agonist antagonist muscles.	87
4.39	Knee joint JRF and JRM for scenarios of normal, weak and strong knee joint agonist antagonist muscles.	87
4.40	Muscle forces and muscle force ratios for scenarios of normal, weak and strong knee joint agonist antagonist muscles.	88
4.41	Hip, knee and ankle kinematics for different weights of Moco Control goal.	89
4.42	GRF and GRM for different weights of Moco Control goal. . .	90
4.43	Knee joint JRF and JRM for different weights of Moco Control goal.	90
4.44	Muscle forces and muscle force ratios for different weights of Moco Control goal.	91

List of Tables

3.1	Bounds for the DoFs of Gait2354 and Gait2392 OpenSim models for MOCO Track tool.	46
3.2	Moco values for <i>pelvis_ty</i> based on landing height as displayed in OpenSim.	50
3.3	Overview of investigated values for hip joint rotation.	51
3.4	Values for DoFs of the model for different values of left hip rotation scenarios	52
3.5	Overview of investigated values for lumbar joint DoFs. We also describe the bounds for each value.	53
3.6	Bounds for the DoFs of the model for the trunk orientation case study.	55
3.7	Values for max isometric force for all muscles in hamstrings and gastrocnemius muscle groups. Also, the modified max isometric forces for these muscles for their strengthening or weakening are included.	56
3.8	Demonstration of the eight cases with different combinations of normal, weak and strong muscles.	56

4.22 Knee joint JRF and JRM at the time instant of peak vGRF for
different weights of Moco Control goal. 92

Acronyms

2D 2 - Dimensional. 37

3D 3 - Dimensional. 26–28, 33, 37

AbdM Abduction moment. iii, 26, 58, 60, 63, 64, 69, 71, 72, 74, 75, 77, 78, 82, 87, 88, 90, 92, 93, 95–99

ACL Anterior Cruciate Ligament. iii, vii, 1, 2, 4–7, 10, 15–18, 24–28, 30, 55, 57, 93–96, 98, 99

AddM Adduction moment. 26, 67, 72, 75, 95

AF Anterior force. iii, 58, 60, 62, 67, 69, 71, 72, 74, 75, 77, 78, 82, 85, 88, 90, 92–99

BW Body Weight. 57, 62, 91, 93, 95–97

CF Compressive force. 58, 60, 62, 63, 66, 69, 71, 72, 74, 75, 78, 79, 81, 82, 84, 85, 87, 92, 93, 96, 97

COM Center of Mass. 39

CoP Center of Pressure. ix, 47–49, 99

DoF Degree of Freedom. 31, 34, 35, 43, 99

DoFs Degrees of Freedom. viii, ix, xi, 9, 10, 28, 33, 43, 45, 46, 50–53, 55–57, 61

EM Extension moment. 26

EMG Electromyography. 4, 25–27, 95

ERM External rotation moment. 58, 63, 66, 69, 72, 75, 92, 95, 99

FD Forward Kinematics. 3

FE Finite Element. 3

FEA Finite Element Analysis. 3

FEM Finite Element Method. 3

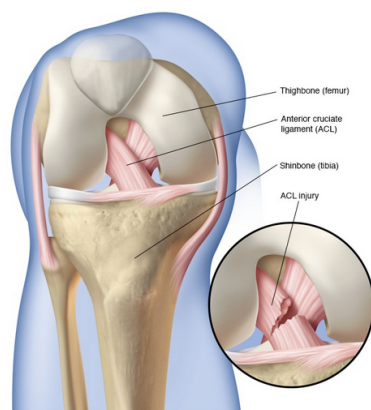
FM Flexion moment. 59, 60, 63

- GRF** Ground Reaction Forces. ix–xii, 6, 17, 18, 24–28, 33, 43, 47, 48, 55, 57, 58, 60, 62, 64–67, 69, 71, 72, 74, 75, 77, 78, 80–91, 93–97
- GRM** Ground Reaction Moments. ix–xi, 6, 57, 58, 62, 65, 66, 69, 72, 75, 78, 80, 81, 83, 84, 86, 87, 89, 90
- GTA force ratio** Gastrocnemius / Tibialis Anterior force ratio. xii, 59, 60, 64, 66, 67, 70, 71, 74, 77, 80, 82, 85, 88, 91, 97
- ID** Inverse Dynamics. 3
- IGC** Initial Ground Contact. 26–28, 58, 59, 61, 72, 75, 87, 93
- IK** Inverse Kinematics. 25, 32
- IRM** Internal rotation moment. 26, 59, 60, 64, 67, 72, 75, 78, 82, 87, 92, 95, 96
- JRA** Joint Reaction Analysis. 32, 47, 98
- JRF** Joint Reaction Forces. ix–xiii, 6, 58, 59, 61, 63, 65, 68, 70, 71, 73, 74, 76, 77, 79–81, 83, 84, 86, 87, 89, 90, 92
- JRM** Joint Reaction Moments. ix–xiii, 6, 57–59, 61, 63, 65, 68, 70, 71, 73, 74, 76, 77, 79–81, 83, 84, 86, 87, 89, 90, 92
- kJRF** Knee Joint Reaction Forces. x, 47, 57, 62, 64, 66, 69, 72, 75, 78, 81, 82, 84, 87, 90, 95
- kJRM** Knee Joint Reaction Moments. x, 47, 57, 62, 66, 69, 72, 75, 78, 81, 82, 84, 87, 90
- LCL** Lateral Collateral Ligament. 10
- MCL** Medial Collateral Ligament. 10
- MF** Medial force. 58, 88, 92, 93, 95
- MoCap** Motion Capture. iii, 3, 4, 26–28, 31
- PCL** Posterior Cruciate Ligament. 10
- pGRF** posterior Ground Reaction Force. 27, 58, 60, 62, 69, 72, 73, 75, 78, 81, 82, 89, 95
- Q/H force ratio** Quadriceps / Hamstring force ratio. iii, xii, 24, 59, 60, 63, 64, 66, 67, 70, 71, 73, 74, 76, 77, 79, 80, 82, 84, 85, 88, 91, 94–98
- RRA** Residual Reduction Algorithm. 25
- SO** Static Optimization. 25, 32
- vGRF** vertical Ground Reaction Force. iii, xii, xiii, 6, 24–27, 57–83, 85–99

Chapter 1

Introduction

The knee joint anatomical structure is one of the most complex human body joints. Its stability and functionality during daily life activities are maintained mainly by the articulations, ligaments, menisci and muscle forces. Among the knee joint ligaments, ACL is of prominent importance as it acts as a stabilizer by restricting excessive posterior and anterior knee displacement during dynamic movements. This is the reason why ACL rupture is one of the most common knee injuries in competitive sports activities, like football, basketball, or skiing (Figure 1.1a) (Prodromos et al., 2008). These sports involve movement patterns of high risk, such as sudden stops, abrupt changes of direction, landing after a jump and deceleration before changing direction (Sugimoto et al., 2014; Boden et al., 2000). These are labeled as non - contact ACL injury conditions (Figure 1.1b). However, injuries of the ACL can also happen when direct contact with another athlete takes place, although only 1/3 of the total ACL injuries occur due to direct contact (Mokhtarzadeh et al., 2017; Bulat et al., 2019).



(a) ACL rupture representation. Reproduced from (MayoClinic 2021a).

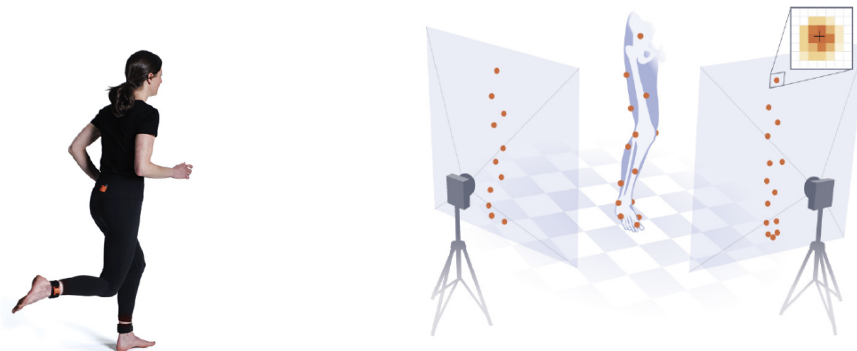


(b) Mechanism of ACL rupture during change of direction. An increased injury is introduced with the foot planted, knee externally rotated or in valgus position and a varus or internal moment is applied. Reproduced from (Peter Brukner, 2016).

FIGURE 1.1: Left: ACL rupture. Right: ACL rupture during change of direction.

In general, ACL injury involves a complete or partial ligament tear. This condition as well as the desired post injury activity levels affect the chosen

treatment procedure. Typically, there are two main approaches. The first option involves a basic rehabilitation plan including physiotherapy and bracing support. However, this option requires low levels of activity in the future. On the other hand, if high levels of activity are desired, surgery for ACL restoration is unavoidable. This procedure named as "ACL reconstruction" has emerged as the golden standard approach when it comes to ACL injuries (Looney et al., 2020). It requires replacement of the ligament by a tendon graft extracted by the same patient or a donor. Also, artificial grafts can be used. Post - surgery, rehabilitation strategies involve muscle strengthening and gradual restoration of knee motion range. A post - effect of a complete ACL tear is the higher risk of osteoarthritis development on the knee cartilage, especially when the meniscus is also damaged (Monk et al., 2014). ACL reconstruction is a complex surgery that depends on a plethora of parameters and requires long periods of rehabilitation, that can span a 6 - 12 month range (Kvist, 2004; Goes et al., 2020). Moreover, graft failures are common and full restoration of knee kinematics is not always achievable. Therefore, complete and accurate knowledge regarding knee joint biomechanics is crucial to develop training strategies that aim to limit ACL injury risk or assist surgery and rehabilitation plans post - injury.



(a) Inertial measurement units, the orange sensors measure linear accelerations and angular velocities.

Reproduced from (Thomas K. Uchida, 2021)

(b) Optical motion capture (mocap) is a technique for estimating the motion of the underlying skeleton from the trajectories of points on the skin.

Reproduced from (Thomas K. Uchida, 2021)

FIGURE 1.2: Left: Inertial Measurement Units (IMUs). Right: Optical Motion Capture (mocap).

Traditionally, researchers and clinicians acquire knowledge about human movement during daily - life activities by organizing complex *in vivo* studies. However, these experiments feature high complexity, costs and technical and physical challenges. Particularly in potentially precarious dynamic movements, such as landing, ethical issues may arise that can restrain the availability of participants in these scenarios. These limitations and uncertainties gave prominence to computational modeling and simulation as a competent tool at the disposal of biomechanics professional and research community when studying musculoskeletal systems, especially with the rapidly increased

computational power that significantly reduces time of numerical studies' execution.

In the most common approach, biomechanical studies usually require human motion data that are recorded using dedicated equipment. Examples of such devices are mobile sensors (Inertial Measurement Units or IMUs) and Motion Capture (MoCap) equipment using video technologies and retro-reflective markers [Figure 1.2](#). The recorded data are further analyzed using software to estimate joint angles and forces. That way researchers gain insight into the functionality and response of internal structures such as soft tissues, ligaments and muscles. Estimation of these kinematic and kinetic parameters is also achievable with real - time biofeedback as can be seen in [Figure 1.3](#) (Stanev et al., [2021](#)).

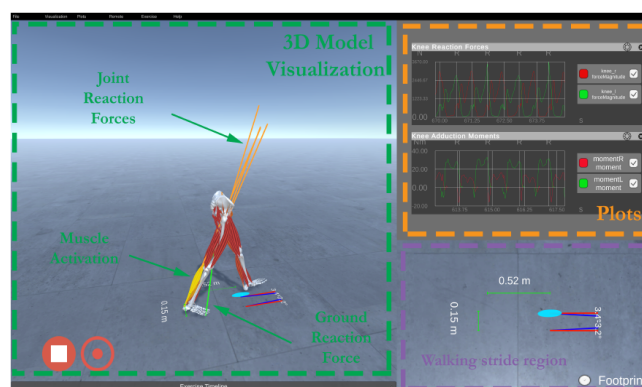


FIGURE 1.3: Visualization front-end composed of a musculoskeletal visualizer, real - time plotting, and footprint visualization. Reproduced from (Stanev et al., [2021](#)).

An integral part of a standard biomechanics analysis is the development of computer models that mathematically describe all the aspects of the physical systems that they represent. The response of these models is numerically evaluated by applying rigid body dynamics, Finite Element Method (FEM) or computational fluid dynamics (CFD) depending on the phenomena under consideration (Engel, Herpers, and Hartmann, [2011](#)).

Usually, rigid body dynamics are applied to study musculoskeletal system on a high - level through estimation of forces at a certain number of body points or joints. The musculoskeletal system is modeled as rigid bodies in series linked together by joints that represent real life articulation. In clinical practice, the main methods regarding multi-body systems are the Inverse Dynamics (ID) and the Forward Kinematics (FD) methods. ID analysis starts from the movement (effect) and computes the muscle excitation signals (cause), while in FD analysis the muscles are triggered and the resultant movement is estimated (Stanev and Moustakas, [2015](#)). On the other hand, when detailed response of anatomical structures is demanded, Finite Element (FE) models are more suitable, since they allow for body deformation evaluation and estimation of stress. Finite Element Analysis (FEA) allows to capture the geometry and material effects on the response of the anatomical structures (Benos et al., [2020](#); Naghibi et al., [2020](#)). Combining these two approaches is also a common route for researchers (Kłodowski et al., [2015](#)).

Examples of biomechanics application fields using multi-body systems are neuromuscular pathologies, study of muscle coordination and surgery modeling and simulation. Regarding neuromuscular pathologies, multiple research studies examine the analysis of human motion dynamics, and especially gait, to obtain biometric features through which disturbances can be observed from normal and abnormal motion patterns (Nandy and Chakraborty, 2017; Akbas, Sulzer, and Neptune, 2018; Arnold et al., 2006). Furthermore, muscle redundancy is a common biomechanics research topic where scientists attempt to investigate the muscle contribution in each movement considering that there exist infinitely many solutions for muscle forces resulting in identical movement (Stanev and Moustakas, 2019b). Many research studies focus on modifying and improving the developed algorithms of efficient computation of these parameters (Stanev and Moustakas, 2018; Stanev and Moustakas, 2019a). Finally, biomechanics are also applied to model and simulate surgery procedures aiming to develop assisting tools and treatment plans (Stanev et al., 2015). In general, all these studies require experimental data, such as MoCap and biosensor measurements (Electromyography (EMG), or sensor implants). Therefore the demands of "state of the art" technology facilities, equipment and complex experimental setups with multiple trials is unavoidable.

In an attempt to overcome these challenges, predictive simulation approaches have emerged as a valuable counterpart to MoCap equipment that offer researchers the opportunity to predict new motions without the demands of acquiring experimental data. These modern simulation approaches as part of the trajectory optimization domain allow researchers to generate and study new biological motions. That way, predominant factors that can cause injuries can be identified and determined overcoming the necessity of real experiments. Predictive simulations can be utilized to provide answers in multiple and repeated what-if scenarios that would require laborious and demanding experimental setups. The outcomes of predictive subject-specific simulations can be used as the scaffold of personalized treatment plans to improve medical therapy and rehabilitation. Moreover, physiotherapists and clinicians can organize retraining procedures such as muscle strengthening and posture improvement to minimize injury risk factors. Finally, prototypes of assistive devices can be assessed to improve their functionality in minimizing injury risk factors.

In this thesis, we use biomechanics tailored trajectory prediction tools to generate a single-leg landing motion and study what-if scenarios that can potentially contribute to an ACL rupture. This is accomplished by evaluating permutations of body posture, individual muscle forces and simulations settings.

1.1 Thesis contribution

In this work, we propose a predictive simulation approach that allows prediction of a single-leg landing motion without using experimental data. The aim of the workflow is to perform multiple case studies of single-leg landings, compare them and identify factors that could contribute to an ACL injury.

In more detail, our analysis is divided in three main parts. First, we predict the motion of a single - leg landing using the SCONE software with a simplified OpenSim model. Then, we track that motion using a more complex OpenSim model and the Moco tool. Finally, we predict multiple single - leg landing motions using MOCO tool, a more complex model and the previously tracked motion as an initial guess. The examined case studies are divided in five main categories. First, we predict landings from six different initial heights. Then we predict single - leg landings with different hip rotation angles. Also, we predict drop - landings with deviations on the trunk orientation, and in particular the following cases: lumbar flexion - extension, lumbar medial - lateral bending and internal - external rotation. Furthermore, we predict single - leg landings with different combinations of knee joint agonist and antagonist muscle forces. Finally, we examine the effect of an effort goal on the results of the analysis since knee stability during single - leg landing can be affected by muscle forces and proprioception.

The presented pipeline offered us an insight into the parameters associated with ACL injuries during single - leg landings which was the main objective. For all case studies we were able to compare numerous parameters that are related to increased ACL injury risk based on thorough literature review of similar research studies. Moreover, when comparing these risk factors we clearly witnessed and showcased their high correlation.

The primary objective of the work presented in this thesis was to lay the technical framework that can allow the easy setup of multiple case studies for evaluating single - leg landings to answer what - if scenarios of our interest. Capitalizing on this, we consider that our work offers multiple additional assets. First, changing the data of the musculoskeletal model can be easily done through the OpenSim interface and allow for subject - specific simulations. This is crucial for identifying or simulating pathological conditions such as muscle weakening following an injury. Furthermore, modifications of the foot - contact modeling setup can support different settings such as inclined landing planes or material properties for footwear.

We envision that the presented pipeline could be used by physiotherapists and clinicians on adjusting rehabilitation, training plans and an overall improve in medical therapy.

1.2 Thesis structure

The next chapters of the presented thesis are organized in the following way:

In **Chapter 2** we introduce the anatomy and biomechanics of the lower - limb, following by a description of the muscle physiology, architecture and dynamics. Then, we present basic concepts of ACL injuries during dynamic movements like drop - landings and associated parameters. Finally, we make a high - level description of mathematical and physic concepts, such as multi - body dynamics and optimization strategies.

In **Chapter 3**, we describe the methods of this thesis. First, we present a description of the musculoskeletal models and the applied modifications. Then, we present the simulations run in SCONE in order to create an initial

predicted motion of a single - leg landing. Finally, the simulations conducted using OpenSim MOCO are described. Information about all studied scenarios are thoroughly described.

In **Chapter 4**, we present results for the investigated scenarios. For every case, we showcase the following parameters of evaluation: GRF, GRM, JRF, JRM, muscle forces and muscle force ratios. The results are analyzed and presented using intuitive plots for the entire motion and tables with values at time of peak vGRF.

In **Chapter 5**, we discuss the findings of our study and compare them by referencing the ACL risk factors pointed out by similar research studies in literature.

Finally, in **Conclusions**, the overall conclusions of the thesis, limitations and possible future directions are presented.

Chapter 2

Theoretical Background of Related Concepts

In this chapter, a theoretical background of the related to our study concepts is provided. First, we present a general description of the lower limb anatomy and muscle physiology. Additionally, we outline the risk factors of ACL injury in an effort to meticulously depict the involved mechanisms. Finally, we attempt a brief introduction into multi - body dynamics and methods of trajectory optimization that are the main mathematical tools deployed throughout this work.

2.1 Lower - limb anatomy and biomechanics

In this section, we describe fundamental material regarding the anatomy, physiology and biomechanics of the lower human body. First, the anatomy of the relevant joints is presented, with specific focus on the knee joint and the involved ligaments. We also briefly describe the muscles that span the knee and provide an insight to muscle physiology and basic concepts of force generation. Moreover, to describe human body posture and understand the relative configuration between different bodies we use the notation of reference planes and directions presented in [Figure 2.1](#). Particularly, we denote the sagittal, transverse and frontal planes. Also, six fundamental directions are described: the superior - inferior, anterior - posterior, and lateral - medial (or contra - lateral).

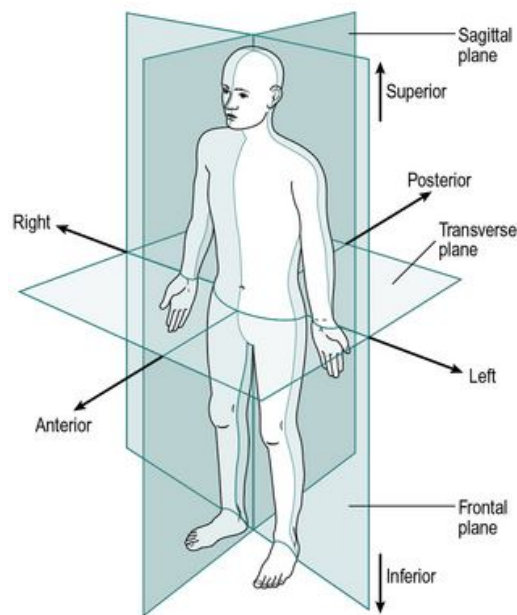
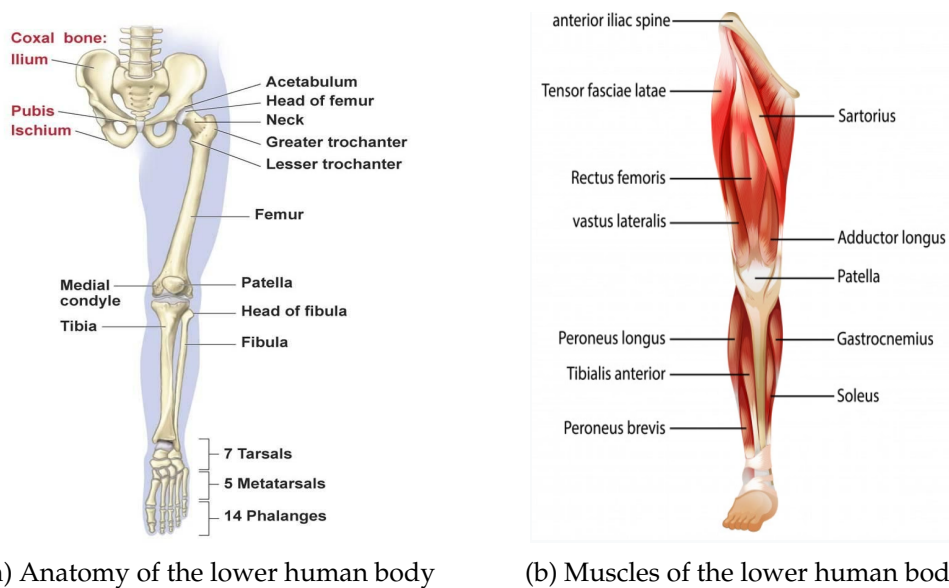


FIGURE 2.1: The anatomical position, with the three reference planes and six fundamental directions. Reproduced from (Musculoskeletal Key 2016).

The lower extremity consists of the pelvis, femur, patella, tibia, fibula and the foot bones. These are connected through the hip, knee and ankle joints, each one featuring its own functionality and allowing for complex movement patterns, rotations and / or translations. These motions are coordinated by the central nervous system which orchestrates the activation of the muscles that span these joints. An overview of the key anatomical structures is presented in Figure 2.2.



(a) Anatomy of the lower human body

(b) Muscles of the lower human body

FIGURE 2.2: Anatomy and physiology of the lower human body. Reproduced from (HowToRelief 2021b; Lower limb anatomy 2021c).

2.1.1 Hip joint

The hip joint connects the pelvis and femur bones and allows three rotational DoFs, namely flexion - extension, abduction - adduction, and internal - external rotation as shown in Figure 2.3.

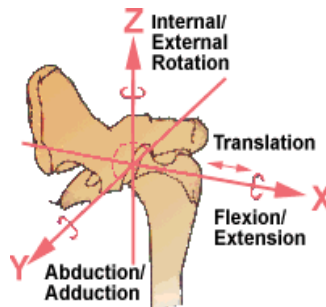


FIGURE 2.3: Presentation of hip joint DoFs. Reproduced from (Smith, Biery, and Gregor, 1990).

2.1.2 Knee joint

The knee joint comprises of two distinct joints, namely the tibio - femoral and patello - femoral joint, which work in conjunction to generate smooth and efficient knee movement. The joint names are derived by the bones that these connect. The tibio - femoral joint provide six DoFs, three relative translations (compression - distraction, anterior - posterior and medial - lateral translation) and three rotations (flexion - extension, internal - external rotation, and varus - valgus rotation) between the femur and tibia bones as depicted in Figure 2.4. Physiological ranges for the rotational motions are $3^\circ - 155^\circ$ for flexion - extension, $6^\circ - 8^\circ$ for varus - valgus and $25^\circ - 30^\circ$ of internal - external rotation when the knee is flexed. Regarding translations, the anterior - posterior translation range is 5 - 10mm, medial - lateral is 1 - 2mm and compression-distraction is 2 - 5mm (Bone and Spine 2019a).

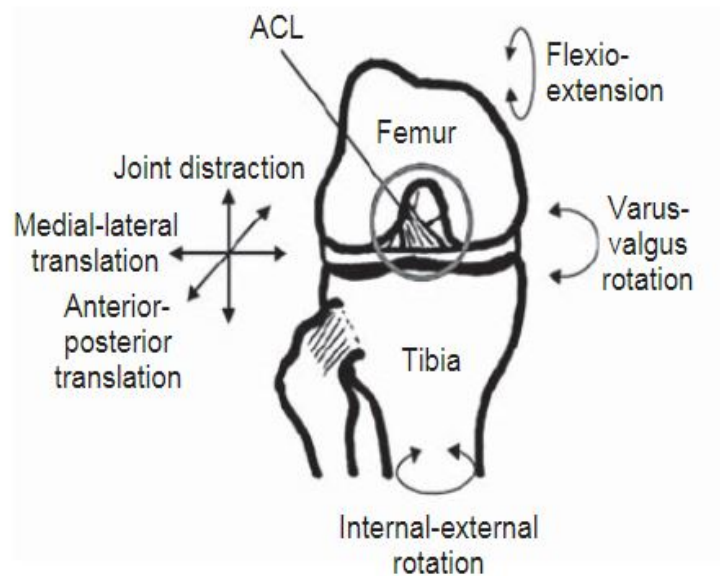


FIGURE 2.4: Presentation of knee joint DoFs. Reproduced from (BioDigital 2020a).

Joint motion is dictated by muscles that span the knee articulation. The extensor muscles are the quadriceps and the flexors are the gastrocnemius, sartorius, popliteus, biceps femoris, semitendinosus and semimembranosus muscles. The role of the knee ligaments is fundamental in restraining the knee motion inside the above mentioned physiological limits by counterbalancing muscle - generated forces. An overview of the knee anatomical structures is presented in Figure 2.5.

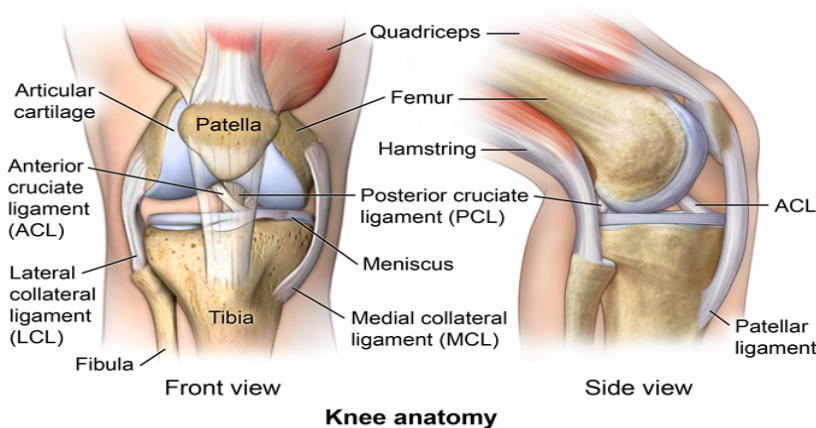


FIGURE 2.5: Overview of the knee anatomy. Reproduced from (JohnsHopkins-Medicine 2021d).

Furthermore, the knee joint is surrounded by ligaments that are elastic bands of connecting tissue. Their main functionality is to act as stabilizers by restricting the anterior - posterior and varus - valgus knee forces and moments. The main ligaments are the ACL, Posterior Cruciate Ligament (PCL), Medial Collateral Ligament (MCL) and the Lateral Collateral Ligament (LCL). Additional ligaments that play a supportive stabilizing role are the

anterolateral ligament, the popliteal and meniscofemoral ligaments and the ligaments of the posterior capsule.

2.1.3 Ankle joint

The ankle joint connects the shank and fibula with the talus bone and allows for plantar - flexion and dorsi - flexion, inversion - eversion, and internal - external rotation Figure 2.6.

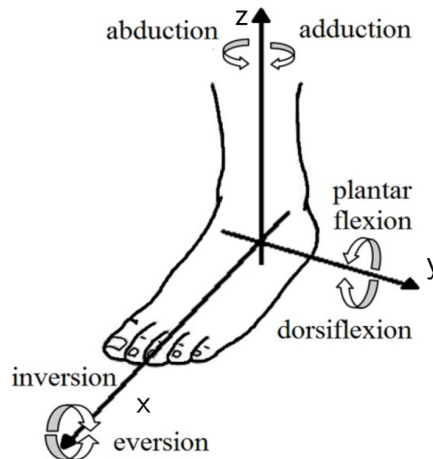


FIGURE 2.6: Ankle joint movements in three orthogonal planes. Reproduced from (Alcocer et al., 2012).

2.2 Muscle physiology, architecture and dynamics

In this section we present the fundamental theoretical concepts about muscle physiology. A brief description of the structure and function of skeletal muscles is necessary to clearly comprehend how motion is generated. An overview of the muscle structures and their hierarchical organization is presented in Figure 2.7.

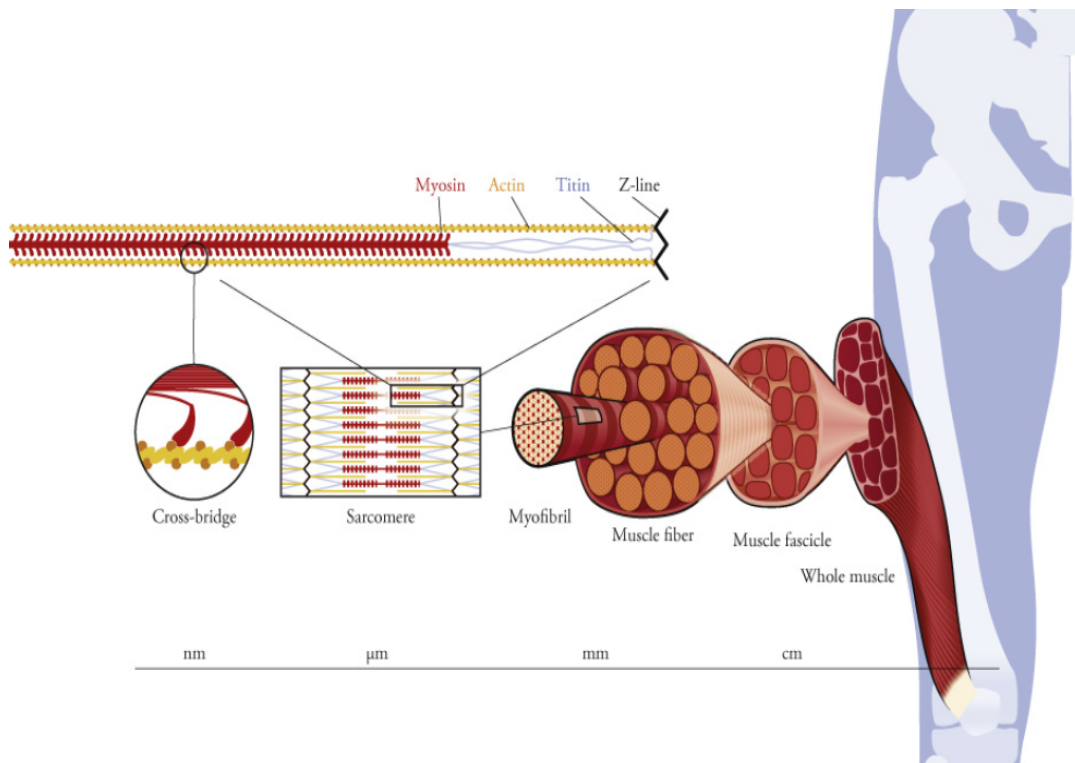


FIGURE 2.7: Hierarchical structure of skeletal muscle. Reproduced from (Thomas K. Uchida, 2021).

By inspecting this figure from right to left we can see that the muscles are connected to bones via tendons on both ends. Tendons are responsible for storing and releasing energy and act as transmitters of muscle forces. As a whole, a muscle is formed by packed muscle fascicles that are shaped by arranged packs of muscle fibers (or myocytes). Subsequently, these comprise of multiple parallel myofibrils that are composed of the fundamental force generating units of a muscle, the sarcomeres. The sarcomeres are linked in parallel or are packed in series. Muscle forces are generated in this lowest level of muscle structure, mainly by two proteins. These are actin and myosin and they are arranged in parallel to form the cross - bridges, areas of a sarcomere where these two proteins are linked. The length of these cross bridges affects the muscle force generation. A single muscle is capable of generating force of thousands of newtons during its contraction, but this force is generated by the summation of small peconewtons of force produced by its motors at the molecular level (myosin). It should be mentioned that in order for a muscle to generate force, it needs to be activated by the central nervous system that coordinates the action of trillions of actin and myosin proteins.

The main parameters of a muscle are its optimal fiber length, the muscle fiber pennation angle at optimal fiber length, its maximum isometric force, its maximum contraction velocity and the tendon slack length. In Figure 2.8 the force - length curve is presented describing the active, passive and total force. The optimal length l_0^S is the length at which the sarcomere develops its peak isometric force, F_0^M . This force is generated when a muscle is at its optimal fiber length and fully activated. In daily life activities, this parameter is tough

to measure and our knowledge is based on cadaver and animal experiments. The fiber optimal length l_0^M is accomplished when the sacromere reaches its optimal length and is equal to $l_0^M = nl_0^S$, if we assume equal length of all sacromeres, and n is the number of sacromeres that form a muscle fiber.

Moreover, the force - length curve is characterized by three different regions. The first is the ascending part where the force increases simultaneously with the length. Subsequently, the second region features an approximately constant force of maximum value (the plateau region) followed by a third region where the force decreases while the length of the sacromere is further increased (the descending region). The optimal range of sacromere length is detected in the plateau region. In this optimal range, the number of cross-bridges of actin and myosin are at a maximum. When muscles are stretched above the resting length, they still generate a passive force even if they are inactive (like a nonlinear spring). Overall, when a muscle is activated, the total force generated is the summation of active and passive forces.

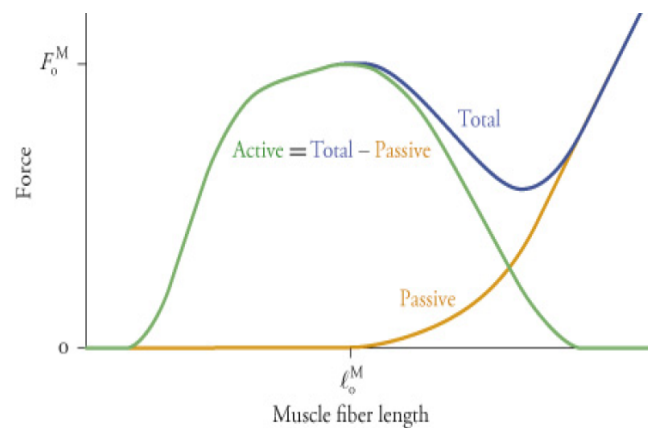


FIGURE 2.8: The active, passive and total force - length curves. The peak of active force F_0^M happens at the optimal fiber length l_0^M . Reproduced from (Thomas K. Uchida, 2021).

The force that a muscle can generate also depends on the velocity that its length changes. This relationship is presented in Figure 2.9. Active force increases as fiber is lengthening and decreases as the fiber is shortening. For high shortening velocities no active force is developed while for high lengthening velocities the muscles can be damaged. In the right part of the figure we also present muscle mechanical power, which takes a maximum value at about 1/3 of maximum shortening velocity.

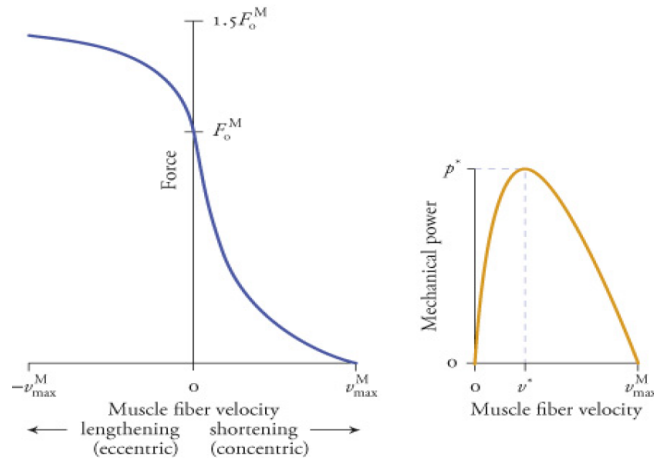


FIGURE 2.9: Muscle fiber force (left) and power (right) as functions of fiber velocity. Reproduced from (Thomas K. Uchida, 2021).

Study of muscle internal structure and functionality is hampered due to their complex nature. As we mentioned during the introduction, computational models can be developed to capture the features, properties and response of physiological systems. A widely adopted by research community muscle model, is the Hill - type muscle model. An overview of the model in the general case is presented in Figure 2.10. It is deployed in biomechanics studies to study muscle forces.

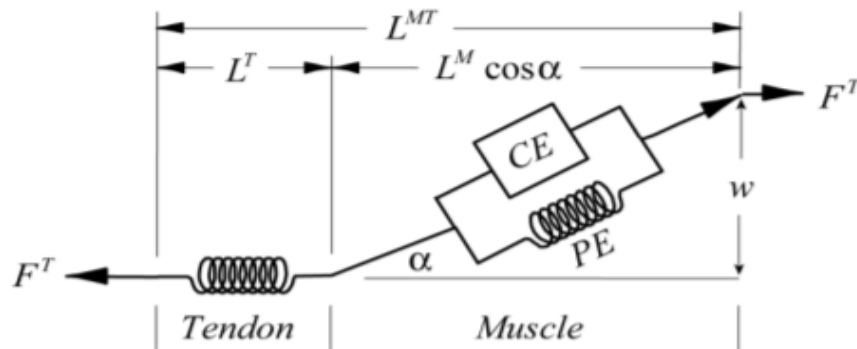


FIGURE 2.10: The Hill - type model of muscle - tendon complex. Reproduced from (Anderson and Pandy, 1999).

The main parameters of the Hill type muscle - tendon model are the following:

- CE = Contractile Element
- PE = Parallel Elastic Element
- L^{MT} = Length
- L^M = Muscle Fiber Length
- L^T = Tendon Length
- α = Pennation angle. Angle between the line of action of a muscle's fibers and the line of action of its tendon

The Hill - type model comprises of the following components: a tendon elastic element, an active contractile element and a passive elastic element. The last two components act in place of the active and passive force - generating properties of the muscle. The force that this muscle - tendon actuator can produce depends on the maximum isometric strength of the muscle and its corresponding pennation angle and fiber length, its maximum shortening velocity and tendons' resting length.

As mentioned previously, the muscles are excited by the central nervous system. In Figure 2.11 a computational model of activation dynamics is presented where excitation $u(t)$ is related to activation $a(t)$. This model relates the rate of change of muscle activation (i.e., the concentration of calcium ions within the muscle) to the muscle excitation (i.e., the firing of motor units). In the presented model, the activation can vary between 0 (no contraction) and 1 (full contraction). Furthermore, the excitation signal can vary continuously between 0 (no excitation) and 1 (full excitation).

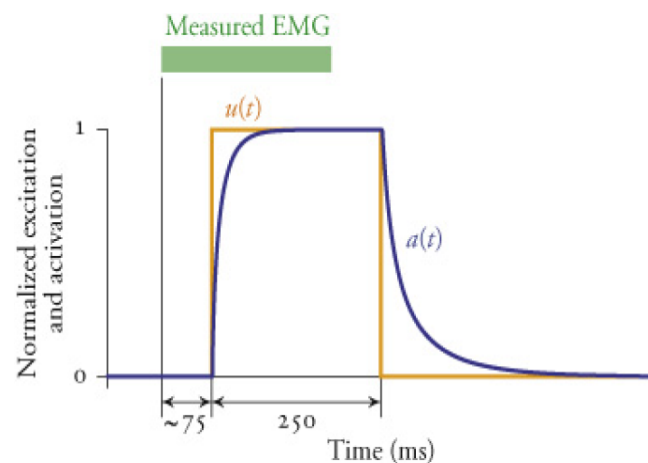


FIGURE 2.11: A computational model of activation dynamics that relates excitation ($u(t)$) to activation ($a(t)$). Reproduced from (Thomas K. Uchida, 2021)

Also, a muscle can neither relax nor generate force spontaneously. The production of force requires a complex chain of events. The delay between a motor unit action potential (the first step of these events) and the production of maximum force has been observed to vary from 5 to 50 milliseconds.

2.3 ACL biomechanics, injury and treatment

As already mentioned in subsection 2.1.2, ACL is one of the main ligaments that surround the knee joint. The ACL is placed at the midpoint of the knee. ACL functionality is fundamental as it prevents anterior sliding of the tibia relative to the femur, excessive tibial medial and lateral rotation and withstands varus and valgus stresses (Petersen and Zantop, 2007). It is composed of two bundles, the antero - medial and postero - lateral bundle and extends from the lateral femoral intercondylar notch towards the tibial plateau and the intercondyloid eminence (Duthon et al., 2006).

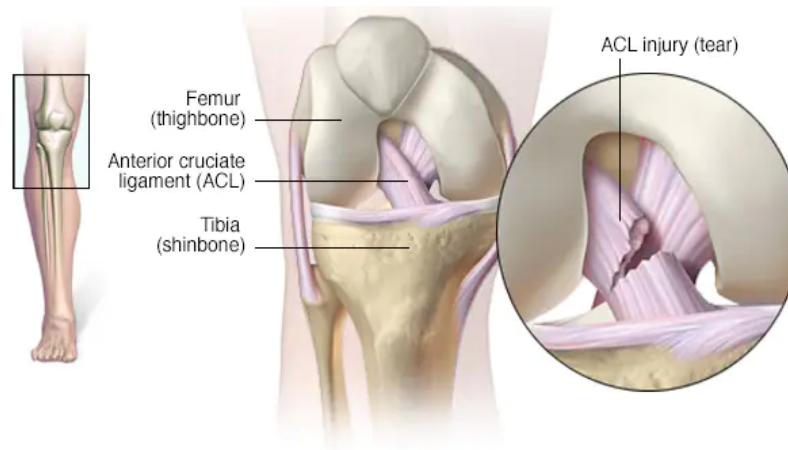


FIGURE 2.12: The anterior cruciate ligament (ACL) is one of the key ligaments that help stabilize the knee joint. The ACL connects the femur to the tibia. Reproduced from (MayoClinic 2021a)

ACL injuries are very common during dynamic movements when practising sport activities. These movements include sudden stops, abrupt changes of direction, landing after a jump and deceleration before changing direction (Sugimoto et al., 2014; Boden et al., 2000). Among the various types of injuries non - contact actions are the most significant cause of partially or completely ACL injury (Marieswaran et al., 2018). The risk factors for a non - contact ACL injury can be environmental, anatomical, hormonal and biomechanical – neuromuscular. From a biomechanical view, ACL can be injured from extreme anterior translation or by both valgus and internal rotation moments Figure 2.13 (Georgoulis et al., 2010). In the next section, significant factors that can contribute to an ACL injury when performing a landing after a jump motion are thoroughly presented.

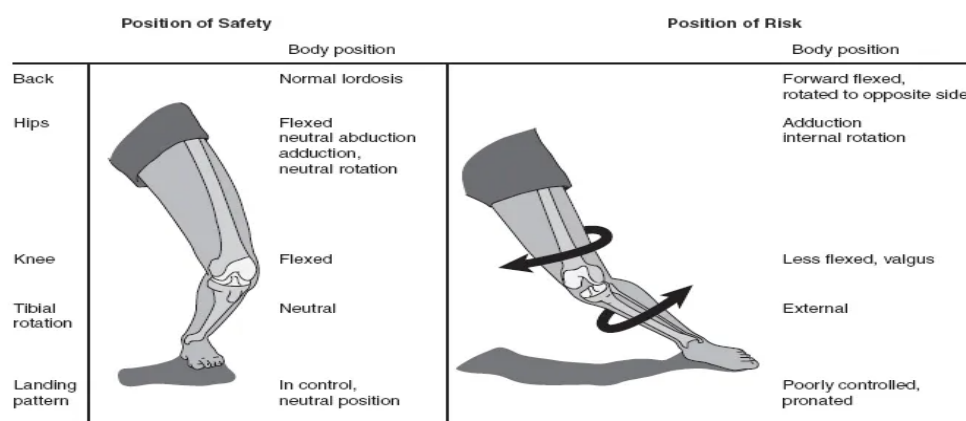


FIGURE 2.13: Mechanism of ACL rupture during change of direction. An increased injury is introduced with the foot planted, knee externally rotated or in valgus position and a varus or internal moment is applied. Reproduced from (Peter Brukner, 2016).

Usually, rupture of the ACL require the total replacement of the injured

tissue with grafts during a surgical procedure named as ACL reconstruction. Different techniques have been developed for the ACL reconstruction procedure, characterized by multiple parameters (like the graft material, the drilling location etc.). The regular workflow consists of drilling sockets or tunnels into the tibia and femur, collecting the graft from another anatomical structure (patellar tendon, hamstrings) and fixating it through the tunnels after replacing the damaged ligament.

2.3.1 Drop - Landing and potential ACL injury

Landing is one of the most common movements associated with ACL injury. In Figure 2.14 the motion of a double - leg landing is demonstrated. The landing phase is considered from foot strike to the time instant of maximum knee flexion angle. In Figure 2.14 the landing phase begins from the drop and ends at the end of collision stage.

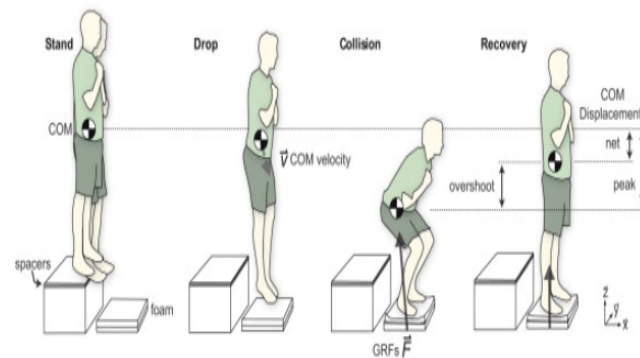


FIGURE 2.14: Representation of a drop - landing and displacement of the center of mass. The landing phase is considered from foot strike to the time instant of maximum knee flexion angle. The landing phase begins from the drop and ends at the end of collision stage. Reproduced from (Skinner, Zelik, and Kuo, 2015)

The correlation between ACL injury and the landing motion has been in the spotlight of multiple research studies. Initially, the height from which the landing is performed is a factor that affects potential ACL injury, as it is connected with the magnitude and direction of GRF (Hewett, 2017; Guy-Cherry et al., 2018a). Furthermore, an association between ACL injury and landing is related to the body posture at time of ground contact. Most of the athletes, when they attempt to land in a natural way after a jump, they tend to land stiffly. This term refers to the limited flexion of hip, knee and ankle angles. The result of a stiff landing is that all impact is absorbed between ankle, knee, and hip joints. On the contrary, a soft landing lowers the impact forces, extends the life of joints and finally the injury risk is decreased (Daniel Arnheim, 1997; Hewett, 2017; Guy-Cherry et al., 2018a). Additionally, flat - foot landings are considered of greater risk compared with natural and fore - foot landings (Teng, Leong, and Kong, 2020). Furthermore, different energy dissipation strategies have been found for single - leg and double - leg

landings. During single - leg landings the ACL injury risk is higher compared with double - leg landings (Yeow, Lee, and Goh, 2011).

Moreover, the alignment of the lower extremity has also been indicated by several researchers as a main risk factor. It has been reported by previous research studies that landings with lower knee flexion angle result on reduced absorption of the kinetic energy by the muscular system and on higher impact stress on other body tissues. Nevertheless, Griffin et al. pointed out that in the kinematic chain, not only the knee is included, but also the hip, ankle and trunk should be taken into account (Griffin et al., 2000). The most common lower - limb posture associated with ACL injury are foot pronation, tibial internal rotation, and a valgus position of the knee joint (Daniel Arnheim, 1997). Knee valgus posture can be caused by rotations of the hip and knee joints (Nguyen, Shultz, and Schmitz, 2015; Koga et al., 2017; Yasuda et al., 2016). Also, combinations of knee joint internal rotation, knee joint abduction, knee joint adduction moment and hip joint internal rotation can result in improper landings and ACL injury.

Additionally, multiple research studies have examined the effect of different upper body postures on ACL injuries (Blackburn and Padua, 2008; Saito et al., 2020; Song et al., 2021; Jones, Herrington, and Graham-Smith, 2015; Donelon et al., 2020). It has been observed that trunk flexion - extension, bending and rotation affect the kinematics of the joints of the lower body and the landing forces.

Several studies have shown great correlations between tibio - femoral forces, GRF and muscle forces during landings (Mokhtarzadeh et al., 2010; Mokhtarzadeh et al., 2012; Hernandez et al., 2013). Along with the fact that the ACL restrain anterior tibial translation, the quadriceps and hamstrings muscles are also considered as a highly important pair of agonist - antagonist muscles related to ACL injuries because of their crucial role in anterior tibial translation. Additionally, at the peak of GRF during landing, absence or delay of muscle activation can cause ACL injury, while greater quadriceps/hamstrings ratio indicates greater anterior knee muscle force and increases the risk or ACL injury (Mokhtarzadeh et al., 2012; Griffin et al., 2000).

Other identified ACL injury risk factors are the axial tibial torque, the valgus moment and hyper - extension moment. These factors can cause anterior tibial translation, valgus rotation or anterior tibial translation respectively and increase the risk of ACL excessive stretch (Hernandez et al., 2013). Also, the ACL strain can be increased by externally applied knee abduction moments, anterior tibial shear force and knee internal rotation moments (Shin, Chaudhari, and Andriacchi, 2007; Shin, Chaudhari, and Andriacchi, 2011; Bates et al., 2019; Bates et al., 2017).

2.4 Mathematics and physics concepts

In this section we give a general description of multibody dynamics. Then, we introduce the trajectory optimization problem and outline the optimization methods adopted by the software tools deployed throughout the study workflow presented in this thesis.

2.4.1 Multibody dynamics

Mechanics studies the behavior of physical bodies subjected to displacements and forces (Lindström, 2019). It is distinguished in two branches, dynamics and statics. Statics study the forces and their effect on a system when it is in static equilibrium. On the contrary, dynamics examine bodies when in motion.

Dynamics are subdivided into kinematics and kinetics (Mounts, 1970). First, kinematics investigate the relative motion of the components of the system. They do not consider the forces that generate the motion, but rather provide knowledge about properties such as displacement, velocity, acceleration and their variation over time. On the contrary, kinetics examine the relation between the motion of the system and the cause of that motion (forces and torques).

In biomechanics, human musculoskeletal system is usually modeled as a multibody dynamics system, adopting many parts of the robotics theory (Nordin and Frankel, 2013; SimTK - confluence 2011a). These systems are represented as a series of rigid bodies called links, starting from a base link that is usually called ground and is considered fixed in space. Every link is added to the kinematic chain through connections that are called joints. These joints impose the constraints of the system, meaning that they permit only certain relative displacements (translation or rotation) between the rigid bodies they connect. Furthermore, force elements such as springs, actuators and dampers, are included along with any applied external force. This system model can also be mathematically described as the system of equations that model the physical response of a given system. In our case this response is the model's motion that is subject to the forces applied and the modeling assumptions we have adopted. A general description of the equations of motion for a multibody system is presented in Equation 2.1.

$$\tau = M(\theta)\ddot{\theta} + H(\theta, \dot{\theta}) \quad (2.1)$$

τ = generalized forces and moments

M = symmetric positive definite mass matrix

θ = generalized coordinates

$\dot{\theta}$ = generalized velocities

$\ddot{\theta}$ = generalized accelerations

H = centripetal, Coriolis, gravity, friction, external forces

2.4.2 Trajectory Optimization problems

Trajectory optimization problems refer to a set of mathematical methods that aim to produce an optimized trajectory for a dynamic system. This trajectory minimizes a given cost functional and has to satisfy the constraints of the system. A general scheme of this problem is displayed by the next formulas:

Optimal trajectory:

$$(x^*(t), u^*(t))$$

System dynamics:

$$\dot{x} = f(t, x, u)$$

Constraints:

$$c_{min} < c(t, x, u) < c_{max}$$

Boundary Conditions:

$$b_{min} < b(t_0, x_0, t_f, x_f) < b_{max}$$

Cost Functional:

$$J = \varphi(t_0, x_0, t_f, x_f) + \int_{t_0}^{t_f} g(t, x, u) dt$$

where \mathbf{x} refers to a state variable, a differentiated variable in the dynamics equation, and \mathbf{u} refers to a control variable.

The above description is a continuous problem that needs to be transformed into a non-linear one in order to be solved. This procedure is executed by transcription methods. Then, the problem can be solved by solvers like the IPOPT (Wächter and Biegler, 2006). The new form of the problem is displayed by the next formula:

$$\begin{aligned} & \text{minimize} \quad \bar{J}(z), \quad z \in R^n \\ & \text{subject to :} \quad 1 \leq \begin{pmatrix} z \\ \bar{c}(z) \\ Az \end{pmatrix} \leq u \end{aligned}$$

The transcription methods are divided in two main categories: the shooting methods and the simultaneous methods. Simultaneous methods enforce the dynamics at a series of points along the trajectory, while shooting use a simulation to explicitly enforce the system dynamics.

Also, the methods for trajectory optimization can be direct or indirect. Direct methods convert the trajectory optimization problem into a discrete nonlinear problem. Both shooting methods and collocation methods, that will be presented next, are direct methods.

2.4.2.1 Shooting methods

Shooting methods are based on simulation and the discretization is executed using explicit integration schemes. Also these kind of methods performs better for problems with very simple controls and in absence of path constraints.

One of the simplest methods of transcribing an optimal control problem is the single - shooting method. If we examine the problem where a canon tries to hit a target, then we have two decision variables and one constraint. More specifically, the constraint is that the projectile has to hit the target and the decision variables are the mass of the powder and the firing angle. Also, the powder mass serves as the cost function. In general single - shooting methods make a guess for the decision variables and then assess the result. For our example, this method makes a guess about the mass of the powder

and the angle. Based on these, the cannon fires the projectile and the method investigates whether the target was hit. If not, a new guess is created based on the previous result. This simulation is repeated until the target is finally hit.

On the other hand, in multiple - shooting the trajectory is split in segments and in each segment single - shooting is applied. These segments are not necessarily matched up. If we choose to solve for more segments, then the relation between the objective function and the decision variables becomes more linear. Next, in Figure 2.15 we display a comparison between single - shooting and multiple - shooting. We can notice that in multiple - shooting a constraint is added in order to create a continuous trajectory.

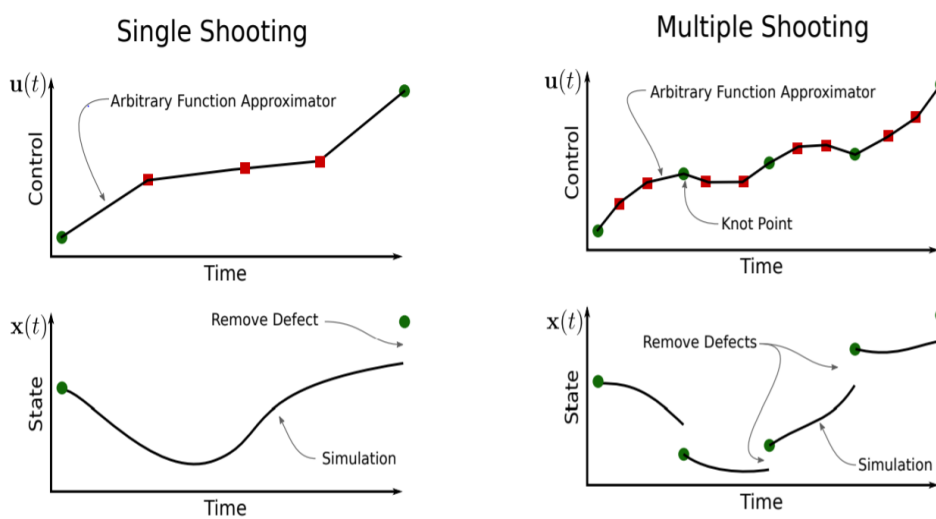


FIGURE 2.15: Single - Shooting and Multiple - Shooting methods. Reproduced from (Kelly, 2017b).

In trajectory optimization problems, the dynamics constraints can be written in two different forms. The first form is the derivative method where the derivative of the state with respect to time should be equal to the dynamics function. The second method is the integral method where the state trajectory must be equal to the integral of the dynamics with respect to time. The shooting methods use the integral method.

The formulas for the previously mentioned methods are presented next.

$$\text{Derivative method: } \dot{x} = f(x, u)$$

$$\text{Integral method: } x = \int f(x, u) dt$$

One of the main complications when using trajectory optimization methods is that they can become stuck in a local minimum in the space of trajectories. As a result, their response depends on an initial guess. It is extremely hard for these methods to detect a trajectory that is not homotopic to the initial trajectory and they cannot recover from an initial guess in a wrong homotopy

class. For that reason, providing an appropriate initial guess to the solver can put it close to the "right" local minimum of the trajectory.

2.4.2.2 Collocation methods

Collocation methods are based on function approximation. These methods use an implicit integrator to approximate system dynamics. Furthermore, they perform more efficiently in problems with complicated control and / or path constraints.

In direct collocation method the controls and states of the system are approximated as splines over the mesh of time points. The continuous trajectory optimization problem is discretized by approximating the continuous functions of the problem as polynomial splines. Subsequently, the optimizer solves for the knot points that lead the splines to comply with the dynamics of the system. The dynamics are enforced by demanding that at specified time points, the time derivative of the state splines match the derivative from the system differential equations. That way, a non linear program is created, where the states are the variables and the constraints that are enforced are the system dynamics. An important attribute of this method is that large problems can be tractable because the constraints at a given time point depend only on the variables near that specific time.

An example of how direct collocation solves simple problems is presented next, adopted from (Kelly, 2017a). Lets consider a model of a small block that consists of a point mass, that can translate only in one direction. If we try to simulate its movement between two points with initial and final states at rest in a defined amount of time, then the dynamics describe the way that the system moves. The input of the system (or the control) is the force applied on the point mass.

$$\text{System dynamics: } \dot{x} = v, \quad \dot{v} = u$$

where x refers to position, v to velocity and u to control.

Both initial and final position and velocity should be zero. The requirements concerning initial and final state along with the desire to move the point mass one unit of distance in one unit of time are presented next and schematically in Figure 2.16.

$$\text{Boundary conditions: } x(0) = 0, \quad x(1) = 1, \quad v(0) = 0, \quad v(1) = 0 \quad (2.2)$$

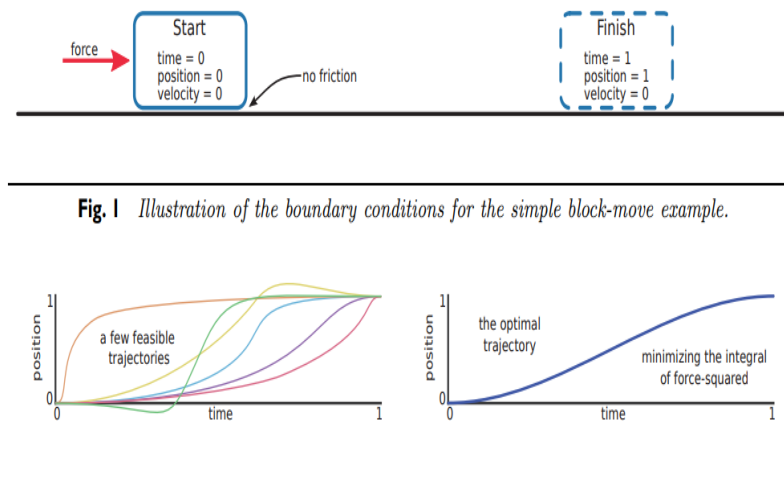


Fig. 1 Illustration of the boundary conditions for the simple block-move example.

FIGURE 2.16: Feasible (left) and optimal (right) trajectories for a simple movement of a block using direct collocation method. Reproduced from (Kelly, 2017a).

As seen in Figure 2.16 (left), there are many feasible solutions to this problem. Trajectory optimization aims to find the best feasible trajectory or the optimal solution. The objective function describes the "best" solution based on an objective. Therefore, optimal trajectory is a feasible one that also minimizes the objective function. One example of an objective function can be the minimum of force squared which is provided by the next formula:

$$\text{Minimum force squared: } \min_{u(t), x(t), v(t)} \int_0^1 u^2(\tau) d\tau \quad (2.3)$$

The solution of this problem is given by:

$$u^*(t) = 6 - 12t, \quad x^*(t) = 3t^2 - 2t^3 \quad (2.4)$$

Subsequently, we describe some basic concepts of "trapezoidal" and "Hermite - Simpson" collocation methods. The "trapezoidal" collocation method offers a finite set of decision variables. This is accomplished by expressing the position and velocity (which are continuous on time) by their values at exact time points. These time points are the collocation points. Also, the system dynamics needs to be converted into a set of constraints that can be applied for every collocation point at states and controls.

The "trapezoidal" rule is used in order to make the conversion of the system dynamics. The main idea is that the change in state between two points is equal to the integral of the system dynamics. Then, the integral is evaluated and the dynamics between all pairs of knot points is approximated. Also, the constraints and the boundary conditions are enforced on all segments and collocation points respectively. Finally, the objective function is estimated as a summation of each segment at the knot points using the control error.

For the previous block example, we get a quadratic program (easier to solve compared to a nonlinear one), given that the constraints are linear and

the objective quadratic. A spline that interpolates the solution trajectory must be created given the set of positions, velocities and controls at the collocation points. In trapezoidal collocation, a linear spline is used for the control, while for the states a quadratic one is used.

The "Hermite - Simpson" collocation method is analogous to the trapezoidal but it offers a higher-order accurate solution. This is due to approximating the system dynamics and the objective function as quadratic functions and not linear. Also, the state trajectory is a cubic Hermite spline. To approximate the integrand, Simpson quadrature uses a quadratic segment. That segment fits three points uniformly aligned in space.

2.5 Literature Review

In this section, a review of research studies that follow an experimental and/or simulation approach regarding the identification of ACL injury risk factors during single - leg landings and subsequent cutting movements is conducted. Based on this review we will be able to present the methods of this study, the scientific improvements and limitations along with the contribution of this work. The order of presentation is based on each investigated parameter. Initially, a description of research studies that consider the correlation of initial landing height and ACL injury risk is conducted. Subsequently, we reference studies that explore lower limb static alignment and produced loads on the knee joint, following by studies that examine the relationship between trunk orientation and ACL injury.

2.5.1 Landing height

Starting with the initial landing height, Mokhtarzadeh et al. conducted a study where single - leg and double - leg landings from different initial heights were performed by ten volunteers in a motion analysis lab. The researchers collected joint kinematics and GRF using six cameras and two force plates respectively. The acquired data were used in an inverse kinematics and dynamics analysis that utilized subject specific models through the OpenSim software. The authors reported the importance of the hamstring muscle due to its ability to posteriorly move the tibia bone and, therefore reducing the load on the ACL. Also, they stated that when the Q/H force ratio was greater than 1, the quadriceps caused the tibia to translate anteriorly which can increase the risk of ACL rupture. On the the other hand, when the ratio was less than 1, the increased hamstrings muscle group contribution caused a posterior tibia movement protecting the excessive and abrupt ACL extension. Furthermore, greater values for vGRF were observed for landings initiated from greater heights. Regarding quadriceps and hamstrings muscle groups, greater forces were observed for landings from 60cm height at time of max vGRF (Mokhtarzadeh et al., 2010). In a latter study, the contribution of ankle plantarflexors (gastrocnemius and soleus muscles) to the ACL load during single - leg landing was examined (Mokhtarzadeh et al., 2013). The parameter of interest was the set of knee joint reaction forces to predict the forces exerted

on the ACL. The authors collected kinetic, kinematic, GRF and EMG data. Then, muscle forces were estimated using a processing procedure (Inverse Kinematics (IK), Residual Reduction Algorithm (RRA), Static Optimization (SO)) using again the OpenSim software platform. They observed that at peak GRF, quadriceps and soleus forces were greater as the initial height increased and that these two muscles acted as ACL agonist - antagonist. Finally, the forces of the muscles that act at the knee joint reached their maximum value after the GRF and ACL forces' peak.

In a similar study, Verniba et al. examined how drop height (22 and 44cm) and style of landing (natural, soft or stiff) affect knee compression force and external flexion moment. Towards this objective, they measured knee flexion angles and vGRF during landings performed by 20 male participants. They observed that peak knee flexion angle was greater for soft landings and for higher heights. Also, they detected that vGRF and knee joint compression were greater as height increased. The same was also true during stiff landings (Verniba et al., 2017). Landing from different heights (32cm, 52cm and 72cm) was again the objective of an additional study (Niu et al., 2018). The authors observed that when the height was increased the vertical forces of all ankle, knee and hip joints were also incremented. Similarly, the forces of several muscles like rectus femoris, gluteus medius, vastii, biceps femoris and adductor magnus were also increased. The researchers also noticed that the iliopsoas, rectus femoris, gluteus minimus and soleus muscles were activated at an earlier time as the dropping height was increased, in contrast with the activation of tibialis anterior that exhibited a delayed activation. Finally, Heinrich et al. examined landings from different heights and compared the effect of landing height along with the effect of trunk leaning on ACL injuries. The simulation included a musculoskeletal model of a skier and tracking experimental data of a jump landing. The results of the study showed that as the jump height and the backward lean were increased, the peak ACL force was also increased. The authors concluded that peak ACL force was sensitive to both variations of trunk leaning and landing height (Heinrich, Bogert, and Nachbauer, 2018).

2.5.2 Lower extremity alignment

As it was previously mentioned, another risk factor of interest that has been associated with ACL injury is the static lower extremity alignment. This condition refers to the rotational alignment of the knee and hip joint during landings and that poses the knee in a valgus posture which is an ACL damage risk factor. Nguyen et al. evaluated combinations of hip and knee joint kinematics, kinetics and external moments during the landing phase of double - leg landings (Nguyen, Shultz, and Schmitz, 2015). The participants were separated in three groups: those with internally rotated hip and knee valgus posture, those with externally rotated knee and valgus knee posture and finally those with neutral posture. The authors observed that groups with internal rotated hip experienced also greater knee valgus motion and smaller hip flexion moments compared to participants with neutral alignment. Also,

participants with internal rotated hip had increased hip rotation moment that tend to place the knee joint in a valgus configuration.

Moreover, the association of ACL injury risk with stiff landings was the main interest of a study that included 171 female basketball and football players. The researchers observed that lower knee flexion and higher peak vGRF during stiff landings are correlated with high risk of ACL injury (Leppänen et al., 2016). In a study conducted in 2018, Guy - Cherry et al. tested three different landing styles (stiff, self - selected and soft landings) in order to indicate which one leads to the most safe landing conditions. They used MoCap equipment with ten cameras to record the kinematics of the lower extremity and an EMG system to record muscle activity. It was observed that peak GRF were different for each style, with lower values for soft landings and higher for stiff landings (Guy-Cherry et al., 2018b).

Koga et al. (Koga et al., 2017), attempted to describe the foot position along with hip and ankle kinematics based on ten videos of ACL injuries experienced by women athletes during basketball and baseball games. They observed that the hip was internally rotated during the interval between initial contact and the next forty milliseconds. The hip internal rotations during all injury cases ranged between 18° and 39°. The authors used a model - based image matching technique to reconstruct the 3 - Dimensional (3D) kinematics to estimate these ranges. It should be mentioned that in six out of ten cases a contact (no direct with the knee) with another player took place at the time of injury and three of the injuries occurred during single - leg landing, while the rest of the injuries took place during cutting movements.

In another study, Yasuda et al. investigated landings of handball players and observed that the ACL injured players demonstrated greater hip internal rotation than the uninjured players (Yasuda et al., 2016). Internal rotation dominance of the hip joint was observed in seven out of eight injured players. Their logistic regression analysis revealed that internal and external rotation and extension of the hip joint is correlated with injury of the ACL. These observations concerns the female participants, while for the male participants the results were not that obvious. Also, studies conducted about cutting or changing of direction motions identified hip internal rotation as a risk factor. Internal hip rotation translates the knee more medial to the GRF vector, thus increasing the moment arm of the force and introducing a greater moment at the knee joint. This further results to an increase of the GRF and higher risk of injury (Sigward, Cesar, and Havens, 2015).

Peel et al. investigated lower extremity kinetics and kinematics when double - leg landing from 40cm with 15° and 30° of toe - in and toe - out conditions or self - selected (Peel et al., 2020). Their observations indicate that the toe - in landing position is connected with increased hip internal rotation, knee abduction, ankle inversion angles at Initial Ground Contact (IGC) and peak knee Internal rotation moment (IRM), knee Abduction moment (AbdM) and hip AbdM. This implies that toe - in landing position is of high risk concerning ACL tear. Landing with toe - out position was related to higher hip flexion and abduction, knee flexion and external rotation angles at IGC and peak hip Extension moment (EM) and AbdM, knee Adduction moment

(AddM), ankle plantar - flexion and inversion moments. Also, the ankle inversion angle was reduced. These findings suggest that the toe - out landing position could reduce the risk of ACL injury. All these angles and moments were higher for the cases of 30° compared with 15°. Concerning the self - selected landings, it was observed that participants landed with a 18° toe - out position. The authors concluded that toe - in position compared to self - selected was associated with increased risk.

2.5.3 Trunk orientation

In two studies conducted by Blackburn et al., the effect of trunk flexion - extension on the kinematics of the hip and knee joints and on the landing forces during drop landing tasks was examined (Blackburn and Padua, 2008; Blackburn and Padua, 2009). They used a MoCap system to record kinematic, kinetic and EMG data of a participant group. All participants were asked to perform two different landings. First, they attempted a natural landing (of their own preference) and subsequently to land with the upper body in a flexed position. These data were used in both of these studies. The authors observed that during the flexed landing the trunk was more flexed at both IGC and loading phase. Also, the knee and hip joints were more flexed. Moreover, they derived that the peak of posterior Ground Reaction Force (pGRF), vGRF and the mean amplitude of the quadriceps EMG were all lower during the flexed landing.

In a similar study conducted by Shimokochi et al., three different landing styles were evaluated (Shimokochi et al., 2012). These included a self - selected, one leaning forward and finally an upright position single - leg landing. The 3D biomechanics, muscle activities of the lower body and landing forces of these cases were recorded using motion analysis (3D electromagnetic tracking system), EMG and GRF. Regarding the upright landings, the authors observed greater peak vGRF but lower values of medial and lateral gastrocnemius and lateral quadriceps activation. Also, lower values of plantar - flexion and hip extensor moments were observed, while the peak knee extensor moments were greater for the upright landings. Based on these observations they concluded that landing with an upright position can harm the ACL, while leaning forward can protect it.

In a review research conducted by Song et al., the trunk motion was associated with ACL loading variables by observing videos with ACL occurrences. First, the authors stated that limited trunk flexion was associated with increased ACL risk of injury. Then, increased lateral bending on both sides but mostly towards the injured leg and increased axial rotation towards the landing side were also associated with increased knee external abduction moment arm, which can potentially lead to a ACL injury. A similar study focused on trunk position during a single - leg landing (Saito et al., 2020). The following trunk orientations were assessed: neutral or preferred, in flexion, in extension and in right and left lateral flexion. Using a two - dimensional video analysis and EMG recording devices, the researchers recorded knee flexion, knee valgus angle values and activity of the rectus femoris and biceps femoris

muscles. They stated that the knee valgus angle had greater value during the left lateral flexion trunk position (when leaning toward the opposite site of the landing side) compared to trunk right lateral flexion position. Both of these had greater values compared to the extension position. As conclusion, a trunk flexion can be less risky for ACL injury due to the higher knee flexion angle, lower knee valgus angle, lower muscle activity of the rectus femoris and higher muscle activity of the biceps femoris (hamstrings). Finally, regarding trunk bending, higher values of GRF were observed when a control - lateral lean of trunk in the opposite direction of travel was involved during 90° cutting motions (Jones, Herrington, and Graham-Smith, 2015).

2.5.4 Knee joint surrounding muscles

One additional factor of ACL injury during landing movement is the role of the knee surrounding muscles. Morgan et al. conducted a dynamic simulation study with MoCap data in order to reveal the importance of the muscles spanning the knee joint in injuries during the weight acceptance phase of single - leg jump landings (Morgan, Donnelly, and Reinbolt, 2014). A model of 5 DoFs on the knee joint and an ACL, was used in OpenSim software. The authors observed greater maximum muscle forces for quadriceps, gastrocnemius and then hamstrings (in decreasing order). Two groups were created, high - risk and low - risk based on the mean values of the shear ACL forces and joint compressive forces. It was observed that for the high - risk group (with greater mean ACL strain and force), the quadriceps and hamstrings yielded greater forces.

Mazumder et al. attempted to simulate the mechanism of ACL injuries using OpenSim software (Mazumder et al., 2019). Their objective was to derive optimal solutions concerning muscles activation while landing in order to avoid injury. Data from 5 landing trials were collected. They used a musculoskeletal model that featured a knee joint with three DoFs and ligament modeling for their analysis. The authors pointed out that common causes of injury are increased abduction of the hip and knee joints and greater knee abduction loads, which are often caused by muscle fragility. They also evaluated and adjusted co - activation of quadriceps and gastrocnemius muscle groups through a controller. The optimal result (decreased ACL injury risk) for quadriceps / hamstrings activation ratio was equal to 0.3 whereas for gastrocnemius / tibialis anterior the activation ratio was equal to 0.2.

Heinrich et al. investigated landings of skiers and they observed that quadriceps force was also sensitive to trunk lean before IGC. Hamstrings force decreased with increased backward lean but the change was not significant (Heinrich, Bogert, and Nachbauer, 2018).

Shin et al. (Shin, Chaudhari, and Andriacchi, 2007) developed a 3D subject - specific knee dynamic simulation model in order to test the impact of deceleration forces on the ACL strain during single - limb landing when running. The knee model was created based on MRI of a cadaver specimen. They demonstrated that the posterior deceleration force can protect the ACL by reducing the peak strain that the contraction of quadriceps muscles produce.

Their findings indicated that a quadriceps force is a non likely mechanism for injury and other mechanisms like valgus rotation, or internal rotational can be more relevant. Internal knee extension moments, internal knee rotation moments and knee flexion moments can also be responsible for higher loads at the knee joint (McBurnie, Dos'Santos, and Jones, 2019).

Methods

In this chapter we describe the methods used in this thesis. First, we present the software platforms and tools utilized to perform the simulations. These are the OpenSim software, the SCONE software and the MOCO tool. Also, a description of the musculoskeletal models is introduced along with the applied modifications. Then, we demonstrate the simulation setup for predicting a single - leg landing motion using the SCONE software. Finally, we describe the simulations conducted in MOCO in order to predict the motion of a single - leg landing using more complex models and the formulation of multiple what - if scenarios to evaluate ACL injury risk factors found in literature. All the steps of the simulation pipeline along with the examined scenarios and the exported results are presented in Figure 3.1.

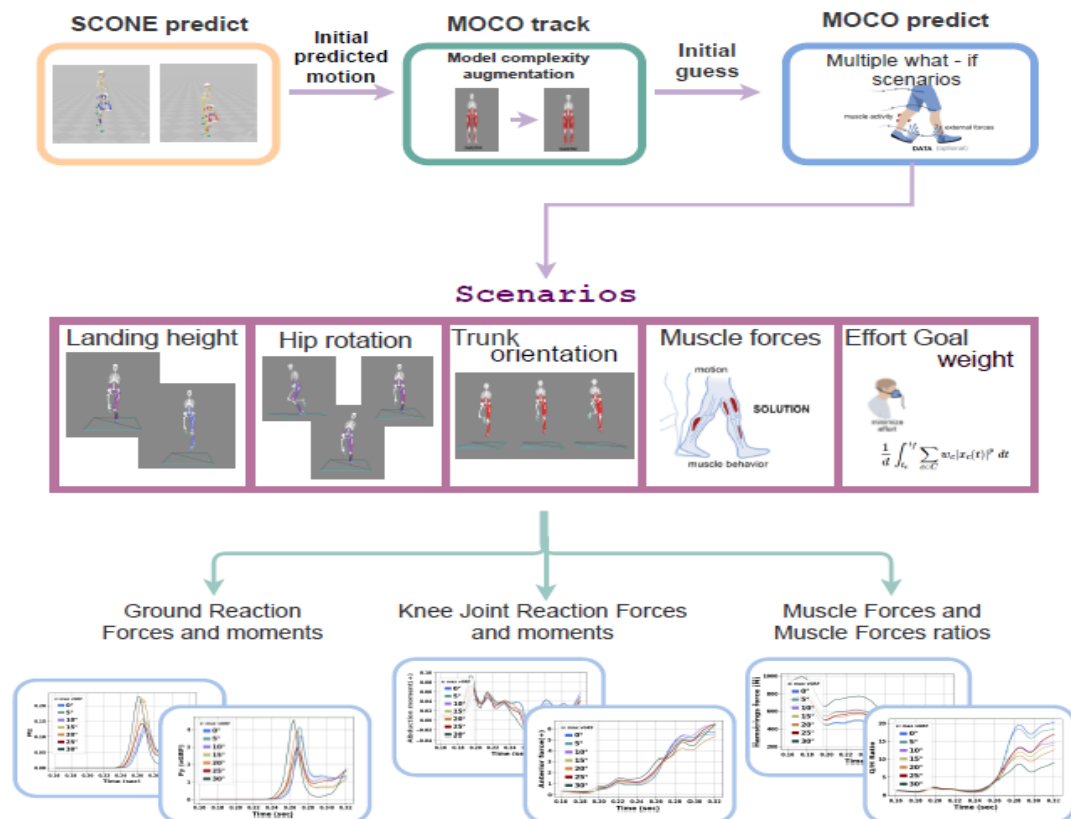


FIGURE 3.1: Overview of the proposed simulation pipeline of this thesis. In the first layer, the implemented methods and software tools used in this thesis are presented. Next, in the second layer all the examined scenarios are introduced and finally in the third layer, the exported results are presented.

3.1 Dependencies

Predictive simulation tools offer the opportunity to generate motion trajectories of a variety of tasks (gait, squat - to - stand, jump, landing) subject to high - level objectives without the need of experimental clinical data. Examples of objectives are solution stability, gait speed, energy efficiency, minimization of certain joint loads, pain avoidance or combination between them. That way, researchers can compose "what - if" scenarios and optimize them. In this section we present the software and tools used in this thesis and allow for simulations of biological motions. These are the OpenSim and SCONE software packages and the MOCO tool that is part of the OpenSim software.

3.1.1 The OpenSim software

OpenSim ([OpenSim Software 2005-2012](#)) is a freely available software package that allows researchers to build and analyze musculoskeletal models and dynamic simulations of movements. Furthermore, it provides a user - friendly graphical user interface (GUI) allowing to use multiple tools of musculoskeletal analysis. OpenSim gives the opportunity to study a given motion in a high level, analyzing the joint angles, the joint torques and the external, muscle or joint reaction forces that are involved. In general, it requires data that are generated by human motion experimentally and are collected with a MoCap system. The availability of predictive simulation tools is an alternative source of motion data that can be used as an input into the standard OpenSim pipeline.

The key block of the OpenSim workflow is the OpenSim model. OpenSim models consist of multiple rigid bodies that are connected through joints. The joints define a parent - child kinematic relationship between the reference frames that are fixed to each body. A joint is described by its spatial transform. For a 6 Degree of Freedom (DoF) joint, three rotations and three translations comprise a joints' spatial transform. The transform describes the spatial position of body B in parent body P as a function of the joint coordinates as presented in [Figure 3.2](#). The model's posture at each time instant is described by the coordinates of all the model joints, also mentioned as the generalized coordinates. Additionally, point, weld or coordinate coupling constraints can be used to enforce constraints to the model. Point constraints restrain relative translations between two bodies. The weld constraint fixes the relative location and orientation of the bodies. Finally, coupling constraints links joint coordinates to any other model coordinate. Moreover, forces are used to actuate the motion of the model. These forces can be produced by either passive elements like springs, dampers and contacts or by active generators like torque actuators and muscles. As we see the OpenSim models encapsulate all key features of multi - body systems dynamics described in [subsection 2.4.1](#)

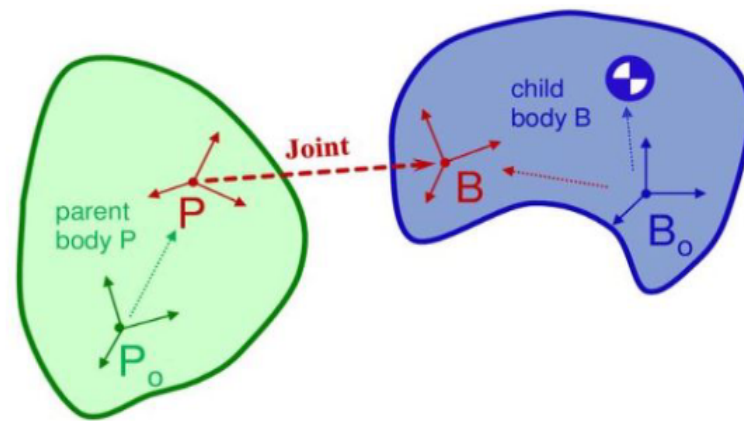


FIGURE 3.2: A joint connects two rigid body reference frames and is used to define the kinematic relationship between the rigid bodies. Reproduced from (SimTK - confluence 2011a).

Subsequently, the basic tools of OpenSim are concisely described, which are Scaling, IK, SO, Analyze tool and Joint Reaction Analysis (JRA). In this study, the Analyze tool and JRA tool were mainly used to extract the results of the prediction simulations.

Firstly, the Scale tool allows to modify a generic musculoskeletal model, so it can accurately reflect a real subject based on its anthropometric properties. Usually, this is achieved by measuring the distance between experimental marker data placed on the subject during a static trial and virtual marker data placed on the model. Specific scaling weights are applied based on the confidence we have on our experimental data. At the end of the scaling process, each model segment is scaled accordingly. Moreover, the mass parameters (mass, inertia tensor) and the other components attached to the body segments (such as muscle actuators) are also scaled.

Next, the IK tool attempts to find the posture of the model that closely resembles the acquired motion at each time frame. This is performed by identifying the pose for which the weighted squared errors between experimental data and the coordinates estimated by the IK tool are minimized at each time frame.

Furthermore, the SO tool, uses as input the movement extracted by the IK tool and gives as output the unknown generalized forces based on the equations of motion. Therefore, it analyzes the joint moments into the forces that produce the motion at every time frame.

Moreover, the Analyze tool enables to analyze a model or simulation based on multiple inputs. These inputs may be model states, controls, and external loads applied to the model.

Finally, the JRA tool calculates the forces and moments at joints based on the loads acting on the model. These forces and moments account for the internal loads of the joint and are transferred between consecutive bodies. They should not be interpreted as the generalized forces estimated by the SO tool that act along or about the joint axes. The JRA loads act on the center of the joint and can be expressed on parent, child or ground frame. These

loads represent the summation of all contributions for each joint structure (including the non - modeled structures like ligaments and cartilage contact) that would produce the desired joint kinematics.

3.1.1.1 OpenSim models

In this section, we present the OpenSim models that were deployed in our simulations. We utilized three different models. The first one, was a simple model in terms of total muscles and DoFs and it was used to predict the motion in SCONE. Then, for the simulations in MOCO we used two musculoskeletal models of augmented complexity.

The musculoskeletal model adopted for the simulations conducted in SCONE was "Human0916". It is a 2D planar reduced gait model with 9 DoFs and 16 muscles created by Ajay Seth, closely based on an older model by Delp (Delp et al., 1990). The model resembles a subject of 1.8m height and 75.16kg weight. The movement of the model is constrained in the sagittal plane. Also, it consists of a planar joint with 3 DoFs between the pelvis and the ground and 6 more DoFs, 3 at each lower limb, one at the ankle, one at the knee and one at the hip. Furthermore, the model contains two spheres at each foot to establish a contact model in order to estimate the GRF when the feet touch the ground. These contact spheres have a radius of 4cm and are attached at the anatomical reference of the right and left calcaneus and toes. Moreover, the model contains eight muscle - tendon units of Hill - type at each leg: biarticular hamstrings (HAMS), gluteus maximus (GMAX), iliopsoas (ILPSO), rectus femoris (RF), vasti (VAS), gastrocnemius (GAS), soleus (SOL), and tibialis anterior (TA). The musculoskeletal model along with the contact spheres is presented in Figure 3.3. The simplicity of this model offered us the ability to perform quick simulations to obtain initial guesses for the subsequent MOCO predictions.

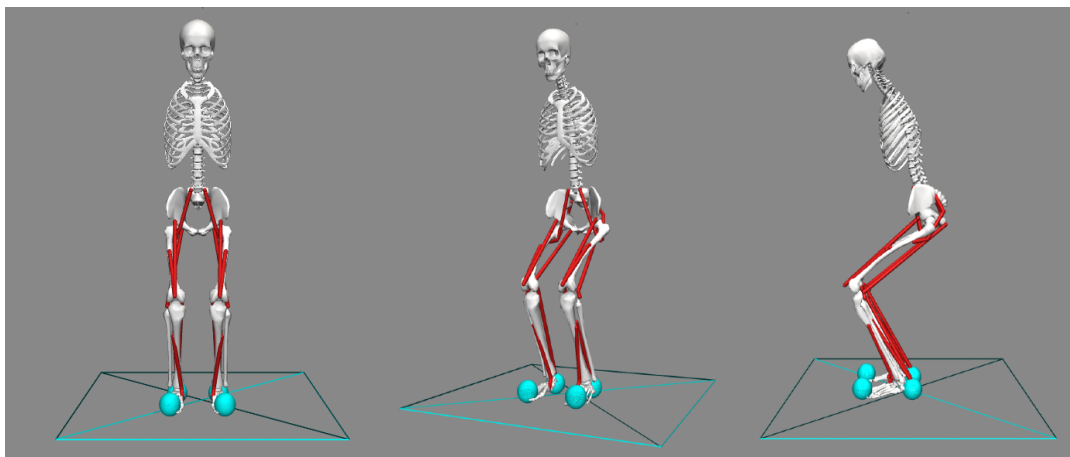


FIGURE 3.3: The musculoskeletal model developed by Ajay Seth used for the predictive simulation of single - leg landing in SCONE. It has 9 DoFs and contact spheres to estimate GRF.

The musculoskeletal models used for the simulations conducted in Moco were "Gait2354" and "Gait2392". These are 3D models of the human body with

23 DoF created by Darryl Thelen (University of Wisconsin - Madison), Ajay Seth, Frank C. Anderson, and Scott L. Delp (Stanford University).

The "Gait2392" musculoskeletal model consists of 92 musculotendon actuators in place of 76 muscles of the two lower limbs and torso. In "Gait2354" model the number of muscles is reduced in order to increase speed of simulations and simplify it for educational purposes. Also, Anderson took out the patella from "Gait2354" to avoid kinematic constraints. Both models represent a subject with 75.16kg mass and 1.8m of height. The models described previously are presented in Figure 3.4. Both models feature lower limb joint definitions from (Delp et al., 1990), low back joint and anthropometry adopted from Anderson and Pandy (1999), and a planar knee model adopted from Yamaguchi and Zajac (1989). There are 7 body segments for each leg: toes, foot, talus, tibia, patella, femur and pelvis. Each segment has each own reference frame as shown in Figure 3.5.

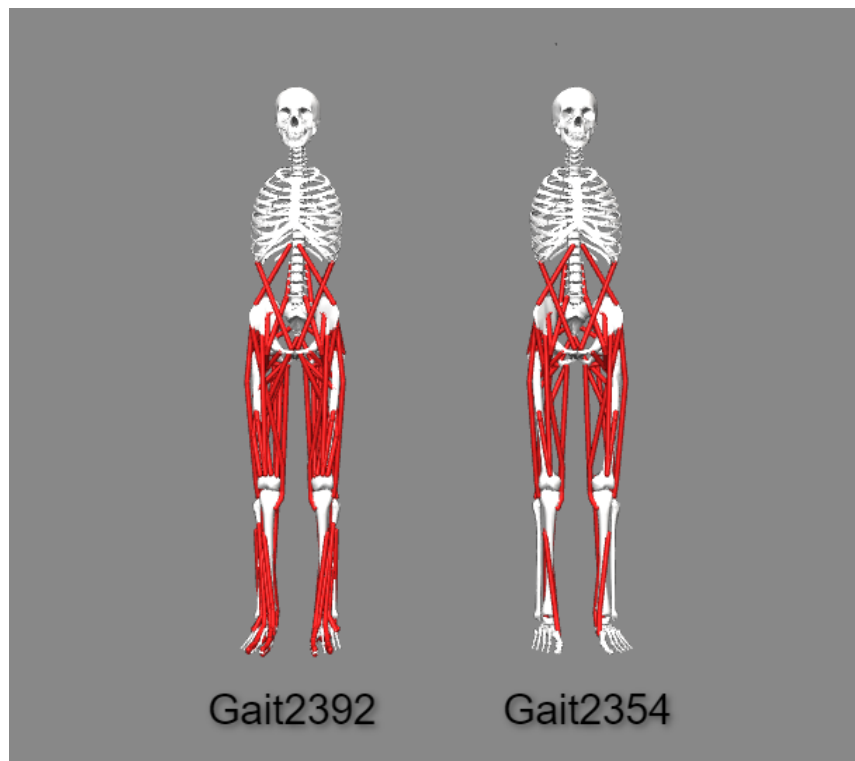


FIGURE 3.4: "Gait2392" and "Gait2354" OpenSim musculoskeletal models used for the simulations conducted in Moco. Both models were developed by Darryl Thelen, Ajay Seth, Frank C. Anderson, and Scott L. Delp, used for the predictive simulation of single-leg landing in Moco.

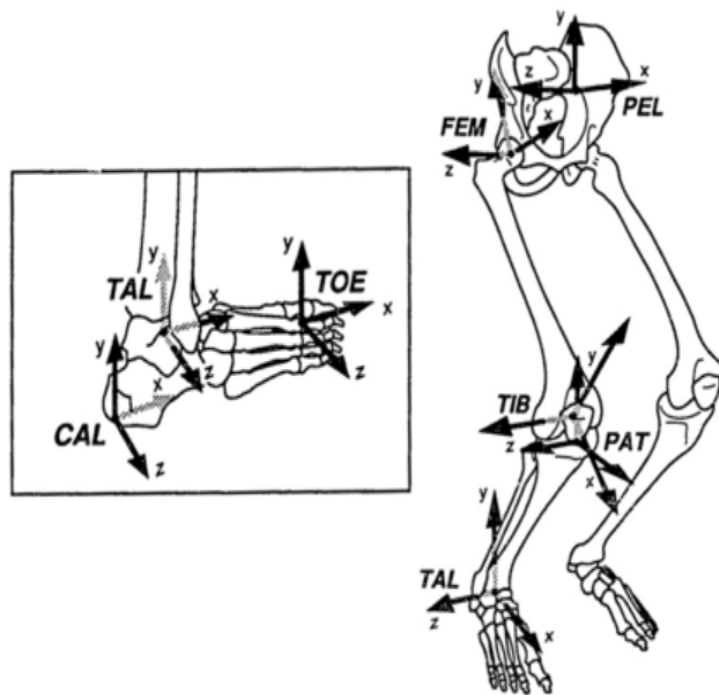


FIGURE 3.5: Location of the body - segmental reference frames. Reproduced from (Delp et al., 1990)

The reference frame of the pelvis is located at the middle of the line connecting the two anterior superior iliac spines. In the neutral position, the reference frame of the pelvis and the ground frame are aligned, meaning that model's pelvic tilt is zero, with respect to the ground. Next, the femoral frame is located at the center of the femoral head, while the reference frame of the tibia is fixed at the center of the line between the medial and lateral femoral epicondyles. Also, the reference frame of the toe is fixed at the base of the second metatarsal. Moreover, the calcaneal frame is fixed at the most interior lateral point on the posterior surface of the calcaneus. Finally the patellar frame is fixed at the most distal point of the patella, while the reference frame of talus is located at the center of the line between the apices of the medial and lateral malleoli.

The hip joint is modeled as a ball - and - socket joint, where transformations between the femoral reference frame and the pelvic reference frame allow rotations of the femoral frame about the 3 axes located in the femoral head. Next, the ankle, subtalar, and metatarsophalangeal joints are modeled as frictionless revolute joints. Regarding the knee joint as already mentioned it consists of 3 bones and it features a very complicated motion. For that reason Yamaguchi et al. provided a 1DoF model of the knee to represent the kinematics of not only the tibiofemoral joint, but also the patellofemoral joint. The tibiofemoral contact point depends on the knee angle and is specified according to data reported by Nisell et al. (1986). The geometry of the knee as described previously is presented in Figure 3.6.

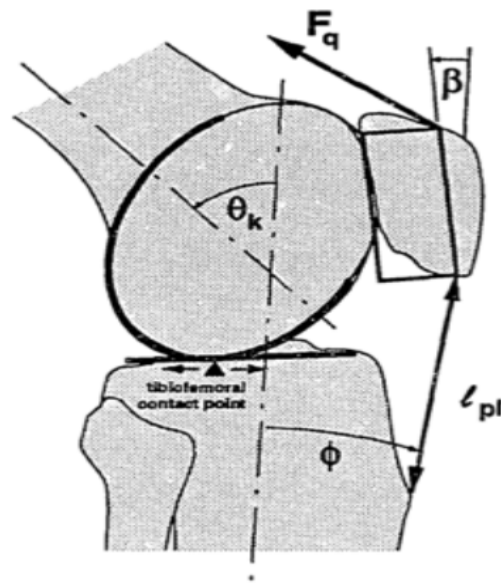


FIGURE 3.6: Geometry of the knee. Reproduced from (Delp et al., 1990).

Concerning the muscle - tendon units, each muscle - tendon path is described by line segments. Muscles can wrap over bones or can be constrained by retinacula. In OpenSim, intermediate via points can be used to describe the muscle path more accurately and model their real - life behavior (SimTK - confluence 2011a).

Foot - ground interaction for the "Gait2392" was modeled using compliant contact force model similar to "HuntCrossleyForce" by Hunt - Crossley (Serrancolí et al., 2019), except that this model applies force even when not in contact. Five spheres were placed under the foot of the model to stimulate the interaction of the foot and the ground adopted by (SimTK - confluence, Sky High 2011b). One sphere was placed under the toes and four under the hind - foot (Figure 3.7). For static and dynamic friction coefficients a value of 0.9 was selected. Also, in order to speed up and simplify the simulations, all muscles of the right lower limb were deleted from the model, since we are interested only in studying left - leg landing.

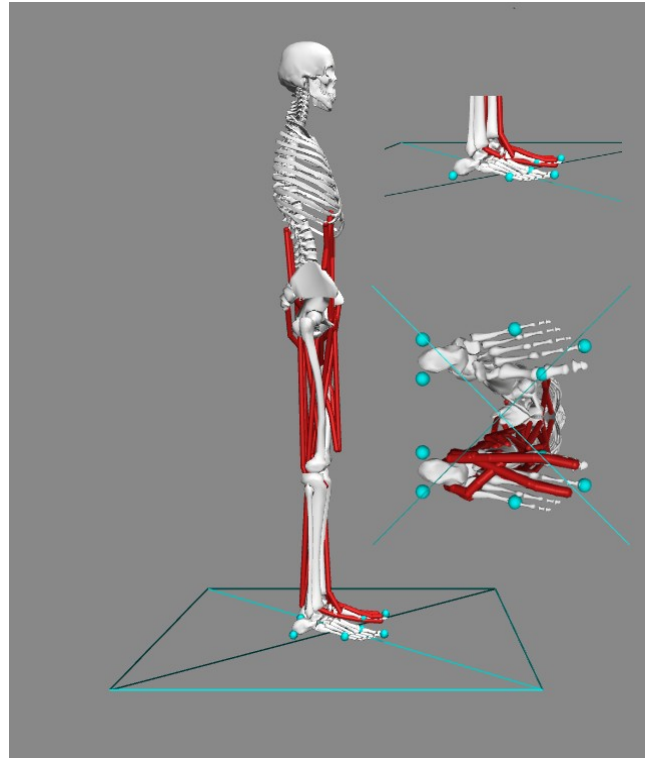


FIGURE 3.7: Schematic diagram of the musculoskeletal model with only the left side muscles. Foot - ground contact was modeled with five contact spheres per foot.

3.1.2 The SCONE software

SCONE ([SCONE Software 2019b](#)) is an optimization and control software framework for predictive simulations that builds on OpenSim. It is an open source software that allows performing predictive simulations of biological motion through a user - friendly environment. Also, it allows users with a Lua scripting interface. In SCONE, simulations are performed through scenarios.

Each scenario is composed of several building blocks. First, it contains a model of a human, an animal or a robot. Also, it includes the objective that defines the goals that the user wants to optimize (this can be a weighted combination of different goals). Moreover, the controller that generates the input for the actuators or muscles of the model is included in the scenario. Last but not least, it consists of the optimizer that takes the free parameters of the problem and optimize them for the objective chosen by the user.

The models used in SCONE can be 2 - Dimensional (2D) or 3D musculoskeletal or other type OpenSim models. Nevertheless, there is a requirement that the model contains torque - driven actuators or muscle - tendon units. Also, the model needs collision shapes and contact models to simulate contact reaction forces and limit forces for simulating forces generated by bones and tendons when joints reach their limits.

Concerning the controller, there are two already implemented controllers. First, the feed - forward controller that creates fixed patterns based on a function. Also, the feedback controller that is based on sensor information and generates inputs for actuators. In this thesis, we adopted the reflex

controller proposed by Ong et al. (Geijtenbeek, 2019). This controller was purposed for the gait motion. The function of the controller was based on the positive feedback from the Golgi tendon organs, and on the length and velocity feedbacks. Moreover a Proportional Derivative (PD) helped to maintain body balance by adjusting hip muscles to limit trunk's lean (Russo et al., 2020). Next, we provide the equations for the simulation of muscles:

Feed-forward simulation:

$$u_c = k_c \quad (3.1)$$

Length feedback:

$$u_L = k_L \cdot \max(0, (\tilde{l}(t - t_d) - l_0)) \quad (3.2)$$

Velocity feedback:

$$u_V = k_V \cdot \max(0, (\tilde{v}(t - t_d))) \quad (3.3)$$

Force feedback:

$$u_f = k_f \cdot \tilde{f}(t - t_d) \quad (3.4)$$

where k_c is a constant, k_L, k_V and k_F are the gains of the reflex controller and l_0 is the threshold value for the muscle length and is defined as the length offset of the stretch response.

PD balance controller:

$$u_{PD} = k_p(\theta(t - t_d) - \theta_0) + k_v \cdot \dot{\theta}(t - t_d) \quad (3.5)$$

where k_p, k_v are the proportional and derivative gains of the controller, and θ_0 the desired forward lean angle.

In all equations, k_p is the time delay depending on the muscle proximity to the vertebral column. Also, the muscle length l , contraction velocity v and force f are all normalized to optimal length (l_{opt}), and maximum isometric force (f_{max}) as described by:

$$\tilde{l} = \frac{l}{l_{opt}}, \quad \tilde{v} = \frac{v}{l_{opt}}, \quad \tilde{f} = \frac{f}{f_{max}}, \quad (3.6)$$

The simulation that the controller provides is associated to muscle activation through first-order dynamics:

$$\frac{d\alpha}{dt} = \frac{u - \alpha}{\tau} \quad (3.7)$$

where α, u, τ are the muscle activation, muscle stimulation and dynamic time constant (with value of 0.01s) accordingly.

Finally, the optimizer identifies the parameters in order to minimize or maximize the objective function by executing the simulation multiple times

and each time adjusting the parameters based on the result. The optimizer repeats until the number of maximum iterations is met or there is no more improvement of the objective function evaluation. The Covariance Matrix Adaptation Evolutionary Strategy (CMA-ES) method is used to optimize the objective of each scenario. The parameters of the optimizer are the samples per iteration and the maximum number of iterations.

3.1.2.1 Objective functions

The objective function in a predictive simulation can be the Center of Mass (COM) position, the energy consumption, the gait speed or weighted combination of them. The goal is to create a motion that optimally performs that task. The parameters that are being optimized are the reflex gains and offsets. The basic components of a cost function used in SCONE are the following:

- **A parameter that penalizes the model when falling based on the termination height:** This parameter is defined as the ratio between the COM height to the initial state:

$$\frac{COM_{height}}{initialCOM_{height}} < th \quad (3.8)$$

The penalty value is give by the next formula:

$$p_{stability} = w_{stability} \cdot \left(\frac{time_{max} - time_{sim}}{time_{max}} \right) \quad (3.9)$$

where th is the threshold for height, $time_{max}$ is the maximum duration of the simulation, $time_{min}$ is the time after which the simulation is terminated and $w_{stability}$ the weight of that penalty.

- **A penalty that minimizes the effort:** The metabolic model of Umberger (Umberger, GERRITSEN, and Martin, 2003; Umberger, 2010), with updates from Uchida is used in order to calculate the effort (Uchida et al., 2016) as described by the next formulas:

$$p_{effort} = w_{effort} \cdot effort \quad (3.10)$$

$$effort = \frac{basalEnergy + \sum_{n=1}^{N_{muscles}} (totHeatRate_i + mechWorkRate_i) \cdot mass_i}{distance \cdot mass_{model}} \quad (3.11)$$

where $totHeatRate$ is the total heat rate and $mechWorkRate$ the mechanical work rate.

- **Penalties for exceeding desired joint ranges.** This penalty evaluates the differences between the desired angles and the actual ones.

$$p_{joints} = w_{joints} \cdot |jointsRanges_{model} - jointsRangestarget| \quad (3.12)$$

where "model" refers to values recorded in simulation and "target" refers to desired ranges.

The total cost function is given by the summation of all components of the objective function:

$$costFunction = p_{stability} + p_{effort} + p_{joints} \quad (3.13)$$

3.1.3 The MOCO tool

OpenSim Moco is a software toolkit for optimizing the motion and control of musculoskeletal systems (MOCO 2020b). It uses the direct collocation method in order to solve quickly problems of trajectory optimization. Users can use Moco to solve not only motion tracking problems, but also parameter optimization and motion prediction problems, model fitting, electromyography-driven simulations, and simulations for device design using any OpenSim model and already implemented cost functions. The core library of Moco is written in C++, but users can also work with Python, Matlab and XML interfaces (Dembia et al., 2020). An overview of the tool is presented in Figure 3.8.

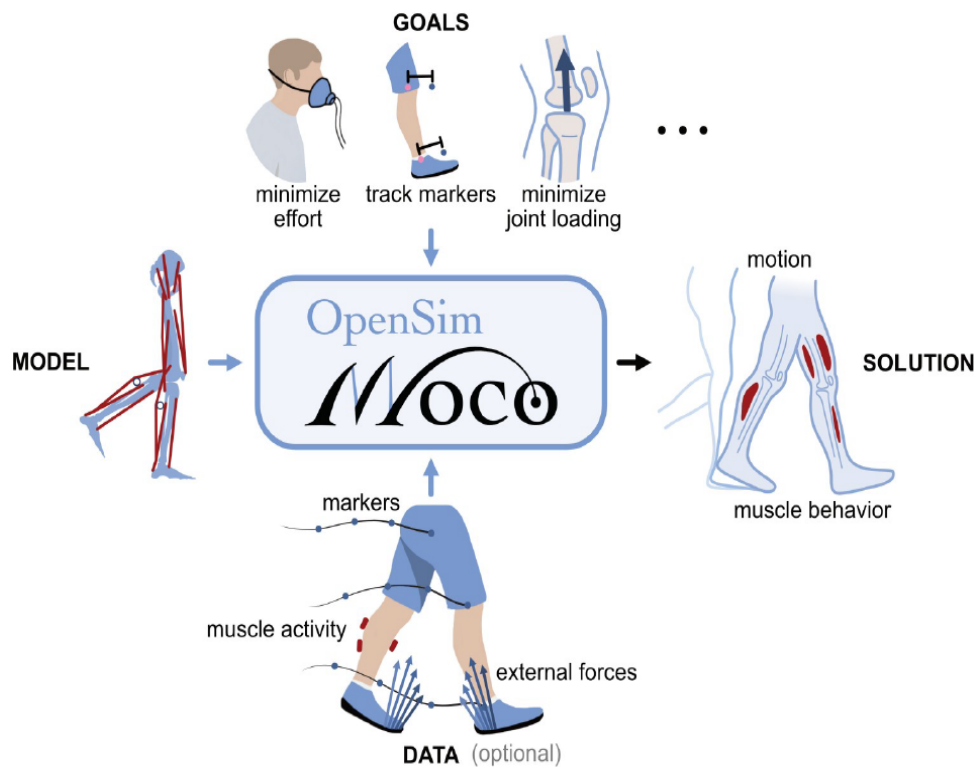


FIGURE 3.8: Overview of OpenSim Moco. It produces the optimal motion and muscle behavior for an OpenSim musculoskeletal model, given goals to achieve during the motion and/or reference data. Reproduced from (Dembia et al., 2020).

Moco is built as a compilation of classes. The user can define the problem within the "MocoProblem" class and use the "MocoSolver" class to solve it. These two classes are nested into the "MocoStudy" class. Also, there is the "MocoSolution" class, which allows the user to plot and visualize the solution of the study created. The organization of the cornerstone Moco classes is presented in Figure 3.9.

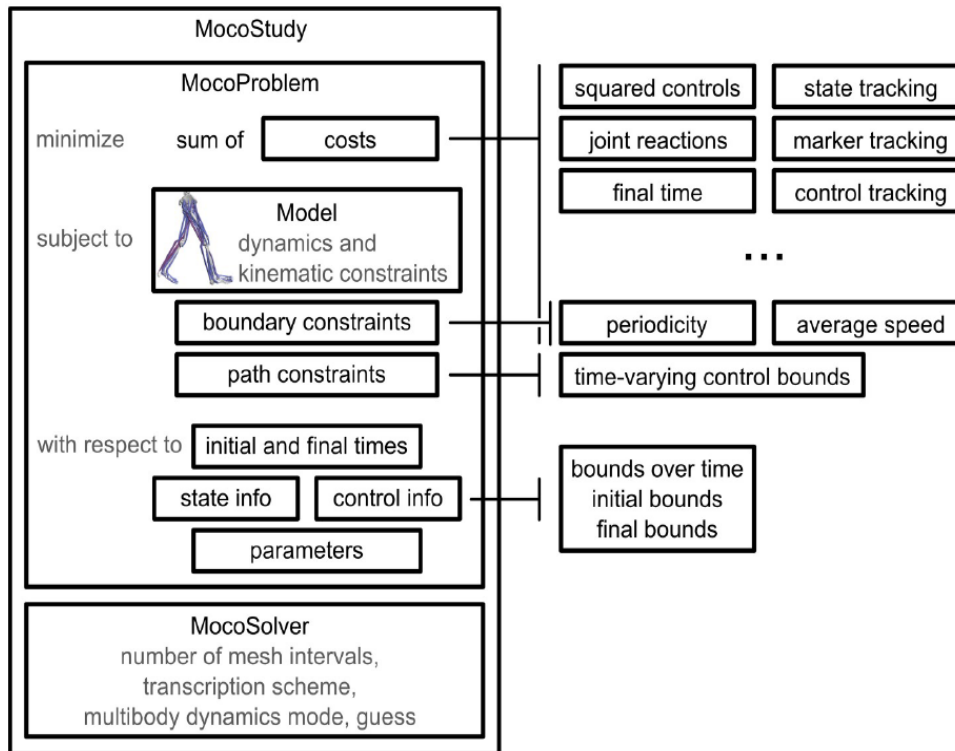


FIGURE 3.9: Organization of basic Moco classes. Overview of MocoStudy. Reproduced from (Dembia et al., 2020).

A "MocoProblem" is a list of "MocoPhases". Nevertheless, Moco supports only single - phase problems. The "MocoProblem" class contains the following elements (as shown on Figure 3.9):

- **cost terms:** Users can choose from multiple costs (duration of motion, deviation from an observed motion, effort, joint reaction loads, etc.) and the weighted sum of the squared controls is being minimized. All goals can be found in the "MocoGoal" class.
- **multibody dynamics, muscle dynamics, kinematic constraints:** Moco uses the musculoskeletal models from OpenSim to obtain multibody dynamics, muscle dynamics and kinematic constraints. The equations are provided by Simbody multibody dynamics library (SimBody n.d.[b]).
- **boundary constraints:** Users can enforce constraints concerning the initial and final state in order to impose periodicity, average speed or symmetry.

- **path constraints:** A function of time (for example for muscle excitation) can be constrained in specified range using the "Moco Control Bound Constraint" class.
- **parameter optimization:** Any property of the model can be optimized.
- **bounds on variables:** Values of initial and final time, states and controls can be bounded.

Moco includes a continuous and differentiable muscle model named "De-GrooteFregly2016Muscle" (De Groote et al., 2016) suitable for the optimization method. Moreover "SmoothSphereHalfSpaceForce" contact model is used to model compliant contact forces (Serrancolí et al., 2019).

3.1.3.1 Objective functions

Moco provides a library of implemented goals like minimizing effort, joint loading, or deviation from marker data. The "Moco Goals" used in this thesis were the "MocoStateTrackingGoal" and the "MocoControlGoal".

"MocoStateTrackingGoal" is used for tracking joint angles, activations etc. This goal is translated as the squared difference between a reference state variable value and a state variable value, summed over the state variables for which a reference is provided, and integrated over the phase.

"MocoControlGoal" is used for minimizing the sum of the absolute value of the controls raised to an exponent (greater or equal to 2, default value is 2) over the phase. In our case squared muscle activation is minimized. The goal is computed by the following formula:

$$\frac{1}{d} \int_{t_i}^{t_f} \sum_{c \in C} w_c |x_c(t)|^p dt \quad (3.14)$$

where:

d : the displacement of the system,

C : the set of the control signals,

w_c : the weight for the control C ,

x_c : the control signal c , and

p : the exponent.

3.2 Predictive simulation of landing with SCONE

In this section we demonstrate the simulation setup in SCONE. This simulation was conducted in order to acquire a motion of a single - leg landing and use it as initial guess for the upcoming Moco simulations.

3.2.1 Simulation setup

First the model was imported to OpenSim to apply an initial configuration and define the desired initial and final states of the motion. The initial state of

the model for landing motion was defined by assigning specific values to the available DoFs. The initial height was set to 30cm height. To achieve this, the DoF corresponding to the pelvis vertical translation was set to 1.25.

Pelvis is connected with the ground with a floating joint of 6 DoFs with an initial translation value of 0.95 m along the vertical axis. The difference between this value and the one we imposed is the desired 30 cm of initial height. Subsequently, we modified the DoFs of both lower - limbs to achieve a single - leg landing with the left foot. The left hip flexion angle was set to 5° , the left knee flexion angle was set to 12° and the left ankle angle was set to 34° . Furthermore, the DoFs of the right - limb were locked to specific values to prevent it from touching the ground at contact phase. The right hip flexion was locked at 25° , the right knee angle was locked at 120° and the right ankle angle at 120° . Moreover, all DoFs of the upper body were set at their default values with only the exception of pelvis vertical translation as previously mentioned. The initial state of the model is displayed in Figure 3.9.

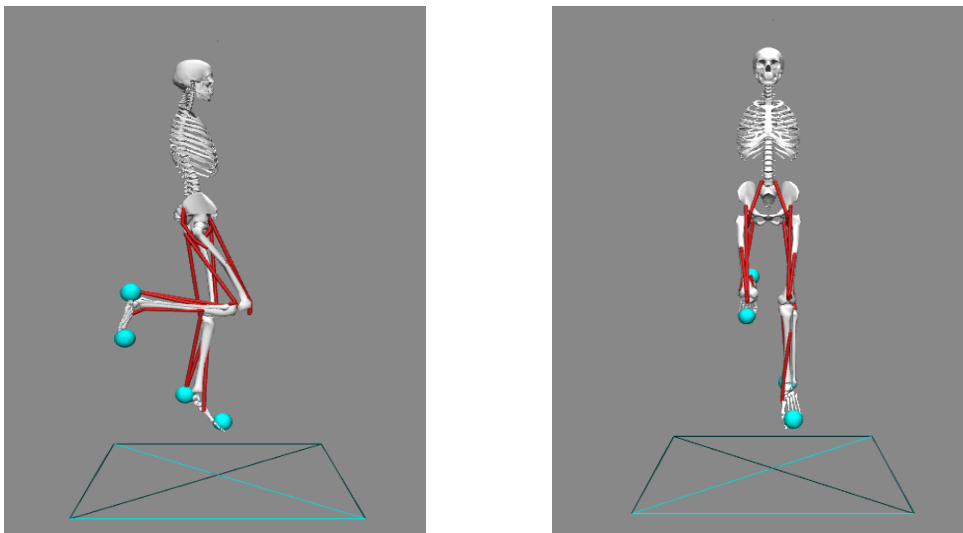


FIGURE 3.9: Initial state of the musculoskeletal model "Human0916" used for the predictive simulations in SCONE. Sagittal (right) and Frontal (left) planes.

Next, we will take a look into the Optimizer and its components. The Optimizer contained the previously described model, a reflex controller and a composite measure which were presented in subsection 3.1.2. The reflex controller included "MuscleReflex" entries that simulated proprioceptive reflexes and a "BodyPointReflex" that simulated the vestibular reflexes. Moreover, each reflex defined a reflex arc with specific gain, offset and delay. Also, the composite measure contained several measures. The first measure was the "ReactionForceMeasure" that was used to minimize the GRF contact with the ground. Furthermore, a range of accepted values for the GRF was defined and if their values were out of that range a penalty was applied. Then, a "BalanceMeasure" was added which was used for keeping the model from falling. Finally several "DofMeasures" for ankle and knee angles were defined to achieve the desired landing (a single - leg soft landing). More specifically,

we defined ranges of accepted values for the angles. Penalties were applied when those ranges were violated.

The components of the cost function that were included in our study are described next:

- **A parameter that penalized the model when falling based on the termination height**
- **A penalty that minimized the effort**
- **Penalties for exceeding desired joint ranges.** The desired joint range for the ankle was: [25°, 35°] (positive dorsiflexion). For the knee was: [−60°, −30°] (positive flexion) and for the pelvis tilt was: [−50°, 0°].

Next, we present a general overview of the script used for this simulation setup and its basic components.

```

1 Optimizer {
2   # definition of model used in simulation
3   OpenSimModel { }
4   Controller {
5     type = ReflexController
6     # Muscle length reflexes
7     MuscleReflex {}
8     # Vestibular reflexes
9     BodyPointReflex {}
10  CompositeMeasure {
11    # measure to minimise GRF
12    ReactionForceMeasure {}
13    # measure for not falling
14    BalanceMeasure {}
15    # measure for desired joint ranges
16    DofMeasure {}
17  }
18 }
```

3.3 Predictive simulation of landing with MOCO

In this section we present the simulation performed in MOCO in order to create case studies of single - leg landings using as an initial guess the predicted motion from SCONE. First, we describe the basic simulation setup in MOCO. Then, we introduce the pipeline for augmenting model complexity. Finally we examine one by one the examined case studies that answer to multiple what - if scenarios.

3.3.1 Simulation setup

Here we present the main outline of the Moco study that is deployed to assess any of the subsequent what - if - scenarios. This is accomplished with Python scripting taking advantage of the Python bindings available for Moco. The order of the commands follows the same hierarchy as presented in Figure 3.9.

Therefore, we created a "MocoProblem" object and a "MocoSolver" object as parts of the high - level "MocoStudy" object. The following subsections are dedicated to describe each distinct block of the overall workflow.

3.3.1.1 Model operations

At first, certain modifications were applied to the musculoskeletal model. The muscle model was selected as the "DeGrootefregly" muscle type, since this model is compliant with Moco. The passive fiber forces were ignored and the active fiber force width for all muscles was scaled with a factor of 1.5. Ideal torque actuators were appended to the DoFs that were not actuated by muscles. Also, reserve actuators were added to all DoFs to act supplementary to the already present muscles. The maximum torque was set to 100 Nm.

```

1 import opensim as osim
2
3 model = osim.ModelProcessor("Gait2392.osim")
4 # turn off tendon compliance
5 model.append(osim.ModOpIgnoreTendonCompliance())
6 # replace with "DeGrootefregly" muscle type
7 model.append(osim.ModOpReplaceMusclesWithDeGrootefregly2016())
8 # turn off passive fiber forces
9 model.append(osim.ModOpIgnorePassiveFiberForcesDGF())
10 # Scale the active fiber force curve width
11 model.append(osim.ModOpScaleActiveFiberForceCurveWidthDGF(1.5))
12 # add reserve actuators to the model
13 model.append(osim.ModOpAddReserves(100))

```

As seen in Figure 3.1 our workflow is divided in two parts. First, we performed tracking studies using the MocoTrack interface and the previously adjusted model. Then the MocoStudy class was used to predict the what-if scenarios.

3.3.1.2 Augmenting model complexity - MocoTrack

The aim of the tracking study was twofold. First, we used it to create initial guesses for our optimization studies. Secondly, this helped us to chain three different simulations where each new one features a higher complexity musculoskeletal model and takes as input the optimal solution of the previous one. Model complexity refers to its total number of DoFs and total number of available muscle - tendon units. As we already described in subsection 3.2.1 the objective of the first simulation using SCONE was to obtain an initial guess for the upcoming Moco studies. Therefore, for the first MocoTrack we used as reference trajectory the SCONE simulation output. The selected model was the Gait2354 model. The output of this tracking study served as input for an additional tracking study, this time with the Gait2392 model.

The simulation initial and final time were identical to these of the SCONE trajectory. The track tool instance was connected to the problem. Instantly the "MocoStateTrackingGoal" was added to the tracking study. Some states of the model were edited to further assist the trajectory solution. The bounds for these DoFs were set based on the initial and final states of the predicted

motion from SCONE simulation. A detailed overview of these bounds is presented in Table 3.1. For the DoFs that are not included in this table no bounds were set. Moreover, we applied bounds for the initial state and the entire motion for the activation of all muscles. At the first time instant the activation of all muscles was set to zero. Furthermore, both models consists of identical DoFs and the following description concerns both of them. An overview of the commands that were used to setup the analysis is presented next:

```

1
2 # set MocoTrack tool
3 track = osim.MocoTrack()
4
5 # define model
6 track.setModel()
7 # set table containing values of model state variables
8 track.setStatesReference()
9 # set initial time
10 track.set_initial_time()
11 # set final time
12 track.set_final_time()
13
14 # initialize MocoTrack in the study
15 study = track.initialize()
16 # access MocoProblem within the study.
17 problem = study.updProblem()
18
19 # set bounds for all state variables for phase 0
20 problem.setStateInfoPattern('/forceset/*/activation', osim.
    MocoBounds(0,1), osim.MocoInitialBounds(0))
21 problem.setStateInfo("/jointset/../../../../value",
22                      osim.MocoBounds(), osim.
    MocoInitialBounds(), osim.MocoFinalBounds())

```

DoFs	Bounds	Initial Bounds	Final Bounds
pelvis_ty	(0.7, 1.25)	1.25	(0.75, 0.85)
pelvis_ [†]	(-0.01, 0.01)	0	-
lumbar_ [†]	(-0.01, 0.01)	0	-
hip_flexion_l	(0.08, 0.5)	0.087	-
hip_ [†]	(-0.01, 0.01)	0	-
subtalar_angle [‡]	(-0.01, 0.01)	0	-
mtp_angle [‡]	(-0.01, 0.01)	0	-

[†] This stands for all DoFs of the joint if they are not explicitly defined.

[‡] This stands for both right and left joints.

TABLE 3.1: Bounds for the DoFs of Gait2354 and Gait2392 OpenSim models for MOCO Track tool.

3.3.1.3 Predictive simulation settings - MocoStudy

Regarding prediction in Moco, we created a new study with the same commands as previously. Since this class was used to execute all the what - if scenarios, the settings for each case study will be presented in the following sections. The common setting for all cases was the initial guess which was set as the MocoTrack output.

```
1 # set MocoStudy
2 study = osim.MocoStudy()
3
4 # access MocoProblem within the study.
5 problem = study.updProblem()
6 #Set the model
7 problem.setModel()
8 #Set time bounds
9 problem.setTimeBounds()
10
11 # set bounds for all state variables for phase 0
12 problem.setStateInfoPattern('/forceset./*/activation', osim.
    MocoBounds(0,1), osim.MocoInitialBounds(0))
13 problem.setStateInfo("/jointset/../../../../value", osim.MocoBounds(),
    osim.MocoInitialBounds(), osim.MocoFinalBounds())
```

3.3.1.4 Post - processing operations

Moreover, we developed scripts to perform post - processing operations on each estimated by Moco predicted trajectory. The parameters of interest were normalized tendon forces, GRF, kJRF and kJRM. Initially, we used the OpenSim Analyze Tool to obtain the muscle tendon forces. Also, JRA was implemented for the left knee joint. The JRA pipeline requires muscle forces and all external forces applied to the model. The external forces were acquired from the estimated solution and the contact forces estimated from the sphere contact model expressed in the ground frame. Since force is a bound vector the point of application is also required to appropriately estimate joint reaction loads. Towards this direction, we deployed a method for estimating the CoP (YH, n.d.), as it serves the actual GRF application point. As depicted in Figure 3.10, the contact between the foot and the ground leads to the development of contact forces between these two parts. These forces can be summed into a ground force vector \mathbf{F} and a free torque vector T_z , which is applied at the CoP.

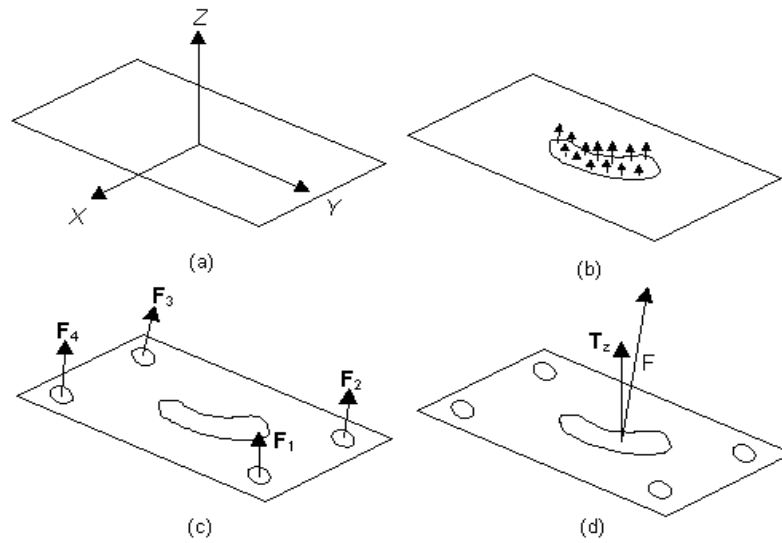


FIGURE 3.10: Computation of the Center of Pressure. Reproduced by (YH, n.d.).

Assuming that the true origin is the O' at (a,b,c) in Figure 3.11, then the Z component is 0. Thus, the moment caused by F about the true origin plus T_z is equal to the moment measured from the plates. These are described by the next formulas:

$$M = [x - a, y - b, -c] \times [F_x, F_y, F_z] + [0, 0, T_z] \quad (3.15)$$

$$\begin{bmatrix} M_x \\ M_y \\ M_z \end{bmatrix} = \begin{bmatrix} 0 & c & y - b \\ -c & 0 & -(x - a) \\ -(y - b) & (x - a) & 0 \end{bmatrix} \begin{bmatrix} F_x \\ F_y \\ F_z \end{bmatrix} + \begin{bmatrix} 0 \\ 0 \\ T_z \end{bmatrix} \quad (3.16)$$

or

$$\begin{bmatrix} M_x \\ M_y \\ M_z \end{bmatrix} = \begin{bmatrix} (y - b)F_z + cF_y \\ -cF_x - (x - a)F_z \\ (x - a)F_y - (y - b)F_x + T_z \end{bmatrix} \quad (3.17)$$

Finally:

$$x = -\frac{M_y + cF_x}{F_z} + a, \quad y = \frac{M_x - cF_y}{F_z} + b \quad (3.18)$$

$$T_z = M_z - (x - a)F_z + (y - b)F_x \quad (3.19)$$

Based on the previous analysis, the CoP can be calculated from the values of the GRF: F_x , F_y and F_z , the moment caused by the GRF: M_x , M_y and M_z , and finally the location of the true origin a , b and c .

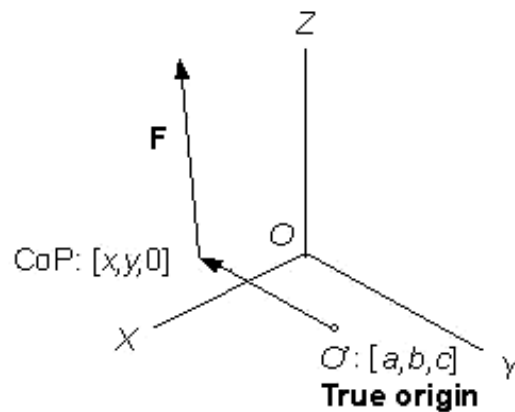


FIGURE 3.11: True origin of the CoP. Reproduced by (YH, n.d.).

A Python code snippet that executes all these post - processing operation is presented in the following block:

```

1
2 #export normalized tendon forces from the Moco solution using
   Analyze tool
3 outputPaths.append('.*tendon_force')
4 outputTable = study.analyze(solution, outputPaths)
5
6 # export GRF expressed in ground frame
7 externalForcesTableFlat = osim.createExternalLoadsTableForGait()
8 # expresses GRF in CoP
9 express_GRF_inCop('GRF.sto')
10
11 # JRA for the knee joint
12 JR_paths.append('.*reaction_on_child')
13 states = solution.exportToStatesTable()
14 controls = solution.exportToControlsTable()
15 JR_outputs_table = osim.analyzeSpatialVec(model, states,
   controls, JR_paths).flatten()
16
17 # express JRA in Child frame
18 express_jra_inChild()

```

3.3.2 Initial height case study

In this section, we describe the simulation setup of drop - landing from different initial heights. The model used was *Gait2392.osim*. The *pelvis_ty* value was modified as presented in Table 3.2 in order to achieve landings from 30, 35, 40, 45, 50 and 55 cm of height. For every height value a new study was created with the parameters described previously. The solution acquired with the track tool was used as an initial guess for the solver. Also, the "MocoControlGoal" goal was added to the problem with a weight of 0.001.

Height	Pelvis_ty
30	1.25
35	1.30
40	1.35
45	1.40
50	1.45
55	1.50

TABLE 3.2: Moco values for *pelvis_ty* based on landing height as displayed in OpenSim.

Figure 3.12, we demonstrate the initial pose of the model from these different drop - landing heights. As it can be observed, apart from the *pelvis_ty* value which was adjusted in order to achieve multiple initial landing heights, all the other DoFs remained identical for the initial state in all scenarios. It should be mentioned that a deviation of 0.01cm of the selected landing height was allowed in all cases, as with all DoFs of the model.

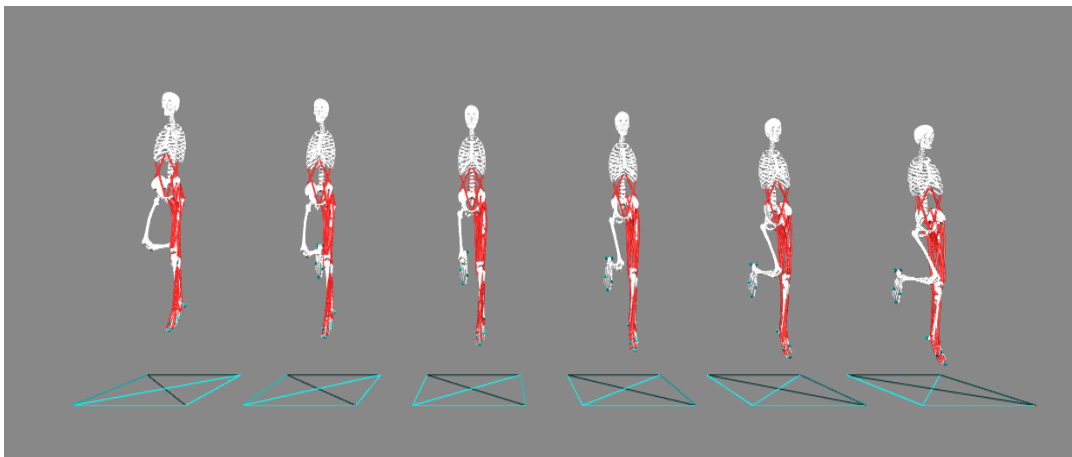


FIGURE 3.12: Initial state of the model for different drop - landing heights.

3.3.3 Hip rotation case study

In this section we describe the analysis parameters used to conduct several studies for drop - landings with different values of hip rotation for the landing leg. We examined cases where the hip was internally or externally rotated for the entire trajectory. In total we created 13 studies, 6 for hip internal rotation, 6 for hip external rotation and 1 for no hip rotation. The angles of external and internal rotation examined were 5°, 10°, 15°, 10°, 25° and 30°. The model in its initial configuration with internally and externally rotated hip (0°, 10°, 20°, 30°) is presented in Figure 3.13 and Figure 3.14 respectively.

DoFs	Angle (degrees)							Bounds
hip_internal_rotation	0	5	10	15	20	25	30	
hip_external_rotation	0	5	10	15	20	25	30	

TABLE 3.3: Overview of investigated values for hip joint rotation.

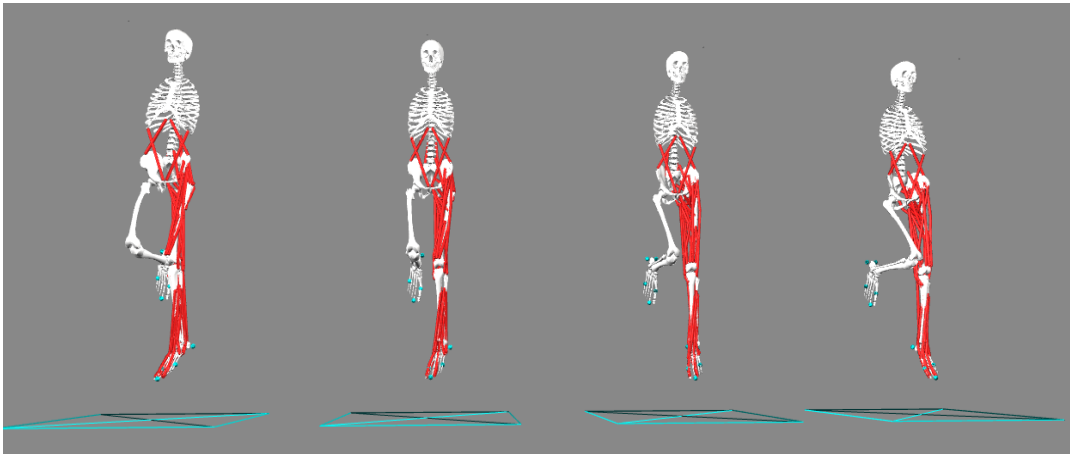


FIGURE 3.13: Initial state of the model for 0°, 10°, 20° and 30° of hip internal rotation.

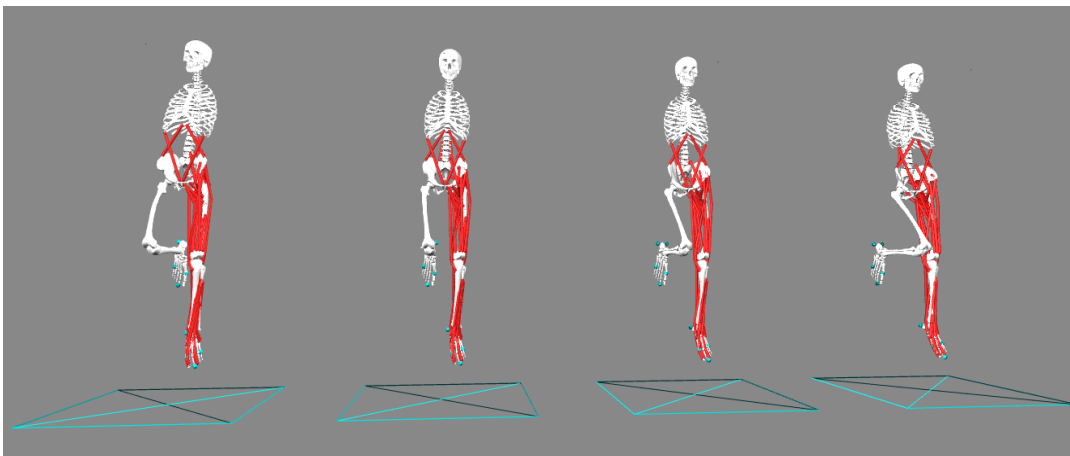


FIGURE 3.14: Initial state of the model for 0°, 10°, 20° and 30° of hip external rotation.

Again, we used the *Gait2392* OpenSim model, and the previously tracked solution was used as an initial guess for the solver. Also, the "MocoControlGoal" was added to the problem with a weight of 0.001. In Table 3.4 we display the bounds assigned to all DoFs in the Moco studies.

DoFs	Initial bounds	Final bounds	Bounds
pelvis_ty	1.25	(0.75, 0.85)	(0.7, 1.25)
pelvis_*	0	-	(-0.57, 0.57)
hip_flexion_r	30°	-	(29°, 30°)
hip_rotation_r	0°	-	(-0.01°, 0.01°)
hip_adduction_r	0°	-	(-0.01°, 0.01°)
knee_angle_r	-120°	-	(-121°, -119°)
ankle_angle_r	0°	-	(-0.57°, 0.57°)
subtalar_angle_r	0°	-	(-0.57°, 0.57°)
mtp_angle_r	0°	-	(-0.57°, 0.57°)
hip_flexion_l	5°	-	(4.5°, 28.5°)
hip_rotation_l	-	-	(v-0.57°, v+0.57°)
hip_adduction_l	-	-	-
knee_angle_l	-11.5°	-	(-57°, 0°)
ankle_angle_l	-34°	-	(-34°, 45°)
subtalar_angle_l	-	-	(-2.85°, 2.85°)
mtp_angle_l	0°	-	(-5.73°, 5.73°)

This stands for all DoFs of the joint if they are not explicitly defined.

TABLE 3.4: Values for DoFs of the model for different values of left hip rotation scenarios

For *hip_adduction* of the left lower limb we did not assign bounds because it is highly related to *hip_rotation* and we wanted to examine how it will respond to different conditions of hip rotation.

3.3.4 Trunk orientation case study

In this section we outline the settings for the scenarios that evaluate deviations of the trunk DoFs. This is achieved through modifying the lumbar joint. It consists of three DoFs, namely flexion - extension, right - left bending and external - internal rotation. The assessed flexion angles were: 5°, 10°, 15°, 20°, 25° and 30° degrees, while for extension were: 5°, 10°, 15° and 20°. Moreover, the angles studied for right - left bending and external - internal rotation were: 0°, 5°, 10°, 15°, 20°, 25° and 30°. Also, an upright position with no flexion, bending or rotation was considered. These scenarios are presented in Table 3.5. We also include the bounds for the DoFs of interest for the entire prediction pipeline. It should be stated that these bounds are active only for the lumbar joint generalized coordinate under consideration, while all other lumbar DoFs are equal to zero.

DoFs	Angle (degrees)							Bounds
lumbar_flexion	0	5	10	15	20	25	30	$(v-0.57, v+0.57)^\dagger$
lumbar_extension	0	5	10	15	20	-	-	"
lumbar_rotation	0	5	10	15	20	25	30	"
lumbar_bending	0	5	10	15	20	25	30	"

[†] v is the value of the generalized coordinate under consideration for each scenario.

TABLE 3.5: Overview of investigated values for lumbar joint DoFs. We also describe the bounds for each value.

In Figure 3.15, Figure 3.16 and Figure 3.17 we display the initial state of the model for selected angles of trunk flexion - extension, right - left bending and internal - external rotation respectively.

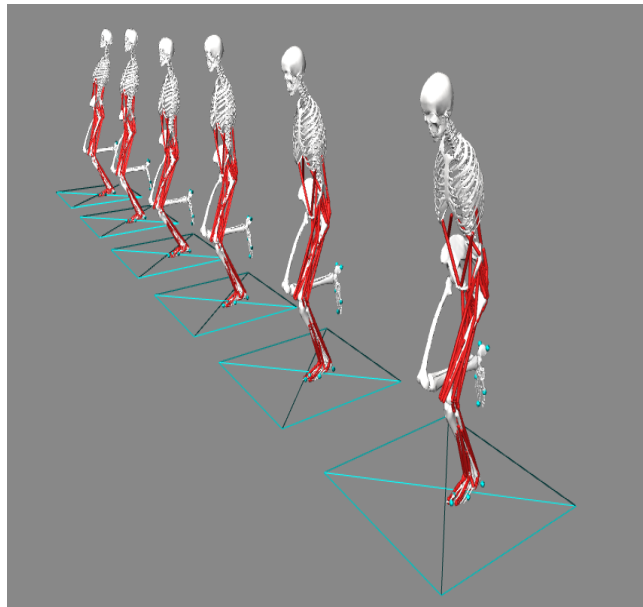


FIGURE 3.15: Initial state of the OpenSim model for different values of lumbar flexion - extension.

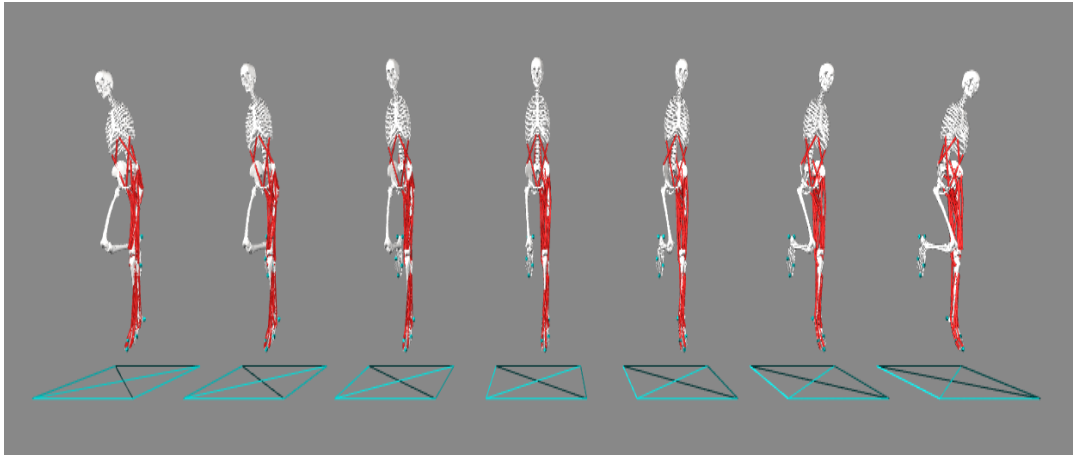


FIGURE 3.16: Initial state of the OpenSim model for different values of lumbar right - left bending.

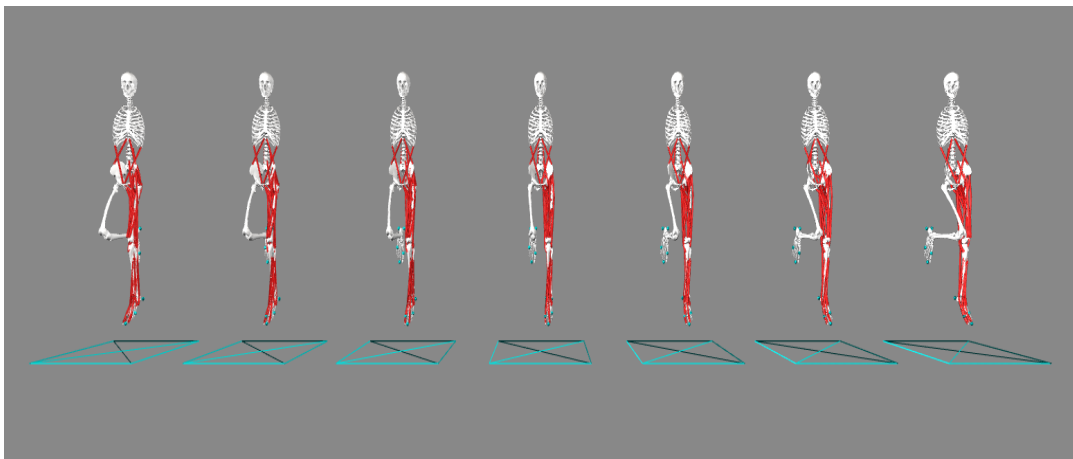


FIGURE 3.17: Initial state of the OpenSim model for different values of lumbar internal - external rotation.

For all of the above cases, different studies were produced using the initial guess described previously and certain bounds for the initial and final states that are presented in Table 3.6.

DoFs	Initial bounds	Final bounds	Bounds
pelvis_ty	1.25	(0.75, 0.85)	(0.7, 1.25)
pelvis_* [†]	0°	-	(-0.57°, 0.57°)
hip_flexion_r	30°	-	(29°, 30°)
hip_rotation_r	0°	-	(-0.01°, 0.01°)
hip_adduction_r	0°	-	(0.01°, 0.01°)
knee_angle_r	-120°	-	(-121°, -119°)
ankle_angle_r	0°	-	(-0.57°, 0.57°)
subtalar_angle_r	0°	-	(-0.57°, 0.57°)
mtp_angle_r	0°	-	(-0.57°, 0.57°)
hip_flexion_l	5°	-	(4.5°, 28.5°)
hip_rotation_l	0°	-	(-0.01°, 0.01°)
hip_adduction_l	0°	-	(-0.01°, 0.01°)
knee_angle_l	-11.5°	-	(-57°, 0°)
ankle_angle_l	-34°	-	(-34°, 45°)
subtalar_angle_l	-	-	(-2.86°, 2.86°)
mtp_angle_l	0°	-	(-0.57°, 0.57°)

[†] This stands for all DoFs of the joint if they are not explicitly defined.

TABLE 3.6: Bounds for the DoFs of the model for the trunk orientation case study.

For all the trunk cases, both the track tool and the prediction with initial guess were examined in order to compare them. Moreover different weights for the *effort goal* were examined and compared for several cases in order to observe deviations of the GRF and muscle activation values.

3.3.5 Muscle force of knee joint agonists and antagonists case study

In this section we present the case studies that were performed to investigate how permutations regarding the max isometric force of the knee joint agonists and antagonists muscle groups affect the ACL injury indicators. Muscle fatigue is defined as the decrease in maximum force (Bigland-Ritchie et al., 1995; SimTK - confluence 2011a). Towards this objective, we edited the values of max isometric forces to simulate weakness and strength of specific muscle groups, namely the quadriceps and the hamstrings muscles. To simulate strong muscles we enlarged max isometric force by 35 percent and to simulate weak muscles we reduced their max isometric force by 35 percent in accordance with (Afschrift et al., 2014; Jing et al., 2017; Daniel et al., 2017).

The model used for these scenarios was *Gait2392*. The quadriceps muscles include rectus femoris, vastus medialis, vastus lateralis and vastus intermedius. Hamstrings muscle group combines the semimembranosus, semitendinosus, biceps femoris long head and biceps femoris short head.

In Table 3.7 we display the value of the standard max isometric force for each muscle, along with the value when it is weakened or strengthened.

Muscle	max Isometric force	Weak	Strong
Rectus femoris	1169	760	1578
Vastus intermedialis	1365	887	1842
Vastus lateralis	1871	1216	2526
Vastus medialis	1294	841	1746
Semimembranosus	1288	837	1739
Semitendinosus	410	267	554
Bicep femoris long head	896	582	1210
Bicep femoris short head	804	523	1085

TABLE 3.7: Values for max isometric force for all muscles in hamstrings and gastrocnemius muscle groups. Also, the modified max isometric forces for these muscles for their strengthening or weakening are included.

The bounds used for the initial and final states were identical to those used in previous cases for the right lower limb. The trunk and the left lower limb DoFs were restricted based on the initial guess and small deviations were allowed. A "MocoControlGoal" was used with a weight of 0.002.

Based on Table 3.7, eight cases were simulated with different combinations of normal, weak and strong muscles. These cases are demonstrated in Table 3.8.

case	Quadriceps	Hamstrings
1	normal	normal
2	normal	strong
3	normal	weak
4	strong	normal
5	weak	normal
6	strong	weak
7	weak	strong
8	weak	weak

TABLE 3.8: Demonstration of the eight cases with different combinations of normal, weak and strong muscles.

3.3.6 Moco Control goal weight case study

In this section, we examined how the "Moco Control goal" affects the outcome of the study. For this, we tested different weight values: 0, 0.1, 0.2, 0.5, 1, 2, 5 and 10. Again, the selected model was the *Gait2392* model, and the tracked solution was the initial guess. Also, the DoFs were bounded as described in previous sections. All parameters were identical for all cases except for the goal weight.

Chapter 4

Results

In this chapter, we present the results of our case studies that reflect parameters associated with ACL injuries. These parameters concern kinematics, GRF, GRM, muscle forces and muscle force ratios of the landing lower limb. Also, we include kJRF and kJRM plots. Finally, tables with values for the previously mentioned parameters at the peak v GRF time instant are introduced. This instant was selected since it is considered the moment of ACL injury occurrence. The kinematics are presented in degrees, the GRF, GRM and JRM are presented with normalized values to Body Weight (BW) of the musculoskeletal model. The muscle forces are presented in Newtons. Moreover, one may notice deviations between the plots and the resulted values on the tables. This is due to an applied filter on the plots. This is only for visualization purposes and does not modify the comparison between the multiple scenarios.

The experiments were conducted using a computer machine with an i7-9700 Intel(R) Core(TM) processor @3.00 GHz, a memory of 16GB, and a Windows 10 64bit operating system. Every simulation scenario required about 45 to 60 minutes to complete regarding the above specifications.

4.1 Initial height case

In this section, we present results concerning single - leg landings from 30, 35, 40, 45, 50 and 55 cm of height as described in subsection 3.3.2.

Initially, we present the predicted kinematics for the hip, knee and ankle joint angles for all examined scenarios (Figure 4.1). As mentioned in subsection 3.3.2, these joints' DoFs were restricted to their respective bounds, although we can observe that there are small deviations among the different cases. First, we can detect that the hip and ankle flexion angles at peak v GRF are increased as the drop - landing height is raised. On the contrary, the knee flexion angle is decreased as the landing height is raised. It should be mentioned that the deviations for these angles between the examined scenarios are less than 10° .

Drop - Landing: Initial Landing Height case study Hip, knee and ankle angles

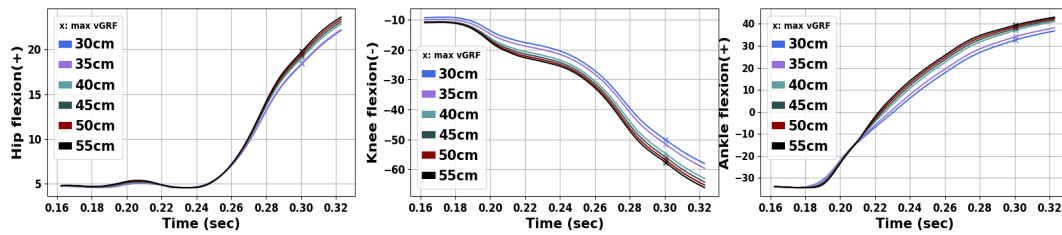


FIGURE 4.1: Hip, knee and ankle kinematics for the initial height case.

Next, we present GRF and GRM of single - leg landings from the same landing heights (Figure 4.2). We can observe that for greater landing heights the pGRF and vGRF values at max vGRF time also increase.

Drop - Landing: Initial Landing Height case study Ground Reaction Forces and Moments (/BW)

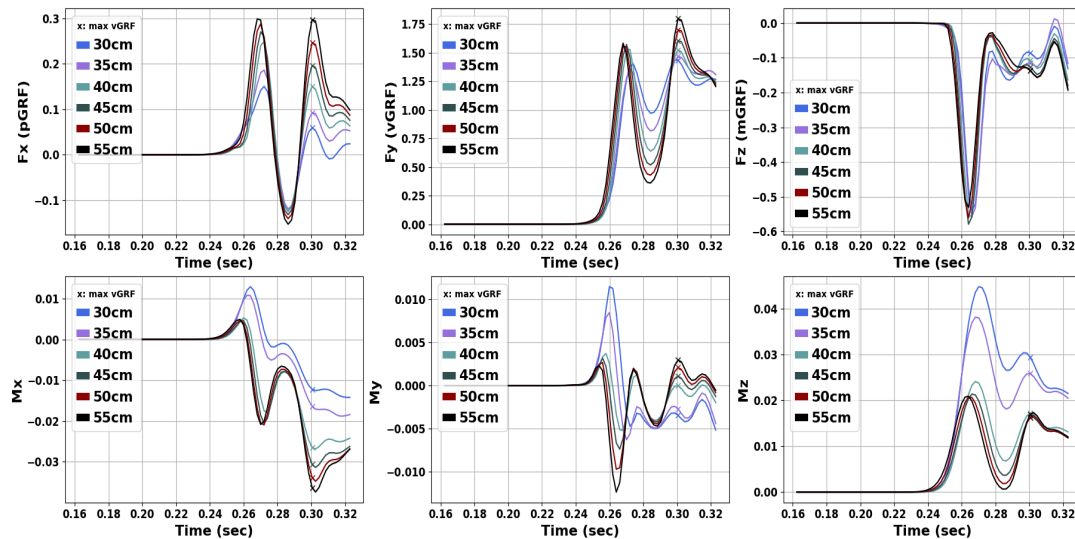


FIGURE 4.2: GRF and GRM for the initial height case study..

Subsequently, in Figure 4.3 we demonstrate JRF and JRM for the knee joint for this case study. As we can observe, the Anterior force (AF) reaches a first peak after IGC and then a greater one after the max vGRF time instant for all cases. Both peaks are greater as the landing height is increased. Nevertheless, at max vGRF no great differences can be detected for the AF among the scenarios. Regarding Compressive force (CF), we can see that the first peak occurs right after IGC with greater values for increased initial heights. Although, at max vGRF time CF is decreased as the landing height is increased. As for the Medial force (MF), a peak value is observed at IGC with greater values for greater landing heights.

Additionally, AbdM obtains a peak value for all examined scenarios around IGC. This peak value is greater for the landings from higher landing heights. Moreover, two External rotation moment (ERM) peaks are spotted for all cases, one after IGC and a second one between IGC and max vGRF.

Furthermore, lower IRM values are observed for higher initial heights with few exceptions. Also, Flexion moment (FM) at max vGRF time is greater for greater initial height scenarios.

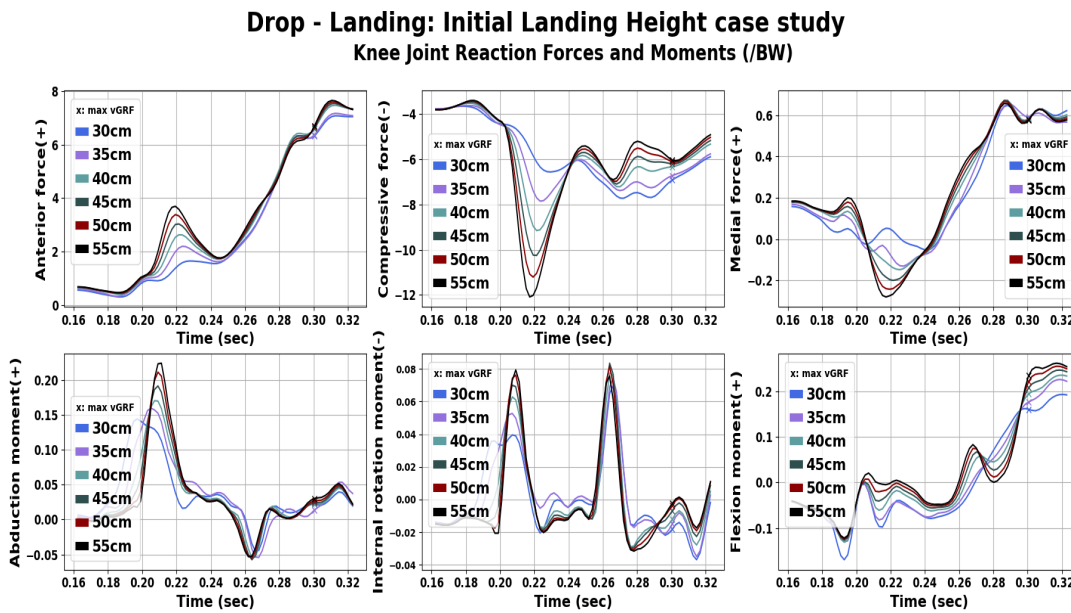


FIGURE 4.3: Knee joint JRF and JRM for multiple drop - landing heights.

Next, in Figure 4.4 we demonstrate muscle forces and muscle force ratios for the studied scenarios. First, we observe that the quadriceps, hamstrings and tibialis anterior forces presents almost identical patterns for all examined scenarios. As a result the Q/H force ratio is almost similar for all cases. At IGC, Q/H force ratio is approximately 3 with lower values for lower initial heights. Then, it obtains greater values (around 10). Moreover, before max vGRF time we observe that for lower heights the ratio obtains greater values, while after that time it receives greater values for increased heights. Also, GTA force ratio appears a peak value after IGC, with increased values for greater heights. At max vGRF no great deviations among different landing heights are observed.

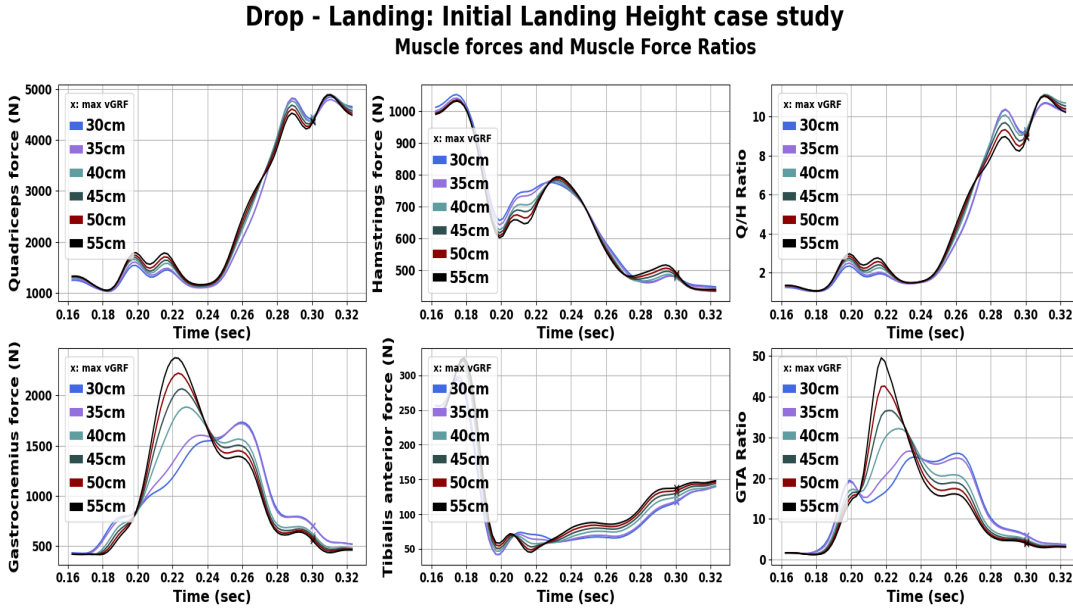


FIGURE 4.4: Muscle forces and muscle force ratios for multiple drop - landing heights.

In Table 4.1 and Table 4.2, values of the previously plotted parameters at the maximum vGRF time instant for all cases are presented. In these tables and in order to compare more easily the different scenarios and validate our observations, the values correspond at time of maximum vGRF.

We can observe that pGRF and vGRF are increased as the landing height is increased. Moreover, GTA force ratio is decreased as the landing height is increased. Also, Q/H force ratio obtains lower values for the landings from 55 and 50 cm.

Case	pGRF	vGRF	mGRF	Q/H_ratio	GTA_ratio
30	0.066	1.436	-0.092	9.243	6.036
35	0.099	1.467	-0.118	9.167	5.914
40	0.160	1.523	-0.109	9.250	4.969
45	0.210	1.604	-0.125	9.083	4.591
50	0.263	1.698	-0.131	8.951	4.289
55	0.319	1.797	-0.130	8.850	4.004

TABLE 4.1: GRF, Q/H force ratio and GTA force ratio at the time instant of peak vGRF for multiple drop - landing heights..

In Table 4.2 we can clearly see that as the landing height is increased, the AF is also increased at peak vGRF time instant. On the other hand, CF decreases as the initial landing height increases. Also, AbdM obtains the greatest value for the landing from 55cm and the lowest one for the landing from 35cm. Moreover IRM is decreased as the landing heights is greater. Finally, FM is also greater for higher initial heights at max vGRF time.

Case	AF(+)	CF(-)	MF(+)	AbdM(+)	IRM(-)	FM(+)
30	6.300	-6.907	0.577	0.021	-0.017	0.160
35	6.334	-6.721	0.587	0.014	-0.014	0.178
40	6.577	-6.339	0.582	0.023	-0.011	0.197
45	6.612	-6.225	0.580	0.025	-0.007	0.213
50	6.652	-6.149	0.577	0.029	-0.004	0.229
55	6.699	-6.093	0.575	0.033	-0.003	0.245

TABLE 4.2: Knee joint JRF and JRM at the time instant of peak vGRF for multiple drop - landing heights.

It should be mentioned that in all figures presented in the current section the results for all scenarios were shifted in time. This was performed in order to synchronize the IGC of all scenarios.

4.2 Hip rotation case

In this section, we present the results concerning single - leg landings with different values of internal and external hip rotation of the landing leg. These angles were set at 0° , 5° , 15° , 20° , 25° and 30° for both cases as described in subsection 3.3.3.

Initially, in Figure 4.5 we provide the hip, knee and ankle flexion angles along with hip adduction and hip rotation angles for the hip internal rotation scenarios. As displayed in Table 3.4, these DoFs were restricted to their respective bounds. For hip, knee and ankle flexion we can detect small deviations between the cases. Nevertheless, hip adduction's bounds were more relaxed and we can identify deviations between the cases. It is noticeable that as we impose greater hip internal rotation angles, the adduction of the hip is also increased.

Drop - Landing: Hip Internal Rotation case study Hip, knee and ankle angles

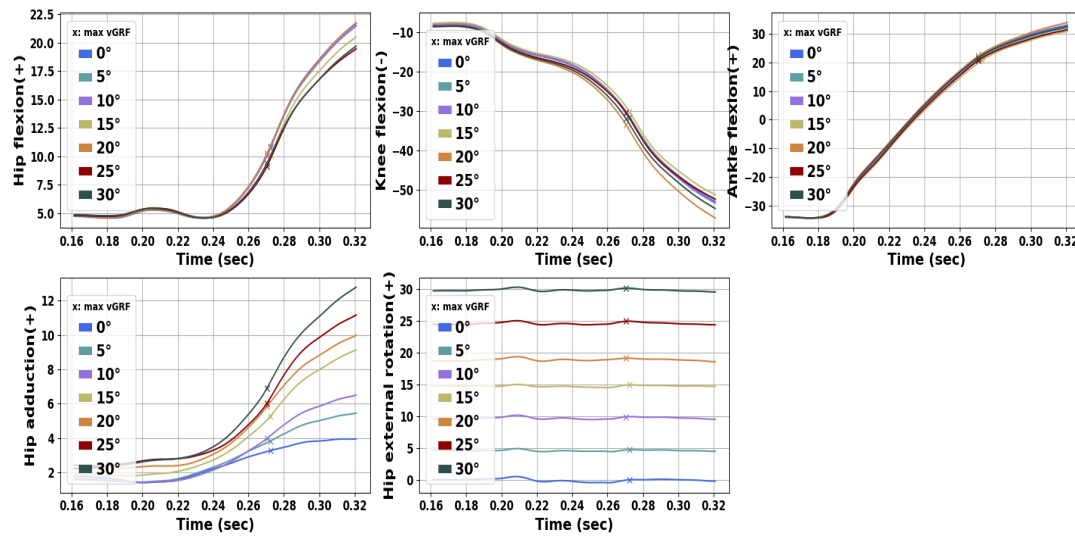


FIGURE 4.5: Hip, knee and ankle kinematics for various hip internal rotation angles.

Subsequently, in Figure 4.6 we demonstrate GRF and GRM for scenarios with different hip internal rotation angles. We can observe that as the hip internal rotation is increased, the vGRF amplitude is higher and for the 30° case it obtains a value greater than 4 times BW. The only exception is for 20° where vGRF derive a significantly smaller value. The same pattern is detected for pGRF at max vGRF.

Drop - Landing: Hip Internal Rotation case study Ground Reaction Forces and Moments (/BW)

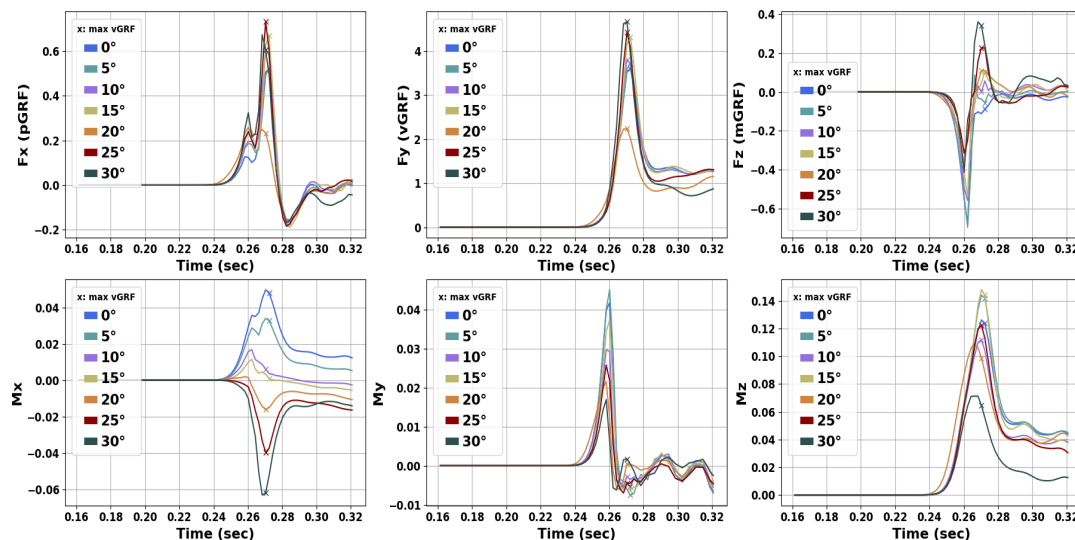


FIGURE 4.6: GRF and GRM for various hip internal rotation angles.

Moreover, in Figure 4.7 we demonstrate kJRF and kJRM for all cases. No great differences can be observed for the AF among the different cases. Also, regarding CF the lower value is detected for the 20° hip internal rotation case around its max vGRF. However, we can notice that the general pattern of this

graphs depicts that as the hip internal rotation increases CF also increases. For AbdM and ERM no comparative observation can be easily made. Nevertheless, FM obtains a peak value around peak vGRF. This peak obtains the greatest value for the 30° hip internal rotation and the lowest for the 20° hip internal rotation scenario.

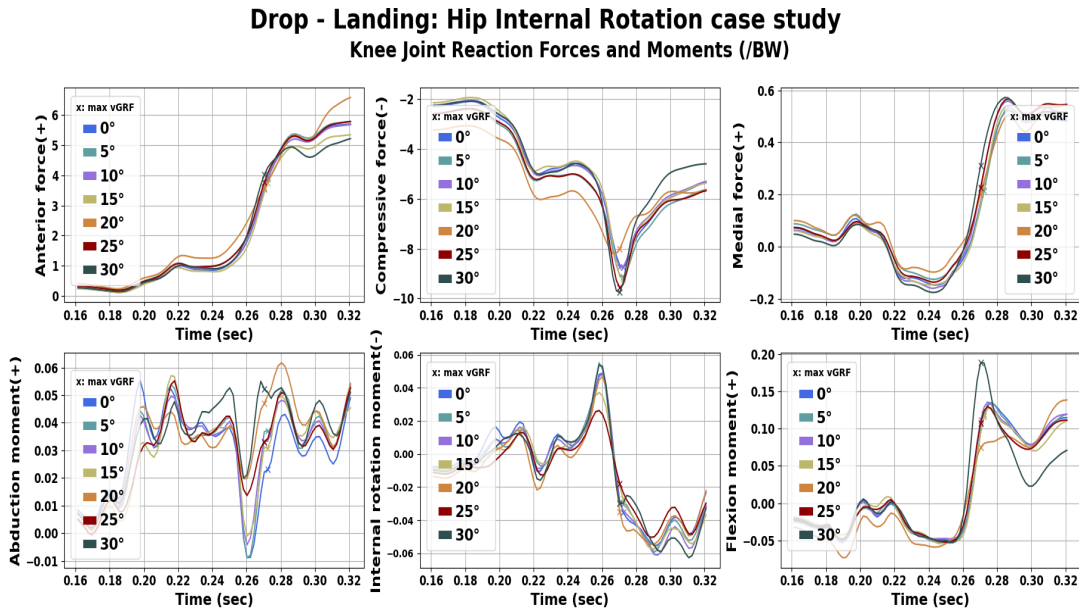


FIGURE 4.7: Knee joint JRF and JRM for various hip internal rotation angles.

Next, in Figure 4.8 we demonstrate muscle forces and muscle force ratios for the various hip internal rotation angles. We can detect greater hamstrings force for the 20° hip internal rotation. Correspondingly, Q/H force ratio obtain lower value for that scenario at max vGRF. However, for the other scenarios we can not derive a clear description pattern.

Drop - Landing: Hip Internal Rotation case study Muscle forces and Muscle Force Ratios

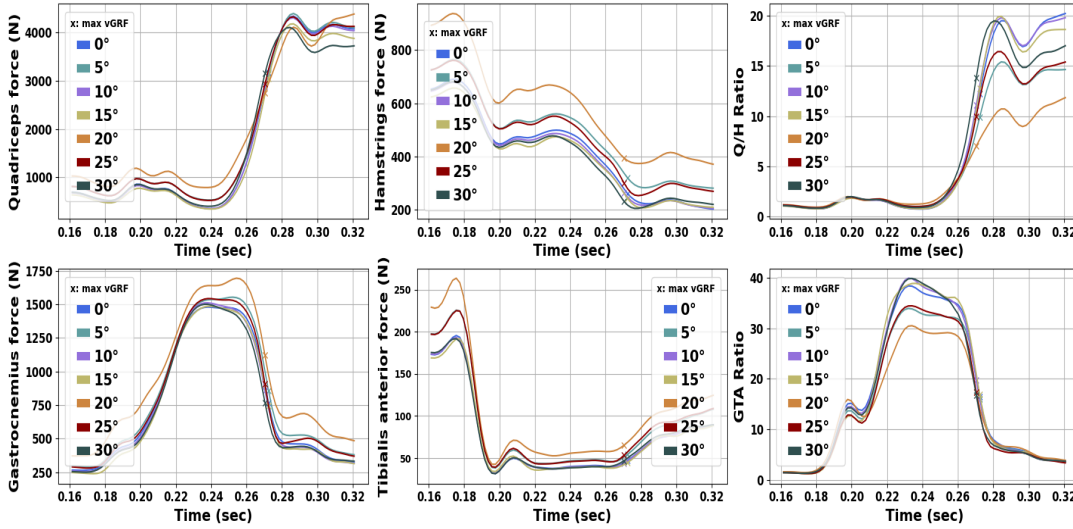


FIGURE 4.8: Muscle forces and muscle force ratios for various hip internal rotation angles.

Finally, in Table 4.3 and Table 4.4, values for all examined parameters at maximum vGRF for all cases are presented. We can state that the greatest vGRF value is detected for the 30° hip internal rotation scenario, while the lowest one is observed for the 20° scenario. If we exclude the 20° scenario we can claim that as the hip rotation is increased, the peak vGRF is also increased.

Case	pGRF	vGRF	mGRF	Q/H_ratio	GTA_ratio
0	0.522	3.602	-0.088	12.264	15.933
5	0.521	3.722	-0.055	9.911	15.583
10	0.607	3.795	0.000	11.007	20.074
15	0.671	4.310	0.102	12.775	16.568
20	0.233	2.234	0.108	7.016	17.291
25	0.732	4.417	0.226	9.860	17.736
30	0.605	4.658	0.340	13.880	16.145

TABLE 4.3: GRF, Q/H force ratio and GTA force ratio at the time instant of peak vGRF for various hip internal rotation angles.

Also, in Table 4.4 we can observe that all kJRF obtains the greatest value for the 30° case at maximum vGRF. Also, AbdM for no internal rotation is lower compared to the other cases, while IRM is lower for 25° of hip internal rotation at the same time instant. Regarding the 20° hip internal rotation with the lowest peak vGRF, we can detect the greatest AbdM and IRM values at peak vGRF compared with the other scenarios.

Case	AF(+)	CF(-)	MF(+)	AbdM(+)	IRM(-)	FM(+)
0	3.927	-8.921	0.231	0.020	-0.034	0.120
5	3.982	-9.333	0.207	0.031	-0.022	0.125
10	3.578	-9.037	0.208	0.021	-0.030	0.120
15	3.787	-9.508	0.231	0.028	-0.027	0.120
20	3.605	-8.089	0.201	0.044	-0.043	0.080
25	3.809	-10.050	0.213	0.027	-0.019	0.116
30	4.068	-10.133	0.310	0.052	-0.028	0.217

TABLE 4.4: Knee joint JRF and JRM at the time instant of peak vGRF for various hip internal rotation angles.

Next, we exhibit results regarding cases with different hip external rotation angles. As mentioned before, the angles examined were 0° , 5° , 15° , 20° , 25° and 30° hip external rotation.

First, in Figure 4.9 we provide the hip, knee and ankle flexion angles for the examined scenarios. Also angles for hip adduction and external rotation are plotted. Again, hip adduction bounds are more relaxed and we can see that at max vGRF for lower hip external rotation values (0° , 5° , 10° and 15°), the hip is more adducted, while for the 20° , 25° and 30° cases hip is less adducted.

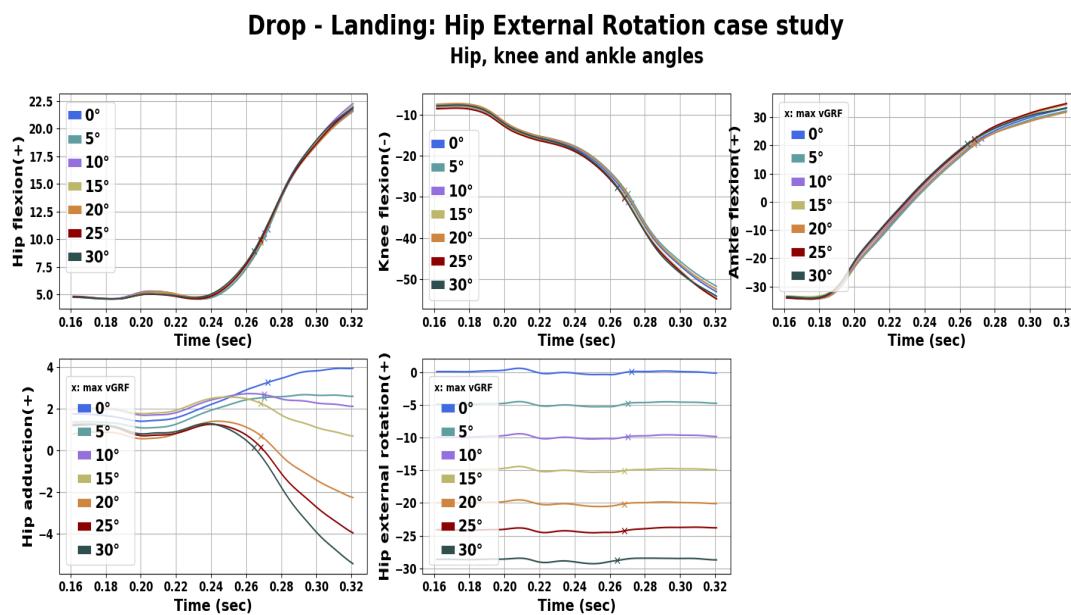


FIGURE 4.9: Hip, knee and ankle kinematics for various hip external rotation angles.

Next, in Figure 4.10 we demonstrate GRF and GRM for scenarios with different hip external rotation angles. In ascending order of vGRF peak value the examined cases are: 15° , 10° , 25° , 0° , 20° , 5° and 30° respectively. We notice that the minimum peak vGRF values are for 15° and 10° hip external rotation.

Drop - Landing: Hip External Rotation case study
Ground Reaction Forces and Moments (/BW)

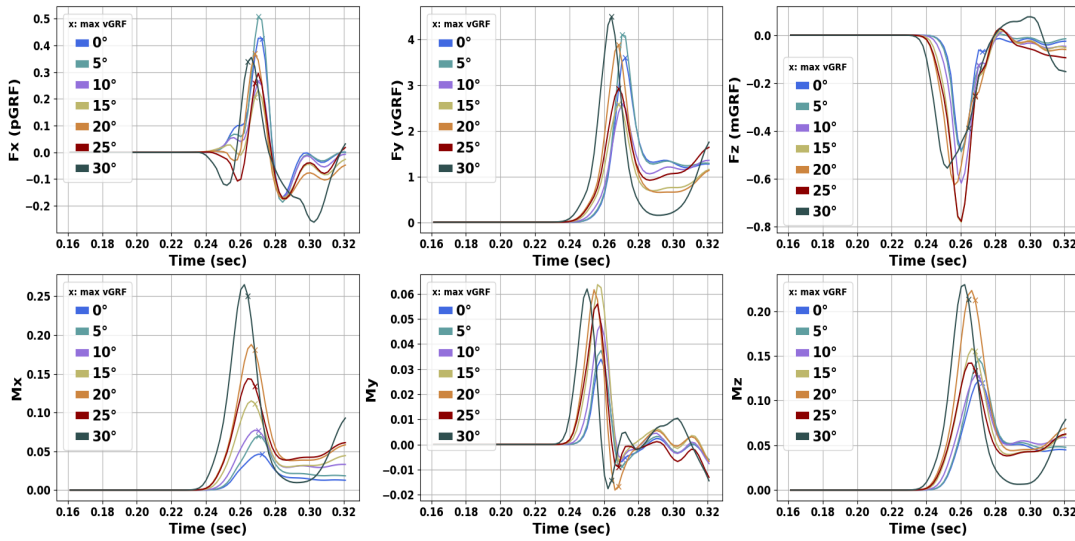


FIGURE 4.10: GRF and GRM for various hip external rotation angles.

Moreover, in Figure 4.11 we demonstrate kJRF and kJRM for different cases with externally rotated hip. No great differences are observed in moments and forces at the knee joint among the studied scenarios with a few exceptions. For example, CF is higher for the 30° cases close to maximum vGRF time. Moreover, in the majority of the landing phase an ERM is introduced.

Drop - Landing: Hip External Rotation case study
Knee Joint Reaction Forces and Moments (/BW)

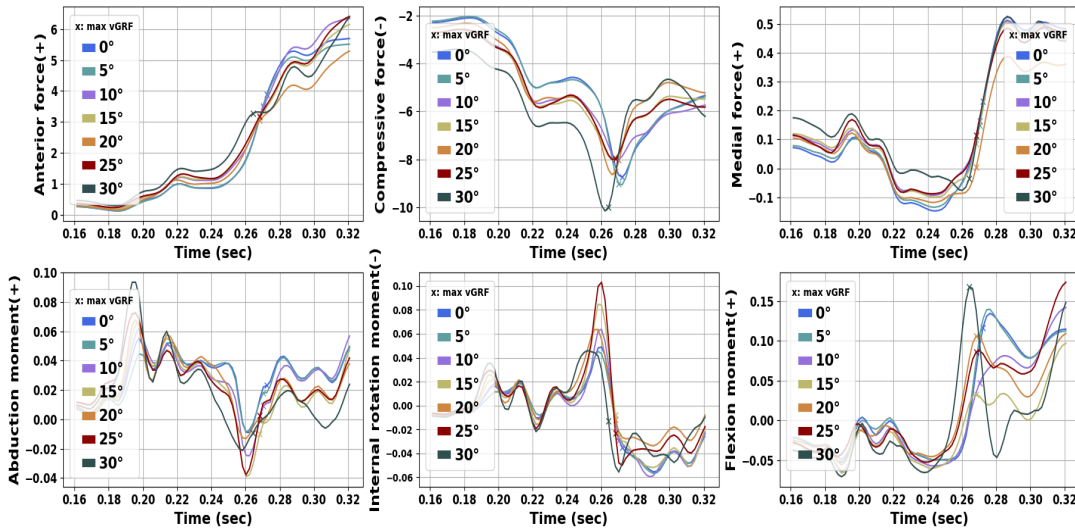


FIGURE 4.11: kJRF and kJRM for various hip external rotation angles.

Following, we demonstrate muscle forces and muscle force ratios for the examined cases in Figure 4.12. It is obvious that for 30° hip external rotation the hamstrings, gastrocnemius and tibialis anterior forces are greater compared with the remaining scenarios at max vGRF. That results in lower Q/H force ratio and GTA force ratio values at the same time instant.

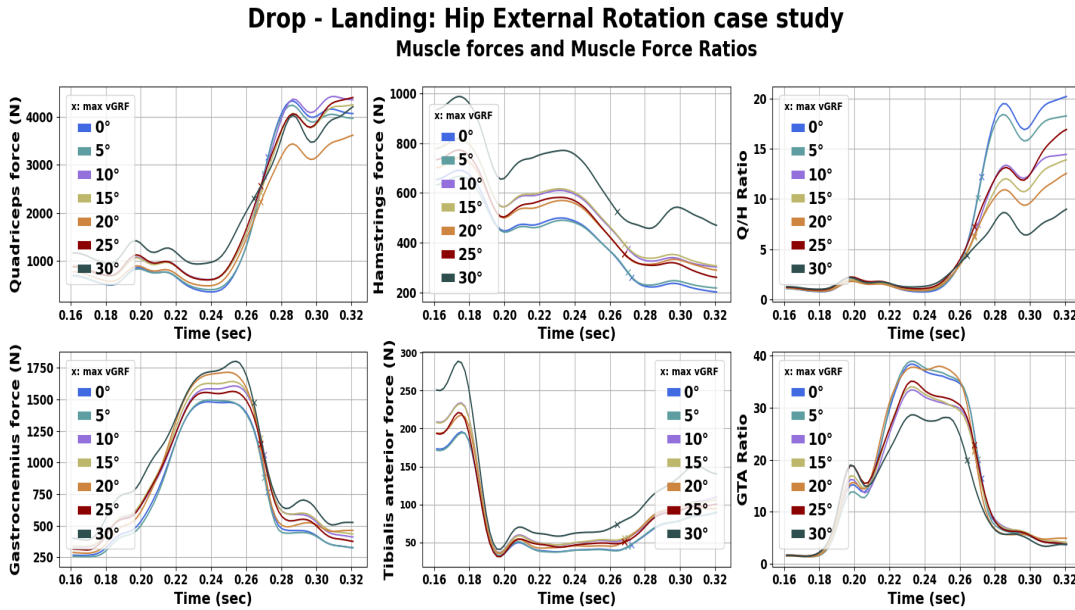


FIGURE 4.12: Muscle forces and muscle force ratios for various hip external rotation angles.

Also, in Table 4.5 and Table 4.6, values of parameters at maximum vGRF for all cases are presented. We can notice that as the hip external rotation angle is increased, the Q/H force ratio is decreased. Also, the lowest peaks of vGRF are detected for 10° and 15° hip external rotation following by the case with no hip rotation.

Case	pGRF	vGRF	mGRF	Q/H_ratio	GTA_ratio
0	0.522	3.602	-0.088	12.264	15.933
5	0.618	4.108	-0.221	10.065	20.442
10	0.309	2.593	-0.180	7.399	19.044
15	0.241	2.584	-0.212	6.141	21.490
20	0.434	3.888	-0.299	6.307	21.426
25	0.320	2.924	-0.209	7.250	22.630
30	0.386	4.501	-0.418	4.382	19.546

TABLE 4.5: GRF, Q/H force ratio and GTA force ratio at the time instant of peak vGRF for various hip external rotation angles.

Regarding AF, the lowest value is spotted for the scenario with 20° hip external rotation, following by 15° while the highest value is detected for the case with no hip rotation. The highest value for AddM is detected for the 30° case at max vGRF while the highest value for the IRM is spotted for the scenario with no rotation.

Case	AF(+)	CF(-)	MF(+)	AbdM(+)	IRM(-)	FM(+)
0	3.927	-8.921	0.231	0.020	-0.034	0.120
5	3.554	-9.356	0.129	0.005	-0.024	0.114
10	3.486	-8.123	0.158	0.002	-0.027	0.050
15	3.167	-8.051	0.088	-0.003	-0.012	0.035
20	3.069	-8.694	-0.005	-0.002	-0.010	0.108
25	3.203	-8.071	0.119	0.010	-0.033	0.088
30	3.298	-10.178	-0.046	-0.008	-0.009	0.171

TABLE 4.6: Knee joint JRF and JRM at the time instant of peak vGRF for various hip external rotation angles.

4.3 Trunk orientation case

In this section we demonstrate results regarding single - leg landings corresponding to different trunk orientations. First, we will present simulation results regarding trunk leaning forward and backward. This corresponds to lumbar flexion and extension respectively. Then, we will continue with results concerning trunk right and left bending (lumbar bending). Finally, we will demonstrate simulation results for landings with the trunk internally and externally rotated (lumbar internal and external rotation respectively).

4.3.1 Trunk forward - backward leaning

Starting from different lumbar flexion - extension angles, we examine the upright position (without any flexion, bending or rotation angle), landings with lumbar flexion (0° , 5° , 10° , 15° , 20° , 25° and 30°) and landings with lumbar extension (0° , 5° , 10° , 15° and 20°).

In Figure 4.13 we display hip, knee and ankle joint angles for the scenarios with lumbar flexion. We can notice that for the upright case knee flexion is greater and ankle flexion is lower compared with the remaining cases. Also, the cases with 15° and 20° trunk flexion presents the lowest knee flexion for the entire motion.

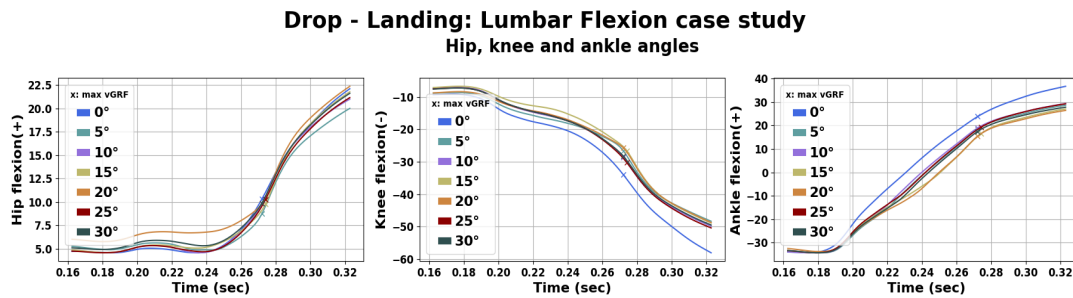


FIGURE 4.13: Hip, knee and ankle kinematics for multiple lumbar flexion angles.

Next, in Figure 4.14 we demonstrate GRF and GRM for cases with multiple trunk flexion angles. We can mark that the lower vGRF peak is spotted for the upright position of the upper body following by the case with 25° trunk flexion and then the cases with 30°, 10°, 5°, 15° and 20° in ascending order. Almost the same pattern is detected for the pGRF at maximum vGRF.

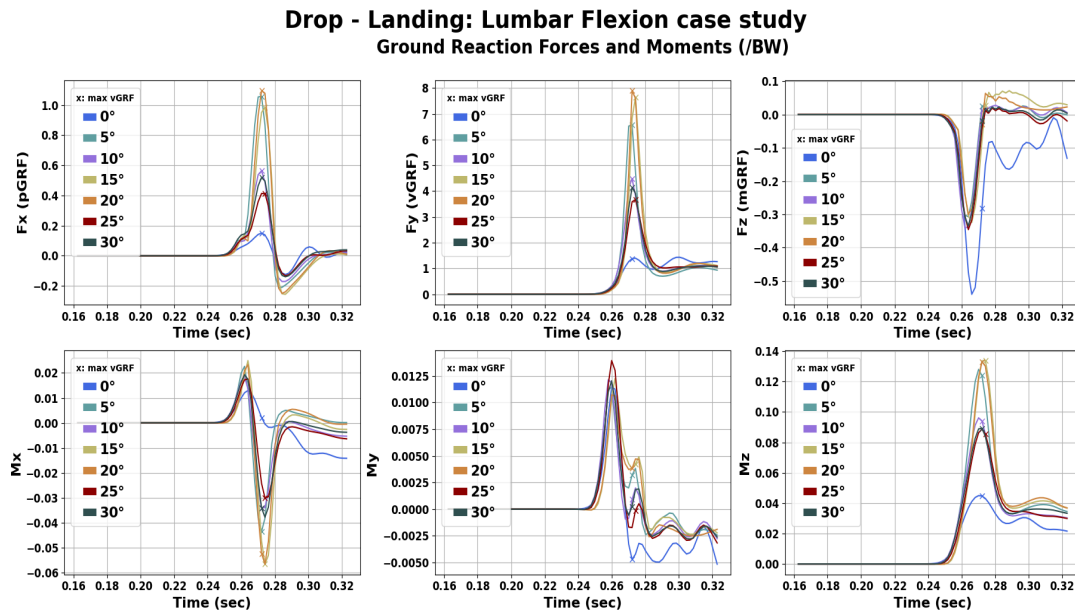


FIGURE 4.14: GRF and GRM for multiple lumbar flexion angles.

Subsequently, in Figure 4.15 we demonstrate kJRF and kJRM for the respective scenarios. It is noticeable that before and after peak vGRF, AF is greater for the upright position. For CF, the upright position shows a different behavior compared with the remaining cases with greater values except of the time around peak vGRF where it takes the lowest value. Again, we notice a deviation in the behavior of AbdM and ERM for the upright case. Comparisons between the cases cannot be easily made.

Drop - Landing: Lumbar Flexion case study Knee Joint Reaction Forces and Moments (/BW)

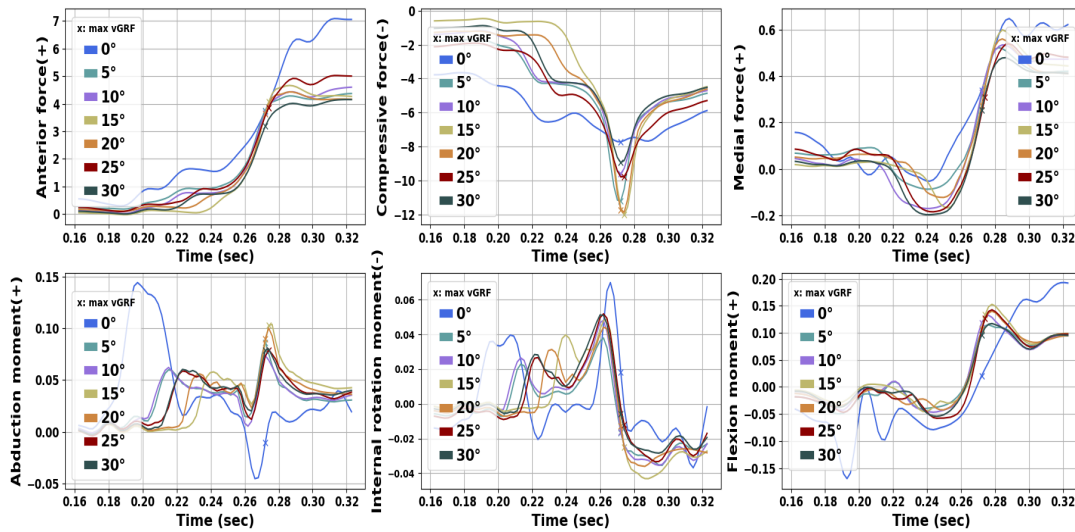


FIGURE 4.15: Knee joint JRF and JRM for multiple lumbar flexion angles.

In Figure 4.16 we demonstrate muscle forces and muscle force ratios for scenarios with multiple trunk flexion - extension angles. We can see that for the upright position quadriceps, hamstrings, gastrocnemius and tibialis anterior forces obtain higher values compared with other cases with trunk flexion. As a result, at maximum vGRF both Q/H force ratio and GTA force ratio obtain lower values for the upright case. The greatest ratios are observed for the case with 15° trunk flexion.

Drop - Landing: Lumbar Flexion case study Muscle forces and Muscle Force Ratios

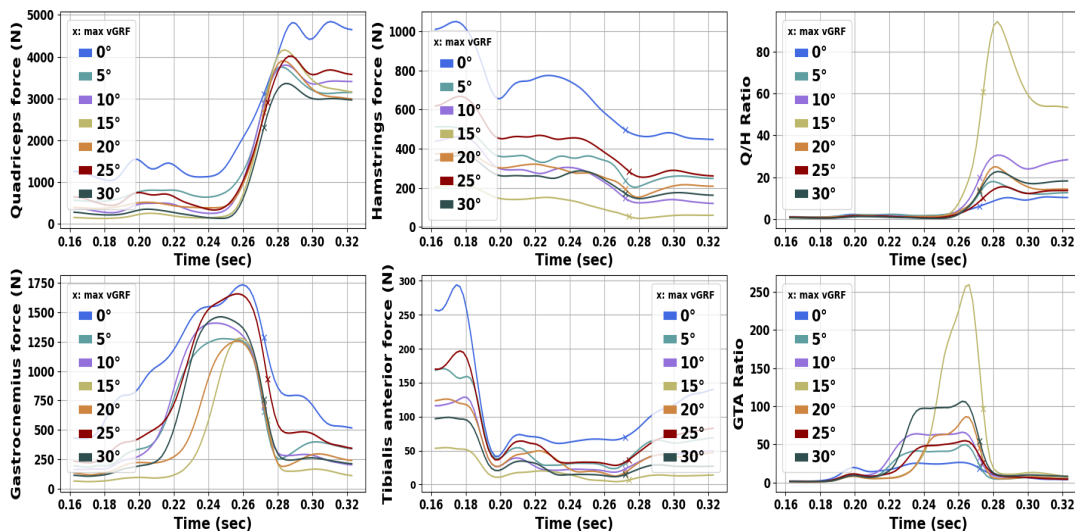


FIGURE 4.16: Muscle forces and muscle force ratios for multiple lumbar flexion angle s.

Moreover, in Table 4.7 and Table 4.8, values for parameters at the peak vGRF for all cases are presented. If we take a closer look at vGRF we can

notice that the lowest vGRF and Q/H force ratio values are detected for 0°, and then 25° trunk flexion.

Case	pGRF	vGRF	mGRF	Q/H_ratio	GTA_ratio
0	0.167	1.383	-0.176	6.275	18.351
5	1.380	6.571	0.016	12.713	20.565
10	0.725	4.485	-0.019	19.775	30.855
15	1.412	7.647	0.055	59.534	81.153
20	1.645	7.892	0.095	13.545	42.070
25	0.505	3.674	-0.038	10.211	25.128
30	0.673	4.139	0.022	13.440	52.721

TABLE 4.7: GRF, Q/H force ratio and GTA force ratio at the time instant of peak vGRF for multiple lumbar flexion angles.

Also, in Table 4.8 we notice that for the upright case AbdM is lower at max vGRF compared with the remaining scenarios. Nonetheless, CF obtains lower value for the upright case, while AF obtains the lowest value for the 30° case following by 10°, 0° and 5° scenarios respectively.

Case	AF(+)	CF(-)	MF(+)	AbdM(+)	IRM(-)	FM(+)
0	3.756	-7.761	0.334	0.006	0.000	0.023
5	3.862	-12.160	0.290	0.094	-0.021	0.114
10	3.731	-10.090	0.323	0.077	-0.014	0.126
15	4.245	-13.329	0.373	0.105	-0.032	0.140
20	3.829	-13.372	0.268	0.132	-0.023	0.107
25	3.899	-10.024	0.308	0.072	-0.013	0.129
30	3.241	-9.421	0.256	0.093	-0.008	0.101

TABLE 4.8: Knee joint JRF and JRM at the time instant of peak vGRF for multiple lumbar flexion angles.

Next, we present the resulted plots for the scenarios of single - leg landings with the trunk in extension. First, in Figure 4.17 hip, knee and ankle flexion angles are displayed for multiple trunk extension angles. We observe that small deviations between the different cases exist for all three joint angles.

Drop - Landing: Lumbar Extension case study Hip, knee and ankle angles

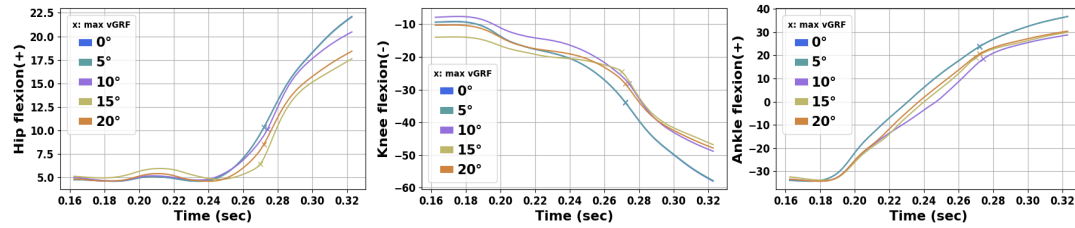


FIGURE 4.17: Hip, knee and ankle kinematics for multiple lumbar extension angles.

Afterwards, in Figure 4.18 we demonstrate GRF and GRM for cases with different trunk extension angles. The lowest vGRF peaks are observed for the cases with 0° and 5° following by 20°, 10° and 15° trunk extension. The same order is noticed for pGRF at peak vGRF.

Drop - Landing: Lumbar Extension case study Ground Reaction Forces and Moments (/BW)

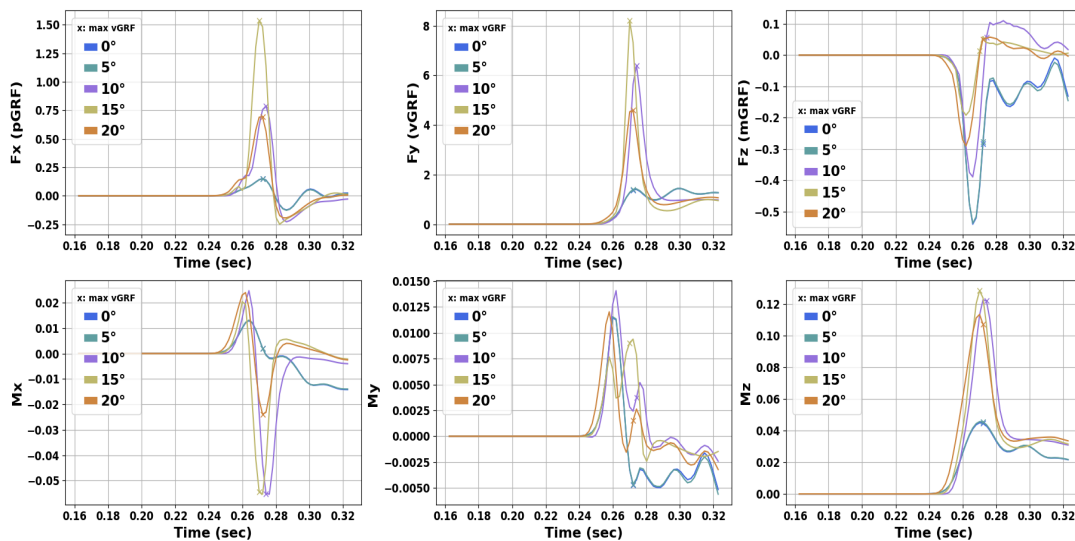


FIGURE 4.18: GRF and GRM for multiple lumbar extension angles.

Following, in Figure 4.19 we demonstrate kJRF and kJRM for the examined scenarios. AF after max vGRF time instant obtains greater peaks for the cases of lower trunk extension values. Though, CF obtains lower peaks for cases of 0° and 5°, while the highest peak is for the case of 10° of trunk extension.

Regarding AbdM and AddM on the knee joint we can detect different behavior for the different cases. Around IGC, drop - landings with 0° and 5° of trunk extension presents higher AbdM values. For IRM and ERM things are more compatible between the scenarios. A first ERM peak is observed at IGC following by a greater one before max vGRF. of trunk extension.

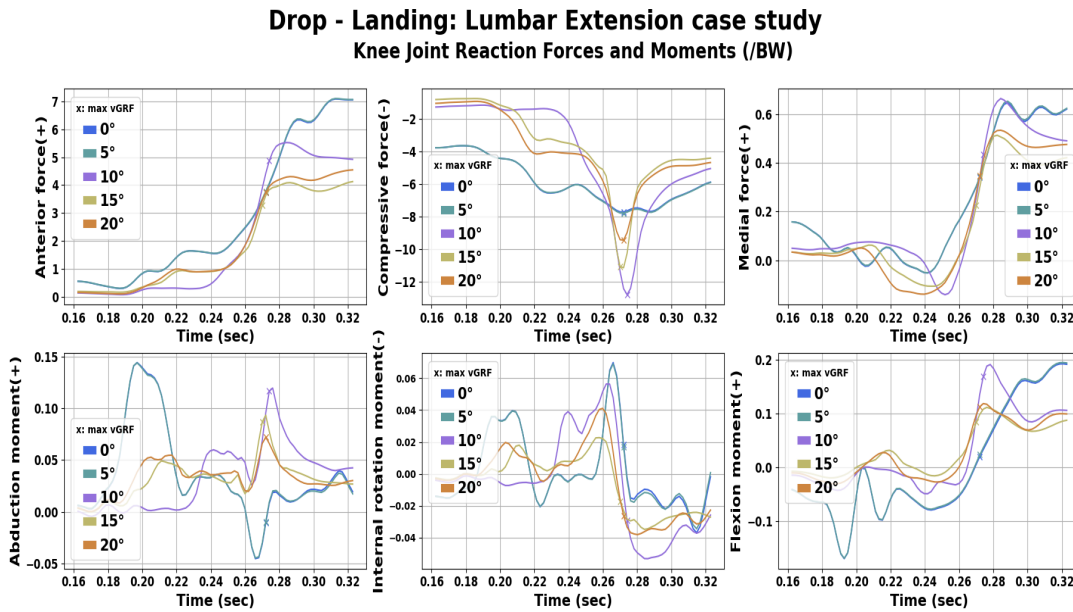


FIGURE 4.19: Knee joint JRF and JRM for multiple lumbar extension angles.

In Figure 4.20 we demonstrate muscle forces and muscle force ratios. Hamstrings, gastrocnemius and tibialis anterior forces are greater for 0 and 5 degrees of trunk extension following by the rest of the scenarios. As a result, Q/H force ratio is lower for the previous cases.

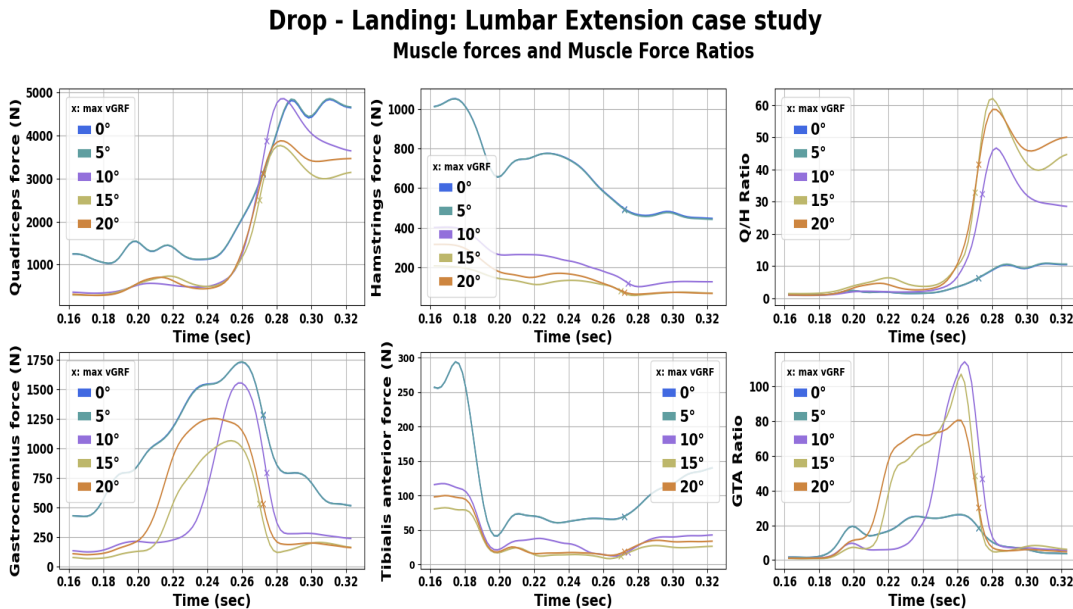


FIGURE 4.20: Muscle forces and muscle force ratios for multiple lumbar extension angles.

In Table 4.9 and Table 4.10, values for parameters at the maximum vGRF for all cases are presented. We can verify the observation made previously regarding vGRF and pGRF, highest values for an extended trunk.

Case	pGRF	vGRF	mGRF	Q/H_ratio	GTA_ratio
0	0.167	1.383	-0.176	6.275	18.351
5	0.165	1.401	-0.171	6.391	18.483
10	1.083	6.403	0.074	32.214	42.112
15	2.211	8.198	0.006	30.940	40.500
20	0.857	4.593	0.031	41.636	28.596

TABLE 4.9: GRF, Q/H force ratio and GTA force ratio at the time instant of peak vGRF for multiple lumbar extension angles.

In Table 4.10 we can investigate in details the deviations between the cases at maximum vGRF time. AF takes the lower value for the case with 15° trunk extension and the greater one for 10° trunk extension. Moreover, CF is lower for the scenario with no extension and higher for the case with 10° trunk extension. Concerning AbdM, the greatest value is observed for 10° trunk extension and the lowest for the cases of 0° and 5° lumbar extension.

Case	AF(+)	CF(-)	MF(+)	AbdM(+)	IRM(-)	FM(+)
0	3.756	-7.761	0.334	0.006	0.000	0.023
5	3.793	-7.835	0.338	0.007	-0.001	0.026
10	4.988	-13.681	0.454	0.118	-0.036	0.176
15	3.507	-12.850	0.254	0.082	-0.029	0.091
20	3.800	-9.908	0.338	0.074	-0.028	0.122

TABLE 4.10: Knee joint JRF and JRM at the time instant of peak vGRF for multiple trunk extension angles.

4.3.2 Trunk medial - lateral bending

In this section we demonstrate results for cases where the model lands with different trunk bending angles as described in subsection 3.3.4. First, we present results about the scenarios of trunk right bending studies. Then, resulted plots about scenarios with left trunk bending are displayed. The investigated angles were 0°, 5°, 10°, 15°, 20°, 25° and 30° for both right and left bending. Initially, in Figure 4.21 we display angles for the hip, knee and ankle joints for scenarios of trunk right bending.

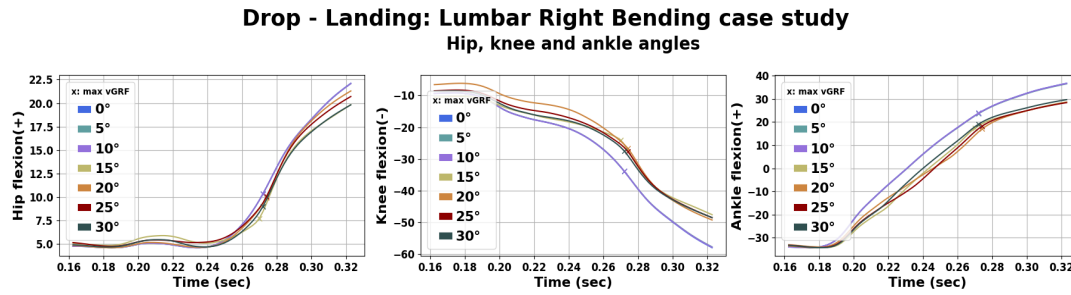


FIGURE 4.21: Hip, knee and ankle kinematics for multiple trunk right bending angles.

In Figure 4.22 we demonstrate GRF and GRM for the respective cases. pGRF and vGRF peak values are lower for the cases with 0°, 5° and 10° right bending while much greater peak values are observed for 15°, 20°, 25° and 30° trunk right bending.

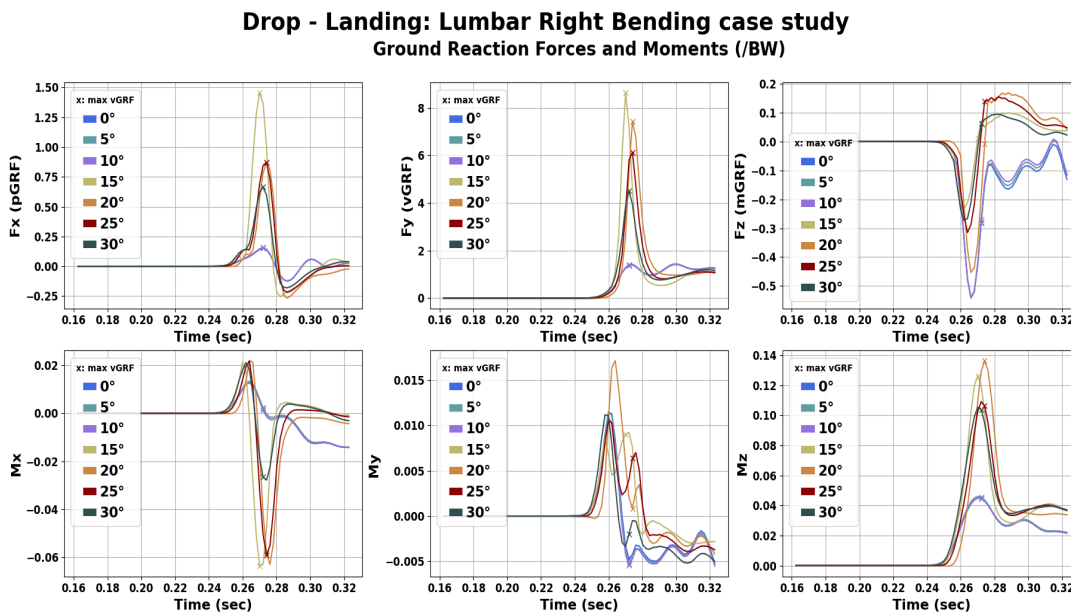


FIGURE 4.22: GRF and GRM for multiple trunk right bending angles.

In Figure 4.23 we demonstrate kJRF and kJRM for the studied scenarios. AF raise a peak value right after max vGRF time. On the contrary, CF displays lower peak values for the scenarios with lower vGRF peaks at max vGRF time. Results for AbdM, AddM and IRM, ERM are more complicated. The main observation is for the different behavior of the AbdM at IGC time, where for increased right bending (towards the medial aspect) the AbdM rapidly increases.

Drop - Landing: Lumbar Right Bending case study Knee Joint Reaction Forces and Moments (/BW)

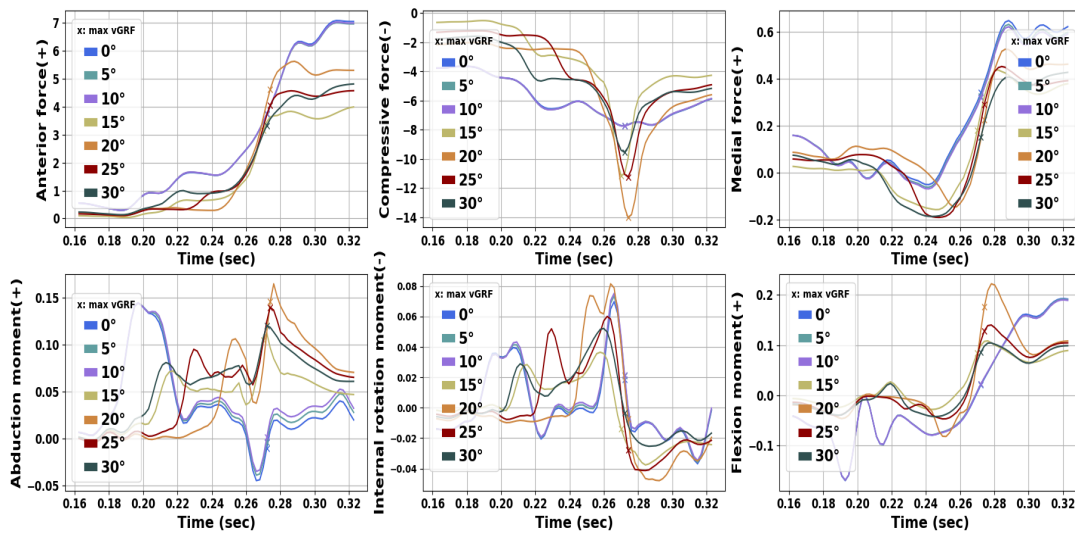


FIGURE 4.23: Knee joint JRF and JRM for multiple trunk right bending angles.

Subsequently, in Figure 4.24 we demonstrate muscle forces and muscle force ratios for the examined cases. We can note that hamstrings force is lower for the scenario with 15° trunk right bending followed by 25°, 30° and 20°, with the greatest hamstring forces for the cases of 0°, 5° and 10°. Correspondingly, Q/H force ratio is lower for the cases of 0°, 5° and 10° and further increases as the bending angle increases.

Drop - Landing: Lumbar Right Bending case study Muscle forces and Muscle Force Ratios

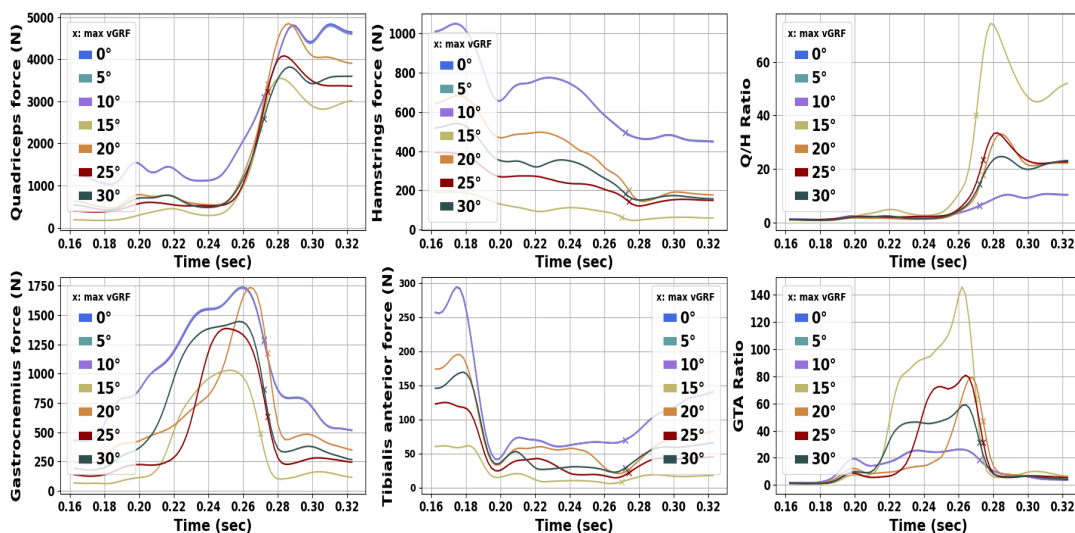


FIGURE 4.24: Muscle forces and muscle force ratios for multiple trunk right bending angles.

In Table 4.11 and Table 4.12, values for parameters at the maximum vGRF time for all cases are presented. The lowest values for vGRF and Q/H force

ratio are detected for 0° , 5° and 10° of right trunk bending, while the highest values are detected for the case of 15° .

Case	pGRF	vGRF	mGRF	Q/H_ratio	GTA_ratio
0	0.167	1.383	-0.176	6.275	18.351
5	0.167	1.387	-0.173	6.232	18.470
10	0.173	1.413	-0.162	6.322	18.312
15	2.126	8.632	0.033	37.554	50.881
20	1.248	7.432	0.080	17.024	43.116
25	1.174	6.131	0.074	23.210	27.825
30	0.866	4.515	0.056	14.284	30.678

TABLE 4.11: GRF, Q/H force ratio and GTA force ratio at the time instant of peak vGRF for multiple trunk right bending angles.

Based on Table 4.12, we can spot that at peak vGRF time, AF is greater for the case of 20° and 25° right bending scenarios. Also, AbdM is lower for the the case with 0° trunk right bending.

Case	AF(+)	CF(-)	MF(+)	AbdM(+)	IRM(-)	FM(+)
0	3.756	-7.761	0.334	0.006	0.000	0.023
5	3.729	-7.769	0.318	0.012	0.002	0.025
10	3.754	-7.784	0.313	0.018	0.003	0.025
15	3.397	-13.052	0.218	0.101	-0.026	0.093
20	4.794	-15.326	0.261	0.153	-0.021	0.185
25	4.176	-12.075	0.295	0.131	-0.032	0.134
30	3.396	-10.125	0.144	0.127	-0.004	0.092

TABLE 4.12: Knee joint JRF and JRM at the time instant of peak vGRF for multiple trunk right bending angles.

Next, we exhibit the resulted plots regarding the cases of single - leg landings with left bending angles. When landing with the left leg, left bending corresponds to a bending towards the lateral left side. In Figure 4.25 we display angles for the hip, knee and ankle joints.

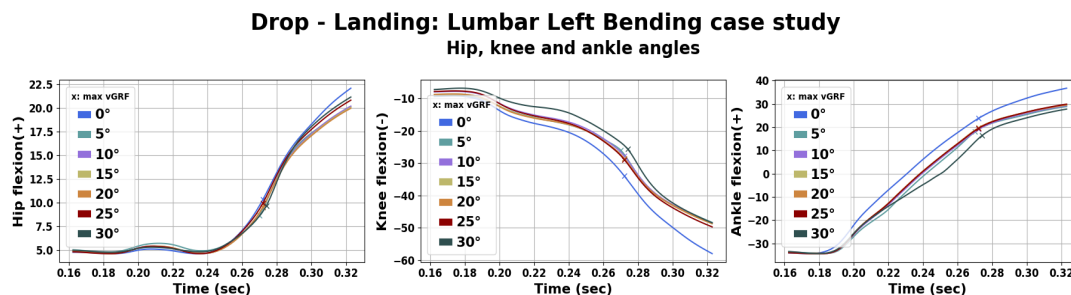


FIGURE 4.25: Hip, knee and ankle kinematics for multiple trunk left bending angles.

Next, in Figure 4.26 we demonstrate GRF and GRM for the already mentioned cases. We notice that pGRF and vGRF peak values obtain the lower value for no right bending while much greater peak values are observed for the remaining examined scenarios. The highest value is spotted for the case with 30° trunk right bending.

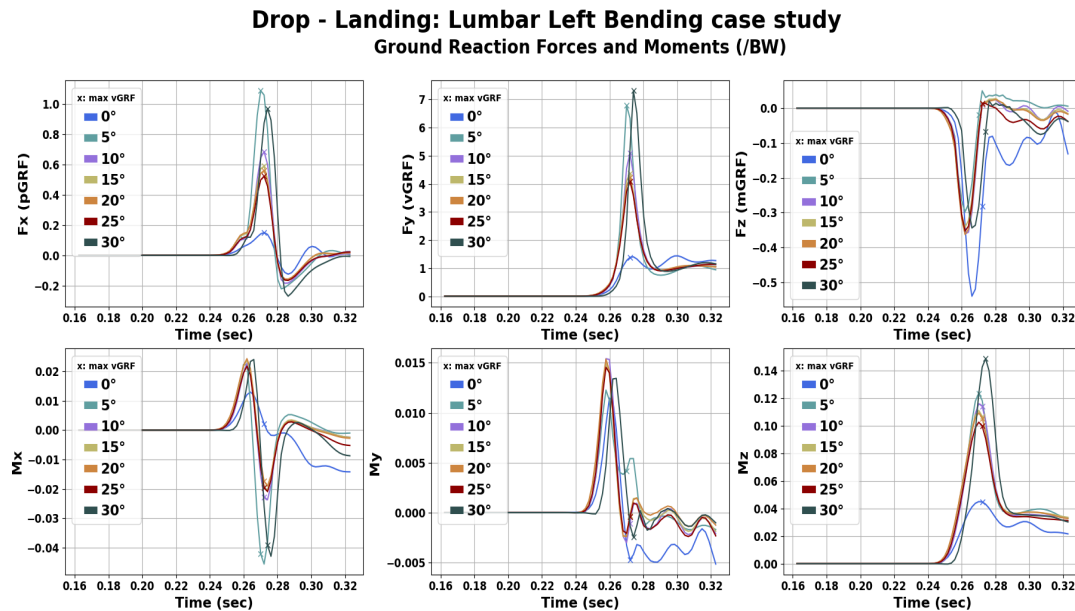


FIGURE 4.26: GRF and GRM for multiple trunk left bending angles.

Also, in Figure 4.27 we demonstrate kJRF and kJRM for the studied scenarios. AF reaches a peak value right after max vGRF time with greater value for the case with no bending, following by the scenario with 30°. Regarding CF, a peak value is noticed at max vGRF time instant. Furthermore, the greatest peak is observed for the case with 30° of trunk left bending, while the lowest one for the case with no bending. Concerning AbdM and IRM we can detect a deviation on behavior between the case with no trunk bending and the cases with left trunk bending.

Drop - Landing: Lumbar Left Bending case study
Knee Joint Reaction Forces and Moments (/BW)

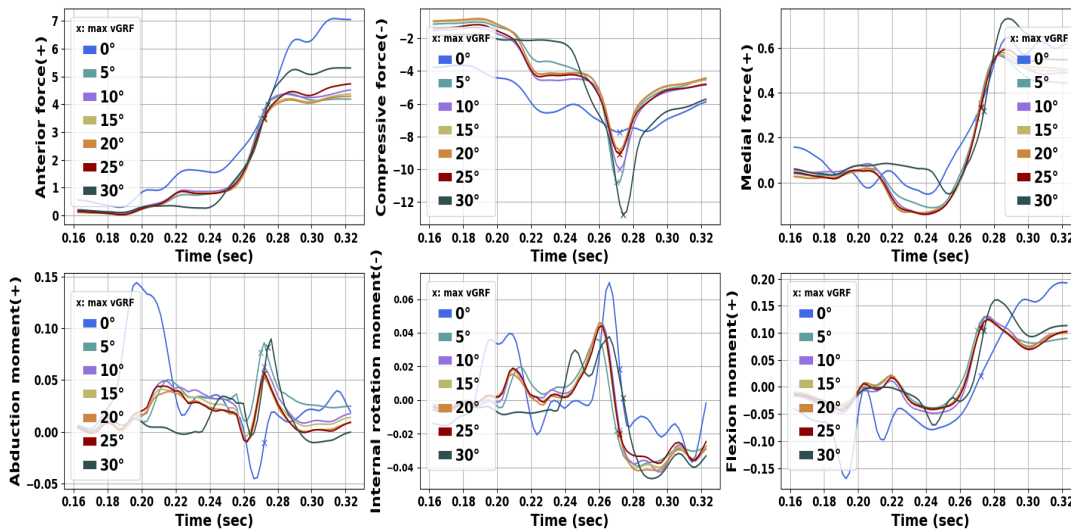


FIGURE 4.27: Knee joint JRF and JRM for multiple trunk left bending angles.

Following, in Figure 4.28 we demonstrate muscle forces and muscle force ratios for the examined scenarios. It is obvious that Q/H force ratio is lower for the cases with 0° and 25° left trunk bending. The greatest values are detected for the case with 30° trunk left bending.

Drop - Landing: Lumbar Left Bending case study
Muscle forces and Muscle Force Ratios

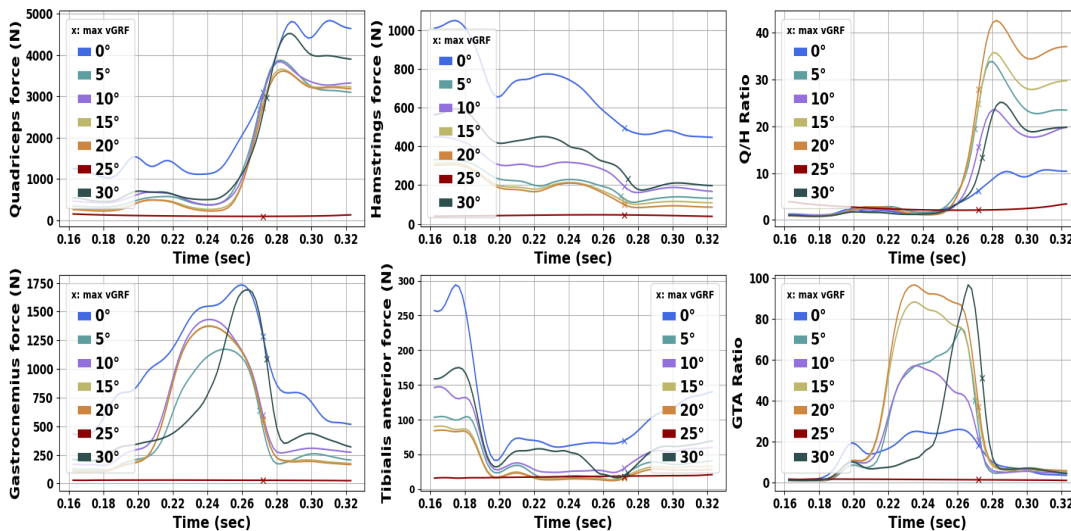


FIGURE 4.28: Muscle forces and muscle force ratios for multiple trunk left bending angles.

Finally, in Table 4.13 and Table 4.14, values for parameters at the time instant of maximum vGRF for all cases are presented. CF at peak vGRF is lower for the cases with lower vGRF peaks.

Case	pGRF	vGRF	mGRF	Q/H_ratio	GTA_ratio
0	0.167	1.383	-0.176	6.275	18.351
5	1.529	6.787	0.016	18.631	36.024
10	0.897	5.091	-0.020	15.568	20.236
15	0.748	4.378	-0.018	24.773	30.945
20	0.712	4.224	-0.021	27.775	35.635
25	0.665	4.088	-0.013	2.095	1.496
30	1.377	7.309	-0.011	12.901	46.030

TABLE 4.13: GRF, Q/H force ratio and GTA force ratio at the time instant of peak vGRF for multiple trunk left bending angles.

Case	AF(+)	CF(-)	MF(+)	AbdM(+)	IRM(-)	FM(+)
0	3.756	-7.761	0.334	0.006	0.000	0.023
5	3.645	-11.960	0.315	0.078	-0.028	0.109
10	3.810	-10.618	0.333	0.067	-0.017	0.123
15	3.594	-9.494	0.341	0.058	-0.022	0.117
20	3.512	-9.259	0.343	0.055	-0.020	0.116
25	3.552	-9.446	0.325	0.056	-0.021	0.115
30	4.135	-14.095	0.342	0.085	-0.008	0.111

TABLE 4.14: Knee joint JRF and JRM at the time instant of peak vGRF for multiple trunk left bending angles.

4.3.3 Trunk internal - external rotation

In this part, we demonstrate results regarding drop landings with different trunk rotation angles as described in subsection 3.3.4. In Figure 4.29 we display angles of the hip, knee and ankle joints corresponding to internal rotation angles.

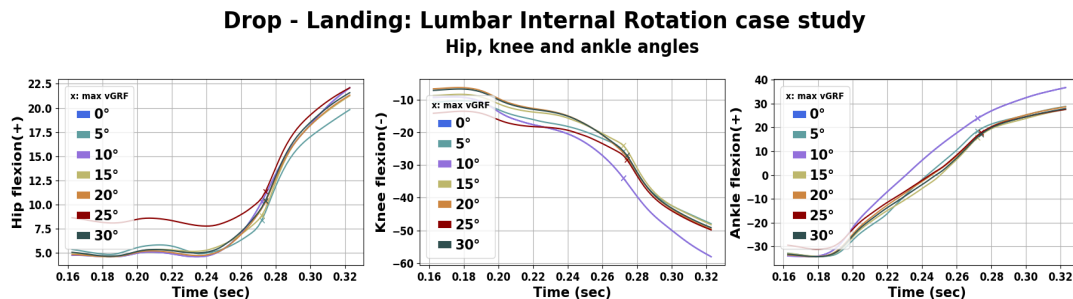


FIGURE 4.29: Hip, knee and ankle kinematics for multiple trunk internal rotation angles.

In Figure 4.30 we demonstrate GRF and GRM for the previously mentioned scenarios. Minimum peak vGRF values are detected for the cases with 0° and

10° internal rotation, while maximum peak values are spotted for the 15° and 25° cases. The same observation is valid for the pGRF.

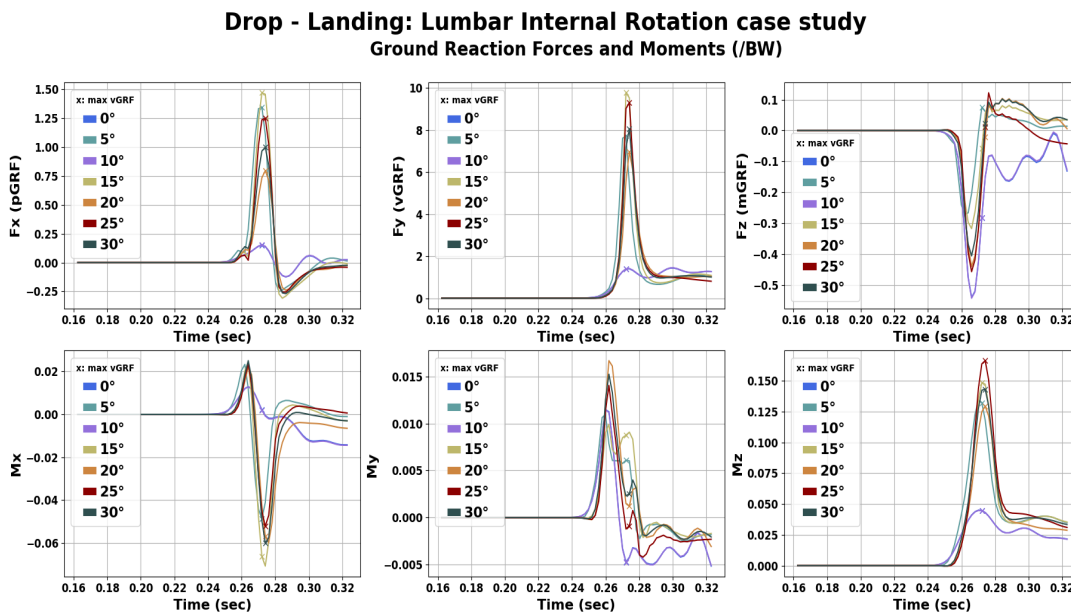


FIGURE 4.30: GRF and GRM for multiple trunk internal rotation angles.

In addition, in Figure 4.31 we demonstrate kJRF and kJRM for the described cases. CF displays lower values for the cases with 0° and 10° of trunk internal rotations and increases for the cases with 5°, 15°, 20°, 30°, getting the highest peak for 25° at max vGRF time instant.

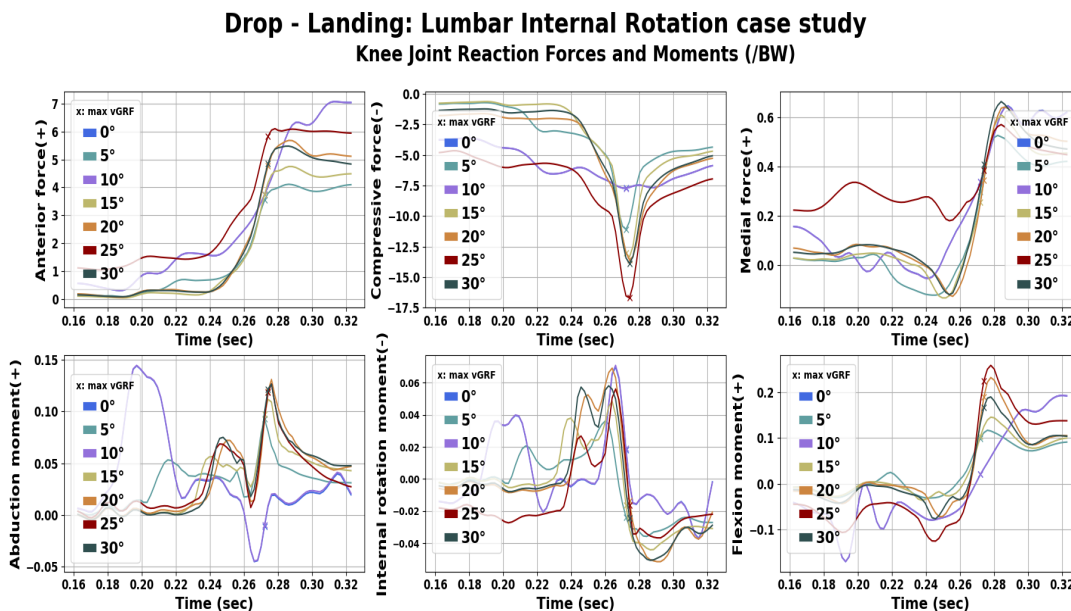


FIGURE 4.31: Knee joint JRF and JRM for multiple trunk internal rotation angles.

In Figure 4.32 we demonstrate muscle forces and muscle force ratios. In general, we can observe that maximum muscle forces are detected for the case

of 25° of trunk internal rotation and the minimum muscle forces are detected for the cases of 15°, 5° and 30°.

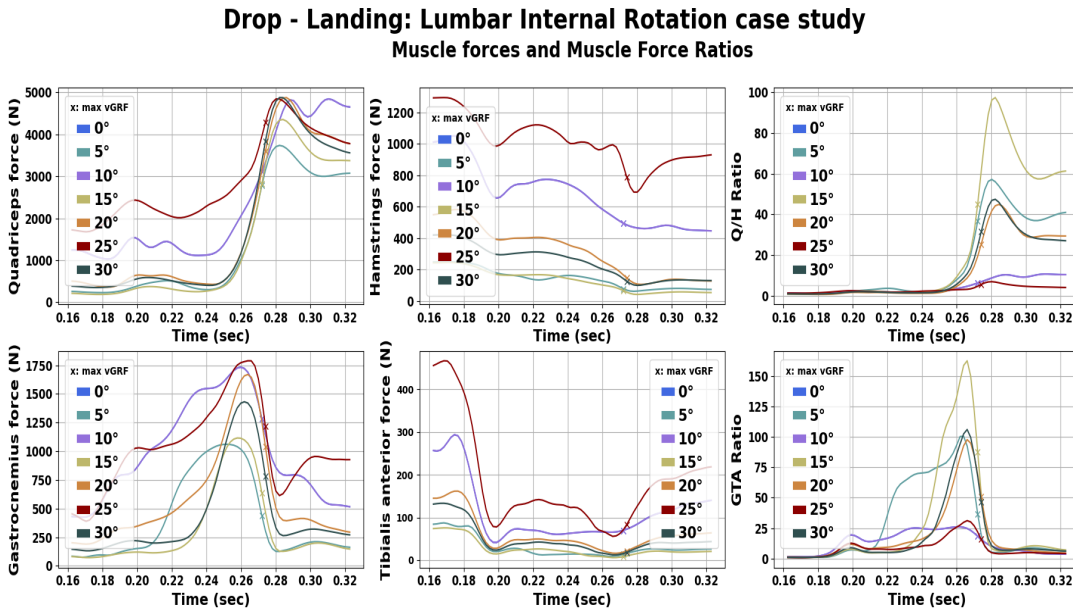


FIGURE 4.32: Muscle forces and muscle force ratios for multiple trunk internal rotation angles.

Also, in Table 4.15 and Table 4.16, values of parameters at the maximum vGRF time instant for all cases are presented. As mentioned previously, lower vGRF and pGRF peaks are spotted for the 0° and 10° trunk internal rotation cases, while maximum values are detected for the 15° and 25° cases.

Case	pGRF	vGRF	mGRF	Q/H_ratio	GTA_ratio
0	0.167	1.383	-0.176	6.275	18.351
5	1.781	7.732	0.087	36.534	31.173
10	0.169	1.393	-0.175	6.289	18.345
15	2.254	9.776	0.007	41.032	79.928
20	1.126	6.975	0.066	24.696	46.359
25	1.742	9.305	0.088	5.596	13.551
30	1.432	8.061	0.080	30.997	40.003

TABLE 4.15: GRF, Q/H force ratio and GTA force ratio at the time instant of peak vGRF for multiple trunk internal rotation angles.

In Table 4.16 we can observe kJRF and kJRM at maximum vGRF for all cases. AF obtains the lower value for the case of 5° and the highest for 25°. In general, greater AF values at max vGRF are observed for increased trunk internal rotation angles. Also, CF has lower values for 0° and 10° and increases for the remaining cases. AbdM and IRM receives the lowest values for the case with no rotation, following by 10° of trunk internal rotation.

Case	AF(+)	CF(-)	MF(+)	AbdM(+)	IRM(-)	FM(+)
0	3.756	-7.761	0.334	0.006	0.000	0.023
5	3.687	-12.384	0.271	0.104	-0.028	0.108
10	3.757	-7.768	0.332	0.007	0.001	0.023
15	4.006	-15.332	0.237	0.137	-0.029	0.102
20	4.921	-14.675	0.377	0.127	-0.023	0.198
25	6.076	-18.200	0.399	0.126	-0.027	0.238
30	5.049	-15.227	0.436	0.128	-0.032	0.177

TABLE 4.16: Knee joint JRF and JRM at the time instant of peak vGRF for multiple trunk internal rotation angles.

In Figure 4.33 we display angles of the hip, knee and ankle joints for single - leg landings with externally rotated trunk scenarios.

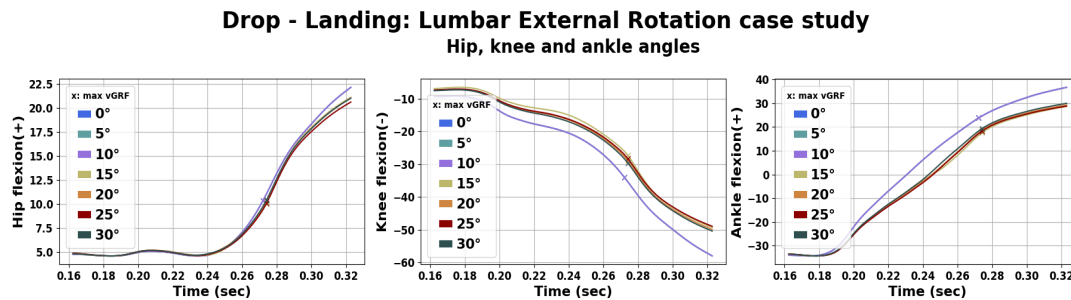


FIGURE 4.33: Hip, knee and ankle kinematics for multiple trunk external rotation angles.

In Figure 4.34 we demonstrate GRF and GRM for the studied scenarios. We can detect greater vGRF peaks for the cases with trunk external rotation greater than 10° , while lower values are observed for 0° , 5° and 10° of trunk external rotation.

Drop - Landing: Lumbar External Rotation case study Ground Reaction Forces and Moments (/BW)

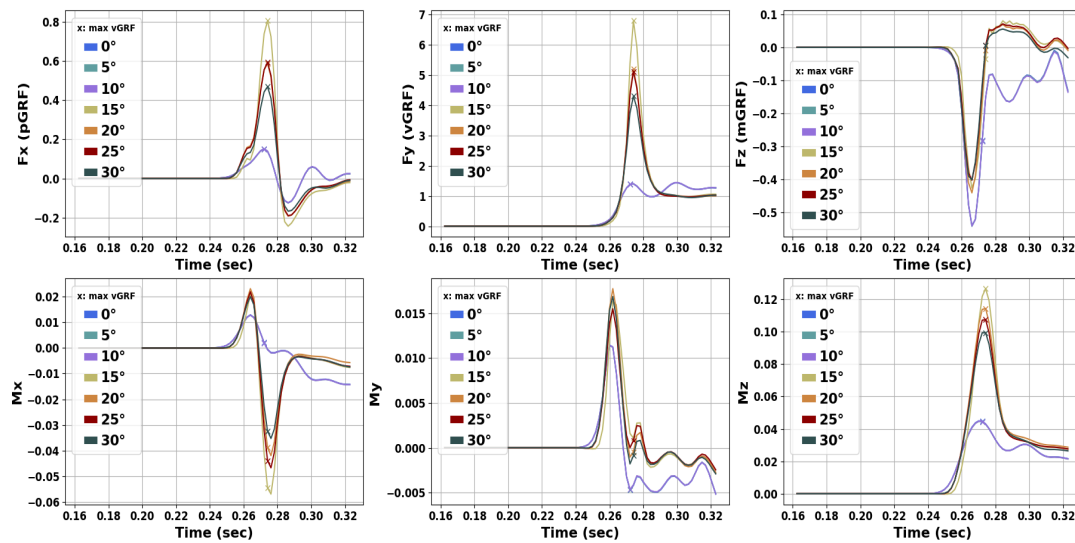


FIGURE 4.34: GRF and GRM for multiple trunk external rotation angles.

In Figure 4.35 we demonstrate kJRF and kJRM. Greater peaks of CF are noticed for 15° trunk external rotation following by 20°, 25°, 30°, 5°, 10°, 0° degrees respectively.

Drop - Landing: Lumbar External Rotation case study Knee Joint Reaction Forces and Moments (/BW)

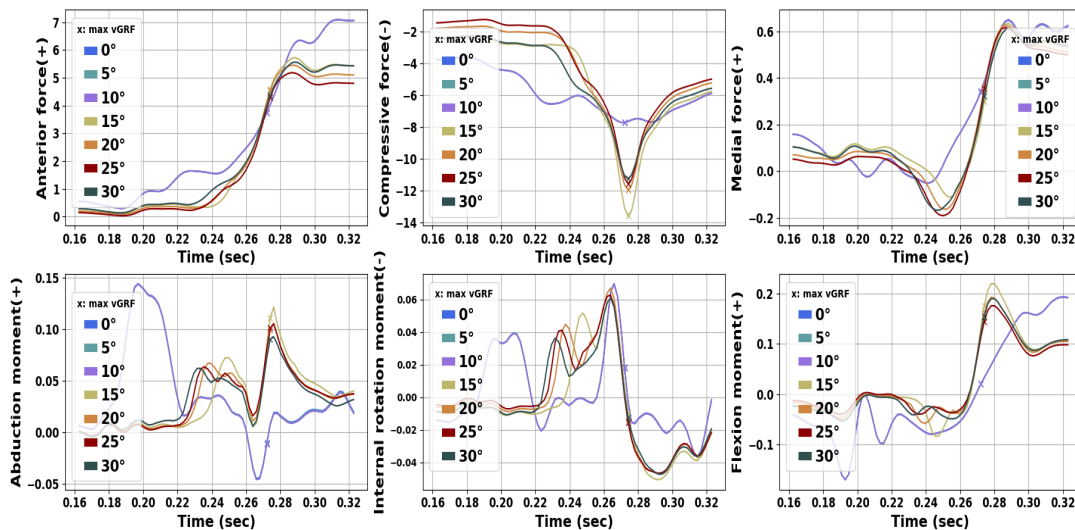


FIGURE 4.35: Knee joint JRF and JRM for multiple trunk external rotation angles.

In Figure 4.36 we demonstrate muscle forces and muscle force ratios. Greater hamstrings force and lower Q/H force ratio are spotted for the cases of 0°, 5° and 10° of trunk external rotation.

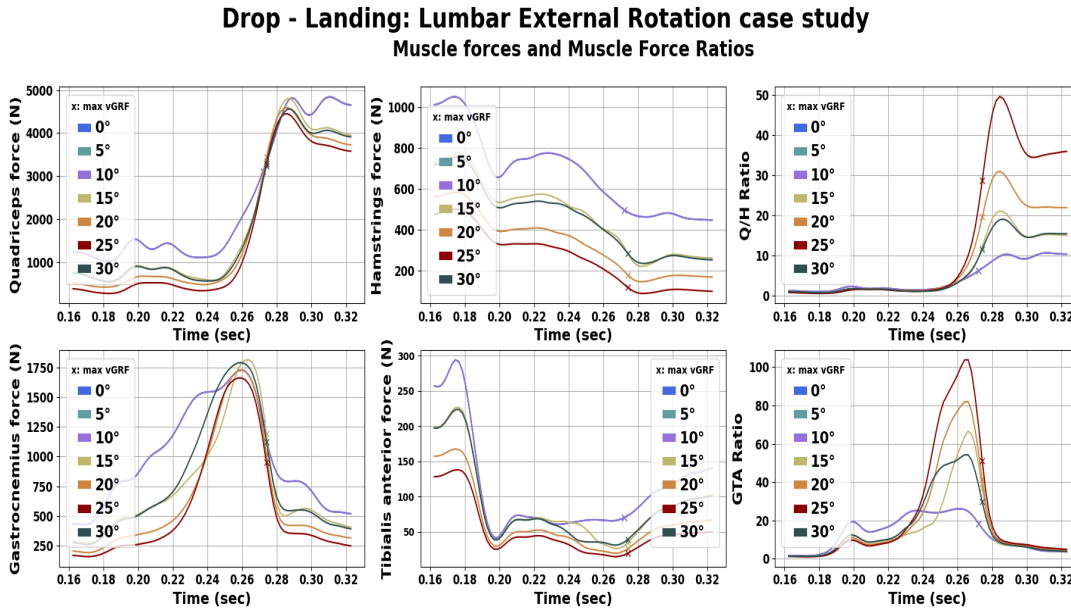


FIGURE 4.36: Muscle forces and muscle force ratios for multiple trunk external rotation angles.

In Table 4.17 and Table 4.18, values of parameters at the time instant of maximum vGRF for all cases are presented.

Case	pGRF	vGRF	mGRF	Q/H_ratio	GTA_ratio
0	0.167	1.383	-0.176	6.275	18.351
5	0.167	1.387	-0.177	6.273	18.315
10	0.168	1.387	-0.178	6.257	18.332
15	1.138	6.799	0.042	11.877	34.097
20	0.782	5.194	0.022	19.366	38.563
25	0.783	5.118	0.021	28.187	47.747
30	0.604	4.304	-0.007	11.482	28.361

TABLE 4.17: GRF, Q/H force ratio and GTA force ratio at the time instant of peak vGRF for multiple trunk external rotation angles.

In Table 4.18 we can compare easily the values of the desired parameters at maximum vGRF instant. AF and CF obtain greater values for cases with greater vGRF peaks compared with cases with lower vGRF peaks.

Case	AF(+)	CF(-)	MF(+)	AbdM(+)	IRM(-)	FM(+)
0	3.756	-7.761	0.334	0.006	0.000	0.023
5	3.757	-7.762	0.336	0.006	0.000	0.023
10	3.754	-7.762	0.337	0.005	0.000	0.022
15	4.730	-14.651	0.330	0.119	-0.019	0.182
20	4.623	-12.552	0.377	0.102	-0.020	0.165
25	4.373	-12.141	0.370	0.102	-0.021	0.149
30	4.421	-11.667	0.329	0.088	-0.015	0.158

TABLE 4.18: Knee joint JRF and JRM at the time instant of peak vGRF for multiple trunk external rotation angles.

4.4 Muscle force of knee joint agonists and antagonists case

In this section we demonstrate the results regarding cases where specific muscle groups were strengthened and weakened as presented in subsection 3.3.5. In the figures following, *nq* refers to normal quadriceps, *sq* refers to strong quadriceps, *wq* refers to weak quadriceps, *nh* refers to normal hamstrings, *sh* refers to strong hamstrings and *wh* refers to weak hamstrings.

Next, in Figure 4.37, angles for the hip, knee and ankle joints are displayed. If we take a close look at knee flexion, we can observe that for the scenarios where quadriceps are normal, the knee and ankle are more flexed.

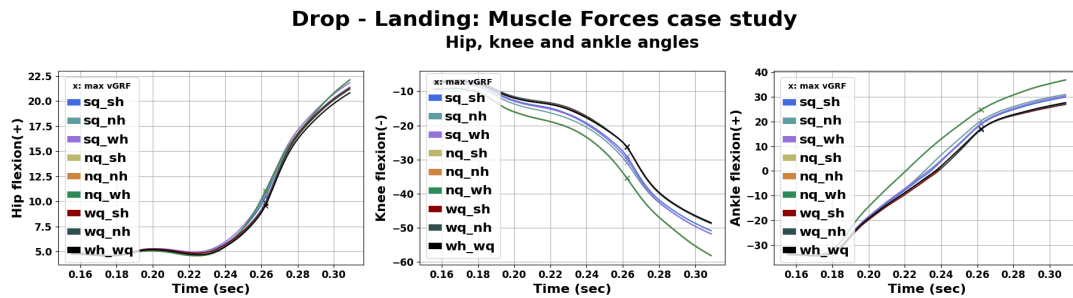


FIGURE 4.37: Hip, knee and ankle kinematics for scenarios of normal, weak and strong knee joint agonist antagonist muscles.

Moreover, in Figure 4.38 we demonstrate GRF and GRM for the examined scenarios. We detect the lowest peak vGRF values for the three cases with normal quadriceps. Also, the highest peak is noticed for the scenario with weak quadriceps and strong hamstrings.

Drop - Landing: Muscle Forces case study
Ground Reaction Forces and Moments (/BW)

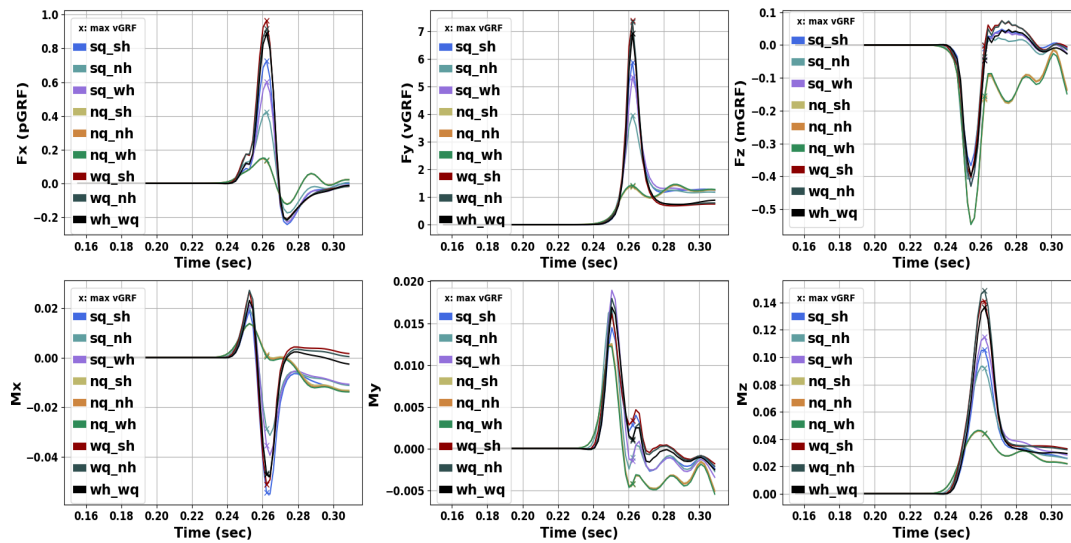


FIGURE 4.38: GRF and GRM for scenarios of normal, weak and strong knee joint agonist antagonist muscles.

Furthermore, in Figure 4.39 we demonstrate kJRF and kJRM for all studied scenarios. If we take a quick look at all knee joint JRF and JRM we can detect similar behavior for the three cases with normal quadriceps. For these three scenarios we notice lower CF peak around maximum vGRF and greater AbdM and IRM peaks at IGC.

Drop - Landing: Muscle Forces case study
Knee Joint Reaction Forces and Moments (/BW)

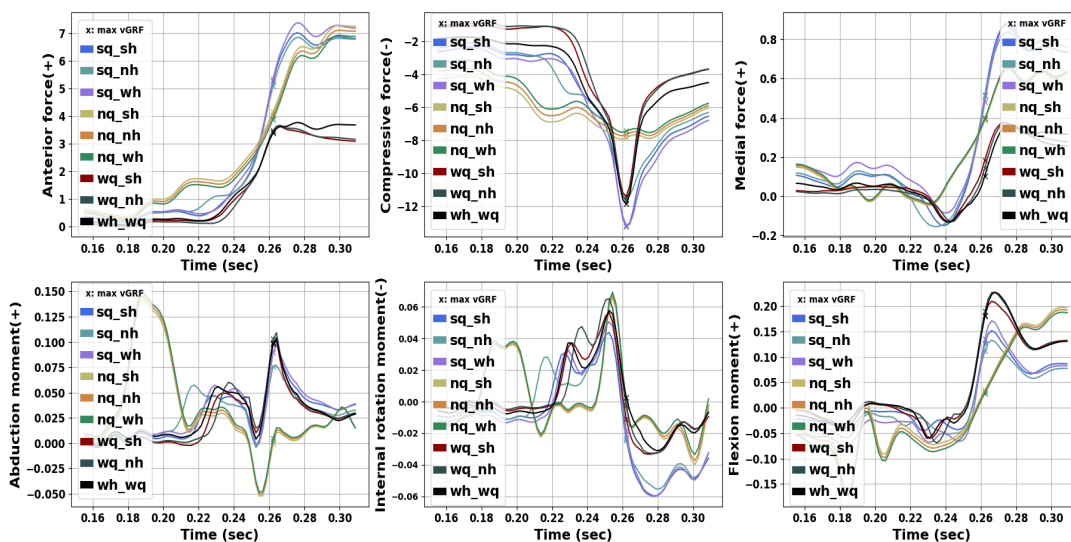


FIGURE 4.39: Knee joint JRF and JRM for scenarios of normal, weak and strong knee joint agonist antagonist muscles.

Afterwards, we demonstrate muscle forces and muscle force ratios for the previously mentioned cases (Figure 4.40). Hamstrings group force obtains the highest value for the scenario with strong hamstrings and normal quadriceps.

Also, the lowest values for hamstrings forces are observed for the scenarios with weak quadriceps.

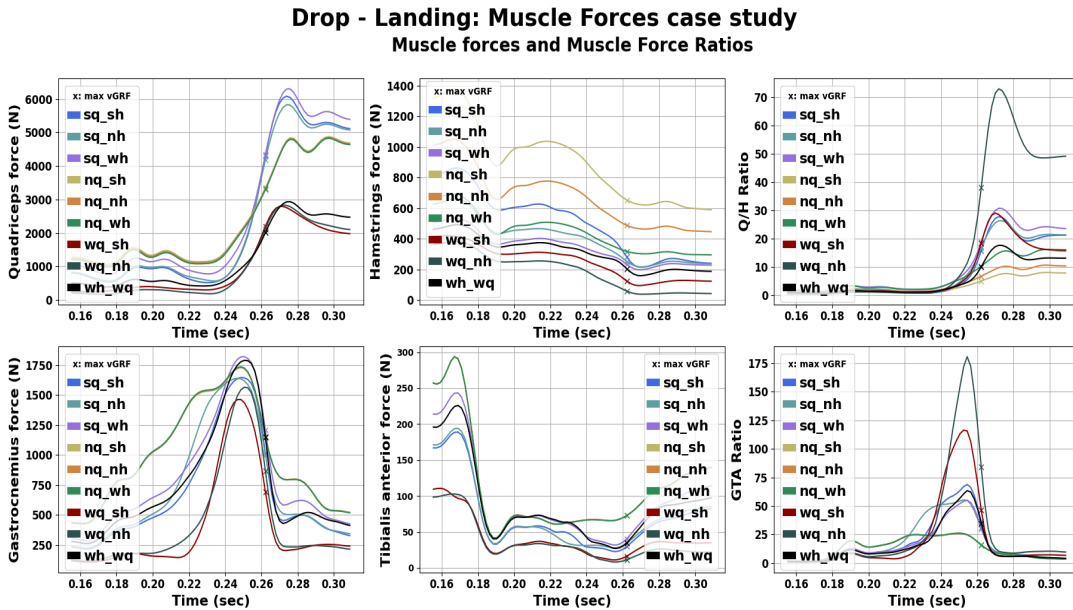


FIGURE 4.40: Muscle forces and muscle force ratios for scenarios of normal, weak and strong knee joint agonist antagonist muscles.

Finally, in Table 4.19 and Table 4.20 we present values for the studied parameters at the maximum vGRF. We observe that the highest vGRF peak occurs for the weak quadriceps and strong hamstrings case. Moreover, the weak quadriceps and normal hamstrings scenario obtains the highest Q/H force ratio value at peak vGRF. On the contrary, the normal quadriceps and strong hamstrings case obtains the lowest Q/H force ratio value at peak vGRF.

Case	pGRF	vGRF	mGRF	Q/H_ratio	GTA_ratio
sq_sh	1.009	5.889	-0.001	15.529	33.423
sq_nh	0.542	3.964	-0.037	16.627	28.490
sq_wh	0.827	5.355	0.005	18.631	29.356
nq_sh	0.146	1.362	-0.119	5.149	15.552
nq_nh	0.149	1.388	-0.114	6.836	15.597
nq_wh	0.152	1.417	-0.109	10.406	15.649
wq_sh	1.362	7.387	0.051	18.101	40.877
wq_nh	1.305	7.344	0.040	36.620	74.210
wq_wh	1.259	6.930	0.014	9.886	32.315

TABLE 4.19: GRF, Q/H force ratio and GTA force ratio at the time instant of peak vGRF for scenarios of normal, weak and strong knee joint agonist antagonist muscles.

Furthermore, in Table 4.20 we observe that the scenarios with greater peak vGRF acquire lower AF and MF values. On the contrary, AbdM values are greater for these scenarios at peak vGRF.

Case	AF(+)	CF(-)	MF(+)	AbdM(+)	IRM(-)	FM(+)
sq_sh	5.379	-14.038	0.532	0.098	-0.030	0.132
sq_nh	5.142	-11.786	0.513	0.072	-0.025	0.114
sq_wh	5.450	-13.827	0.502	0.094	-0.025	0.140
nq_sh	4.168	-7.852	0.391	0.006	-0.010	0.035
nq_nh	4.035	-7.657	0.395	0.008	-0.009	0.032
nq_wh	3.901	-7.460	0.401	0.011	-0.009	0.029
wq_sh	3.639	-12.622	0.207	0.105	-0.019	0.189
wq_nh	3.642	-12.906	0.174	0.111	-0.012	0.197
wq_wh	3.553	-13.030	0.129	0.104	-0.006	0.186

TABLE 4.20: Knee joint JRF and JRM at the time instant of peak vGRF for scenarios of normal, weak and strong knee joint agonist antagonist muscles.

4.5 Moco Control goal weight case

As described in subsection 3.3.6, we assigned different weights to the Moco control objective functions that can be interpreted as the effort minimization cost. The examined weights for this goal were 0, 0.1, 0.2, 0.5, 1, 2, 5 and 10, and the results are presented comparatively in this section.

Initially, in Figure 4.41 we display the angle trajectories for the hip, knee and ankle joints for all case studies. We notice that for zero weight, ankle and hip flexion angles are greater for the entire motion. On the contrary, knee flexion angle obtain lower values compared with higher weight cases.



FIGURE 4.41: Hip, knee and ankle kinematics for different weights of Moco Control goal.

Next, in Figure 4.42 we demonstrate GRF and GRM for the examined cases. We observe that the peak vGRF is lower for zero weight and it is increased for 0.1 and 0.2, reaching even greater values for 1, 2, 5 and 10 weights. The same observation is also valid for the maximum pGRF values.

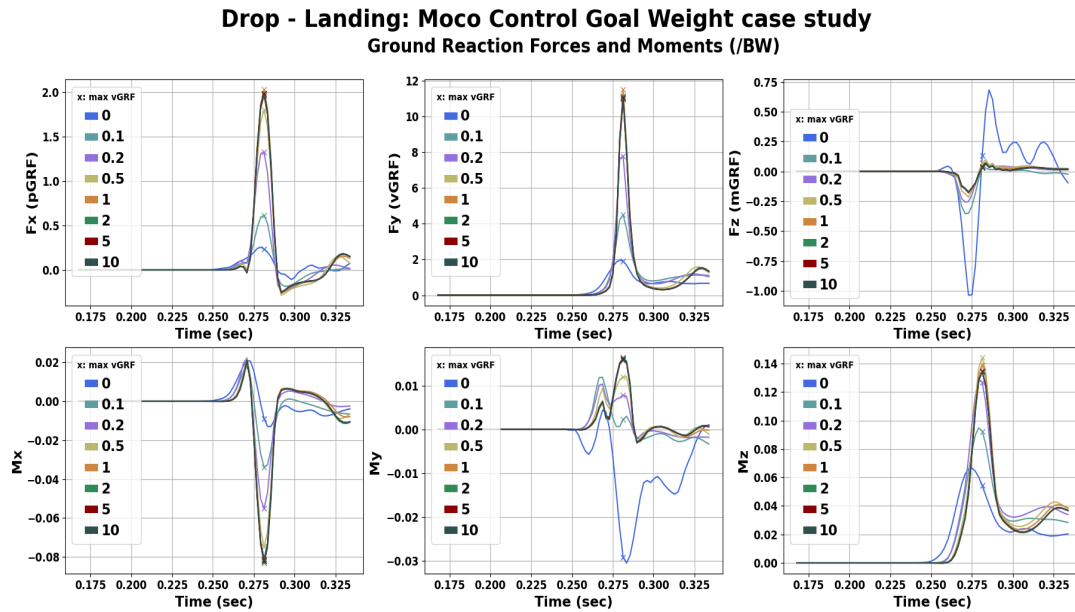


FIGURE 4.42: GRF and GRM for different weights of Moco Control goal.

Moreover, Figure 4.43 demonstrates kJRF and kJRM for the respective scenarios. We notice that for control goal with 0 weight the results are quite different compared to the remaining cases. More specifically, AF is higher for zero weight and as the weight is increased, the force is decreased at max vGRF time. Also, for the cases with 1, 2, 4 and 10 weight we notice that the results are close. Moreover, we detect greater AbdM and rotation moment for the case with zero weight compared with higher values of effort goal weight. It is obvious that the lack of the Control Goal (zero weight) highly affects the forces and moments on the knee joint resulting in much greater values for the entire motion despite the lower vGRF peak.

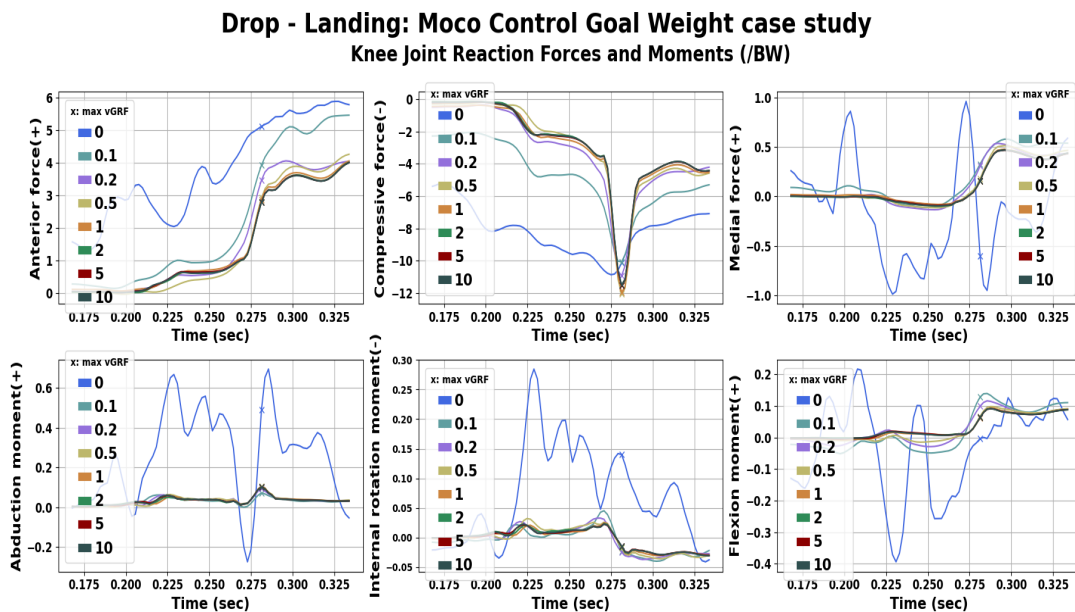


FIGURE 4.43: Knee joint JRF and JRM for different weights of Moco Control goal.

Furthermore, in Figure 4.44 muscle forces and muscle force ratios for all cases examined with different control goal weights are presented. As expected, in general muscle forces are greater for lower effort goal values. Furthermore, for weight greater than 0.5 no great differences are observed. Again we notice a great deviation for the case with no effort goal with much higher values of muscle forces compared with the other cases. As a result, Q/H force ratio and GTA force ratio at max vGRF are greater for larger effort weights and very low in the absence of effort goal.

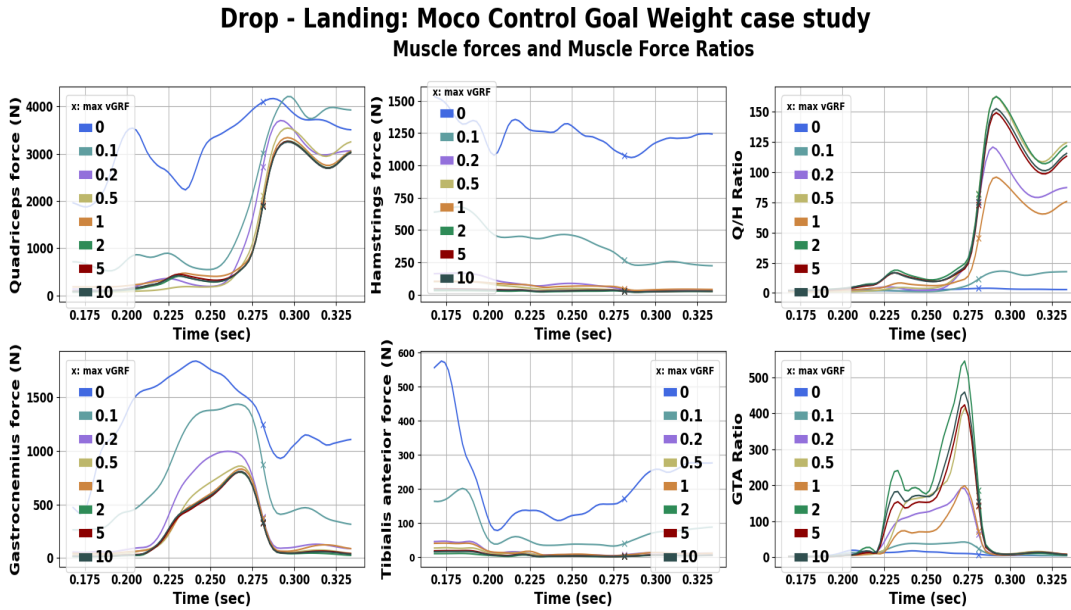


FIGURE 4.44: Muscle forces and muscle force ratios for different weights of Moco Control goal.

In addition, in Table 4.21 and Table 4.22, values for the previously examined parameters at maximum vGRF for all cases are presented. We notice that as the effort goal weight is increased vGRF is also increased until weight of 1, then for weights 2, 5 and 10 values greater than 10 times BW are detected. Q/H force ratio is also very low for the case with no Control Goal.

Case	pGRF	vGRF	mGRF	Q/H_ratio	GTA_ratio
0	0.284	1.967	-0.469	3.724	7.918
0.1	0.792	4.499	-0.001	11.544	22.167
0.2	1.772	7.779	0.081	74.678	56.125
0.5	2.658	11.116	0.206	78.301	113.327
1	3.013	11.479	0.163	42.970	55.000
2	2.923	11.113	0.146	77.616	137.173
5	2.885	11.043	0.148	69.774	104.952
10	2.876	10.964	0.140	72.103	117.775

TABLE 4.21: GRF, Q/H force ratio and GTA force ratio at the time instant of peak vGRF for different weights of Moco Control goal.

Moreover, based on Table 4.22 we observe that AF and MF obtain lower values as the Control Goal weight is increased at peak vGRF. On the contrary, CF is augmented for higher control goal weights at the same time instant. In addition, for 0 weight we notice greater value of AbdM compared with other weights. Also, at max vGRF ERM is detected while for the other cases low values of IRM are detected.

Case	AF(+)	CF(-)	MF(+)	AbdM(+)	IRM(-)	FM(+)
0	4.956	-10.666	-0.080	0.203	0.137	-0.047
0.1	4.002	-10.602	0.320	0.076	-0.020	0.138
0.2	3.604	-12.223	0.277	0.103	-0.032	0.107
0.5	3.225	-14.880	0.149	0.144	-0.035	0.071
1	3.235	-15.044	0.127	0.145	-0.031	0.065
2	3.143	-14.505	0.132	0.139	-0.028	0.067
5	3.141	-14.430	0.131	0.139	-0.027	0.066
10	3.122	-14.344	0.133	0.135	-0.030	0.067

TABLE 4.22: Knee joint JRF and JRM at the time instant of peak vGRF for different weights of Moco Control goal.

Chapter 5

Discussion

In this chapter, we present our results in comparison with other studies in literature in an attempt to identify common conclusions and discuss any divergences that may arise.

5.1 Initial height case

In section 4.1, we presented the simulation results for drop - landings from different landing heights. We examined single - leg landings from 30, 35, 40, 45, 50 and 55cm height. The results clearly indicated the association of the landing height with the assessed ACL injury risk factors.

First, we noticed that as the landing height was increased the landing forces (GRF) were also incremented. This was in agreement with other research studies (Mokhtarzadeh et al., 2010; Mokhtarzadeh et al., 2013). Mokhtarzadeh et al. examined single - leg landings from 30 and 60cm of height and observed greater GRF peaks for landings from 60cm (Mokhtarzadeh et al., 2012). More specifically, peak vGRF was 3.24 times BW when landing from 30cm height and 4.38 when landing from 60cm height. Nevertheless, in our study we observed lower peak values of vGRF ranging from 1,43 to 1,79 times BW for all examined landing heights. However, the GRF should be evaluated taking into account the muscle forces as there is a correlation between these two parameters as it will be described below and in section 5.5.

Furthermore, in Table 4.2 we observed that at max vGRF the AF was increased for greater heights. On the contrary, CF and MF were decreased for increased landing heights. In a research study conducted by Verniba et al., peak CF was greater for greater heights (Verniba et al., 2017) at peak knee flexion moment. In our case, this peak coincides with the peak vGRF. However, in this instant our results demonstrate that CF does not increase with height. Nonetheless, we observe that CF was greatly increased for greater heights at a short time instant after IGC (at about 0.22 sec in Figure 4.3). The same holds true for the AbdM.

This discrepancy could be related to the modified Hunt – Crossley ground - foot contact model adopted in our study, as presented in subsection 3.1.1.1. The values for parameters like stiffness, dissipation and friction were assigned based on other research studies (Serrancolí et al., 2019). Moreover, the position and total number of the contact spheres were adopted by (SimTK - confluence, Sky High 2011b) a study for simulating a standing vertical jump. In general, insight into foot - ground contact during landing motion is limited and the

proposed model might not accurately capture contact geometries affecting the predicted motion. This holds true for all the simulation scenarios we evaluated.

Furthermore, in our study quadriceps and hamstring forces did not present great differences among the different scenarios. On the contrary, Mokhtarzadeh et al. observed greater quadriceps and hamstring forces for higher initial height. In our study, the peak of quadriceps force was detected around maximum vGRF (with values 4500-5000N). These values were greater than those reported by other research studies ((Mokhtarzadeh et al., 2013)). Also, hamstrings force obtained lower values in our simulations compared to the results reported by Mokhtarzadeh et al. At max vGRF hamstring force was around 500N in our case, while Mokhtarzadeh reported values around 1000N for landing from 60cm height. However, we should mention that muscle forces are greatly dependent on the effort goal that is defined in Moco, as will be demonstrated in section 5.5. This also affects GRF as stated previously.

Also, Mokhtarzadeh et al. emphasized on Q/H force ratio and stated that it was decreased when the vGRF was at its peak value which is also valid in our study. Regarding Q/H force ratio, we detected that it was decreased as the initial landing height was increased at max vGRF. In agreement with our results, Mokhtarzadeh et al. stated that Q/H force ratio was lower for the landing from 60cm compared with a landing from 30cm. It should be mentioned that in our study we observed much higher values of Q/H force ratio at time of max vGRF for all examined scenarios. Again, differences between the studies could be due to the selected weight of the Moco control cost.

In a recent study ACL loading was correlated to landing height. For drop - landings from 30 and 60cm, ACL loading was predicted and the authors concluded that for greater heights the loading was increased indicating highest risk of injury (Mokhtarzadeh et al., 2017). In our study, we did not estimate ACL forces. Nonetheless, AF is inherently related with ACL loads and in our study was greater for increased heights.

5.2 Hip rotation case

Several studies have examined the influence of static lower extremity alignment in ACL injuries (Nguyen, Shultz, and Schmitz, 2015; Peel et al., 2020; Koga et al., 2017). More specifically, the hip rotational alignment has been associated with knee valgus posture and ACL injuries. Yasada et al. and Koga et al. studied landings from handball players where ACL injuries took place and observed that in the majority of landings with injury, the hip was internally rotated (Yasuda et al., 2016; Koga et al., 2017). Peel et al. at their study compared landings with toe - in, toe - out and neutral position of the lower limb and concluded that the toe - out position could protect from injury while the toe - in position is associated with increased risk (Peel et al., 2020).

In this thesis we also examined the influence of hip rotation in parameters associated with ACL injuries. In section 4.2 we presented the results concerning cases with different hip rotation angles. First, we presented comparative

figures for the cases with internally rotated hip and then for the externally rotated cases.

Initially, regarding the hip internal rotation scenarios we observed that the minimum vGRF peak was for the 20° case (3.602 times BW). Although, for that scenario we detected greater AbdM and IRM at peak vGRF (0.044 and -0.043 times BW respectively). Nevertheless, for the 0° hip internal rotation scenario the peak vGRF was 3.602 times BW while AbdM, IRM were 0.020 and -0.034 respectively. As the hip internal rotation was increased further, peak vGRF was also increased (reaching the value of 4.658 times BW for the 30° scenario).

Nguyen et al. claimed that when the hip was internally rotated and the knee was in a valgus posture, then the average knee ERM was greater compared with a neutral position. On the other hand, Peel et al. found an association between the toe - in landing position and knee IRM. In our study we found that at peak vGRF we have IRM with very small differences between the values for each case (Figure 4.7). However, we can also notice that we have a peak ERM right before peak vGRF for all cases. Also, we observed the lowest AbdM at peak vGRF for the 0° and 10° scenarios, while the remaining scenarios presented greater values.

Furthermore, we examined scenarios with externally rotated hip. In these scenarios we spotted the lowest vGRF peaks for the 10° and 15° hip external rotation scenarios. Also, at peak vGRF time instant the 0° hip rotation scenario had greater AF, MF, AbdM and IRM compared with the scenarios featuring externally rotated hip. On a similar note, Peel et al. claimed that the toe - out position was associated with decreased knee AddM and therefore lower ACL injury risk. In our study, we see that for increased but not excessive external hip rotation angles, the AF is noticeably smaller converging to the same conclusion. Last but not least, we noticed that as the hip external rotation angle was increased, the Q/H force ratio was also decreased.

Summarizing, we could claim that the internally rotated hip position could possibly be associated with ACL injuries due to increased values in risk factors. On the contrary, the externally rotated hip position may be considered safer due to lower values in risk factors. Landing with 10° or 15° externally rotated hip can possibly be safer due to lower GRF.

5.3 Trunk orientation case

Multiple studies have examined the influence of trunk orientation in the observed kinematics, GRF and kJRF during drop - landings. A leaning forward trunk has been associated with more flexion of the hip and knee joints and lower values of pGRF, vGRF and lower mean amplitude of quadriceps EMG compared with an upright position during drop landings (Blackburn and Padua, 2008; Blackburn and Padua, 2009). In another study, results were quite similar. Upright position during landings was linked with greater peak of vGRF, lower gastrocnemius and quadriceps activation and greater knee extensor moments (Shimokochi et al., 2012). In our study, we demonstrated that for all examined cases, landings that favored a forward leaning position

resulted in lower risk of ACL injury. Specifically, we observed that when the trunk was leaning forward with 25° the peak vGRF was lower, following by 30°, and 10°. However, the lowest vGRF value was observed for the case of no flexion. This can be due to the initial guess given to the study. Also, for the case of 25° of trunk flexion AbdM and IRM were lower compared with other angles of trunk flexion.

Regarding landings with trunk leaning backwards, as a general remark, we observed greater vGRF compared with the upright position as the lumbar extension angle was increased. Additionally, Q/H force ratio, CF, AbdM and IRM were greater at time of maximum vGRF for the cases of landings with trunk in backwards leaning. Also, Saito et al. observed greater knee valgus angles when landing in a trunk extension position compared with landings with trunk neutral position (Saito et al., 2020), which is in agreement with the AbdM values detected in our results.

Concerning the trunk bending, Saito et al. observed that landings with the trunk leaning towards the opposite side of the landing leg or toward to the landing side led to greater values of knee valgus angles (Saito et al., 2020). In our case we observed that greater AbdM values occurred as the right or left bending angle was increased compared with the neutral position, that would introduce an increased valgus angle. Also, Jones et al. noticed greater GRF and knee joint loads when leaning in the opposite direction of landing. Similarly, in our study we observed that the largest peak vGRF occurred when bending towards the right direction that is opposite to the landing leg with a value of 8.632 per BW.

Regarding landings with internal or external rotation, we noticed that for the cases with 5° and 10° degrees of external rotation of the trunk and 10 degrees of internal rotation peaks of equal amplitude with the upright case occurred. For the rest of the trunk rotation angles, we noticed a large increase in the amplitude of the vGRF peaks.

5.4 Muscle force of knee joint agonists and antagonists case

In this study, we investigated how permutations of max isometric force for the knee joint agonist and antagonist muscles affect the parameters of interest, namely vGRF and AF (section 4.4). Again, a direct comparison with other research studies was not feasible.

In our study, we observed that varying the maximum isometric force of these two muscle groups affected all simulation results. We discerned that hamstrings force was the greatest for the scenario with strong hamstrings and normal quadriceps, following by the scenario where both muscles were normal. An unexpected outcome was that the lowest hamstrings forces were detected for the cases of weak quadriceps. This outcome clearly indicates how muscles work in conjunction and the significance of the muscle redundancy issue. This concept is related to the uncertainty of contribution for each in a given task.

The lowest peaks of vGRF were detected for the following scenarios in augmented order: normal quadriceps and strong hamstrings, normal quadriceps and normal hamstrings and normal quadriceps and weak hamstrings with values 1.362, 1.388 and 1.417 times BW respectively. The greatest peak of vGRF was observed for the scenario of weak quadriceps and strong hamstrings. For the cases with lower peaks of vGRF, greater values of AF were noticed at time of maximum vGRF.

It should be emphasized that the cases with normal quadriceps present similar behavior despite hamstrings strengthening or weakening. For these scenarios we observed lower vGRF, Q/H force ratio, GTA force ratio, knee joint CF and AbdM. Although, AF was higher for these scenarios compared with the scenarios with weak quadriceps, but lower compared with the scenarios with strong quadriceps.

5.5 Moco Control goal weight case

Finally, we investigated how the Moco Control Goal (or the effort) affects the simulation results. We cannot compare our results with other research studies because we couldn't find studies with similar content. We assumed that this case study would offer a more clear view for the other case studies in our work, especially regarding the connection between GRF and muscle forces.

In section 4.5, we observed that as we increased the weight of the control goal, peak vGRF was also increased reaching a maximum value of 11.479 times BW for weight of 1. In general, for the upper limit weight values we noticed increased vGRF peaks. The same pattern was also spotted for the Q/H force ratio. In contrast, we observed that as the weight was increased, AF was decreased, although the differences between the peak values above the 0.1 weight are not very large. Regarding muscle forces, as it was expected for greater weights of the goal lower muscle forces were detected since the objective function introduced to the problem tries to minimize the sum of the absolute value of the controls. Again, no great differences were observed between the cases with weight greater than 0.1.

Conclusions

In this work, we presented a pipeline that aims to predict and identify key parameters of interest that are related to ACL injury during single - leg landings. First, we provided the basic theoretical concepts of the subject under consideration. We started from a general description of the lower limb anatomy and physiology. Emphasis was given to the knee joint with its surrounding anatomical structures and especially the ACL ligament. We also described muscle physiology and a muscle modeling approach that captures the physiological properties of muscle functionality. Moreover, we provided a high - level description of multibody dynamics and a brief introduction into trajectory optimization methods, as the tools that we used throughout this work are built upon these fundamental concepts. We finally presented related studies in an effort to gather all risk factors related to ACL injury during landings. In this thesis, we focused on the following parameters: vGRF, AF, AbdM, and Q/H force ratio ratio.

Next, we described in detail the methods we followed to perform our study, starting from the software packages we deployed. These were the OpenSim, SCONE and Moco interfaces. OpenSim was used to modify available musculoskeletal models to include a compliant ground - foot contact model and the Analysis tool to perform JRA analysis and extract information about muscle forces for all our assessed studies. As a first step SCONE was used to acquire a single case of single - leg landing that acted as an initial guess for all subsequent Moco simulations. These tools are based on different approaches regarding trajectory optimization. Moco is based on direct collocation methods that lead to faster predictive simulations. This is one of the main reasons that we chose Moco as our preferred option. To obtain a quick initial guess from SCONE we used a simplified model. Then, for the following Moco studies we used models with a gradually increased complexity. This offered us the ability to provide an adequate initial guess to all investigated cases, that led to quick and efficient predictive simulations.

Subsequently, we presented the results for the following conditions of single - leg landing: a) initial landing height, b) hip internal and external rotation, c) trunk forward - backward leaning, d) trunk medial - lateral bending, e) trunk internal - external rotation and f) muscle forces permutations. We also tested the effect of Moco control goal weight on the derived results.

Starting from the landing height we concluded that vGRF, AF, and AbdM increased as the height increased. On the other hand the opposite holds true for Q/H force ratio ratio. These findings are in agreement with similar studies. Next, regarding the internal hip rotation we observed that in general

vGRF, AF, and AbdM increase with larger hip rotations. On the contrary, a range of hip external rotation between 10° - 15° demonstrated lower values for vGRF. AF had the lowest value for a hip external rotation of 20° . These findings in general agree with literature, where a toe - out posture is associated with lower ACL injury risk. Regarding trunk forward leaning, vGRF was lower for the upright posture. A similar behavior was observed for backward trunk leaning. As a conclusion we can state that an upright posture seems to reduce vGRF. The same holds in general true for trunk lateral - medial bending and internal external rotation. Furthermore, we investigated how modifying muscle forces for quadriceps and hamstrings affected the injury risk factors. An interesting observation is that modifications of quadriceps force capacity greatly affects hamstrings force production. Moreover, when quadriceps were unchanged, the vGRF and AbdM demonstrated the lowest values, regardless of hamstrings force modifications. On the other hand this is not the case for AF. This observation clearly exhibits the inherent complexity of the ACL injury mechanism. Finally, we investigated how the Moco control cost weight affects muscle forces and subsequently all landing and knee joint forces and moments. This objective function is closely related to effort that furthers affects muscle activation and force production. We observed that lower weights greatly reduced vGRF but increased AF, AbdM and ERM. As a general conclusion we can say that AF and vGRF demonstrate an opposite behavior in all cases, where an increase in vGRF is accompanied by a decrease of AF.

Our study clearly demonstrates that ACL injury is a rather complicated mechanism with many associated risk factors. These factors are clearly not independent. Therefore, one cannot clearly study the phenomenon without considering this correlation between these inherently different variables. Of course, our work does not come without any limitations, especially considering the adopted modeling assumptions. First, we deployed musculoskeletal models that feature one DoF knee joint without modeling the contribution of other structures such as cartilages and ligaments. Especially, we think that the absence of a suitable contact model between the femoral and tibial knee compartments greatly affects our results. The same observation can be made for the ground - foot contact model and CoP estimation. Also, we did not assess different population classes that feature varying anthropometric data. All these limitations can serve as the foundations for future work to improve our current pipeline. Nonetheless, our pipeline clearly showcased the promising potential of predictive simulations to evaluate different aspects of complicated phenomena, such as the ACL injury. Moreover, our findings are in general agreement with similar studies. Finally, we envision that further improvements can lead to a pipeline that can be used by physiotherapists and clinicians on adjusting rehabilitation and training plans based on subject - specific characteristics.

Bibliography

- [1] URL: <https://simtk.org/projects/simbody>.
- [2] 2005-2012. URL: <https://simtk.org/projects/opensim>.
- [3] 2011. URL: <https://simtk-confluence.stanford.edu:8443/display/OpenSim/Documentation?desktop=true¯oName=divbox>.
- [4] 2011. URL: <https://simtk-confluence.stanford.edu:8443/display/OpenSim/Sky+High%3A+Coordinating+Muscles+for+Optimal+Jump+Performance>.
- [5] 2019. URL: <https://boneandspine.com/normal-biomechanics-of-knee/>.
- [6] 2019. URL: <https://simtk.org/projects/scone>.
- [7] 2020. URL: <https://www.biodigital.com/>.
- [8] 2020. URL: <https://opensim-org.github.io/opensim-moco-site/>.
- [9] 2021. URL: <https://www.mayoclinic.org/>.
- [10] 2021. URL: <https://www.howtorelief.com/>.
- [11] 2021. URL: <https://www.kenhub.com/en/library/anatomy/lower-extremity-anatomy>.
- [12] 2021. URL: <https://www.hopkinsmedicine.org/about/>.
- [13] Maarten Afschrift et al. "The effect of muscle weakness on the capability gap during gross motor function: A simulation study supporting design criteria for exoskeletons of the lower limb". In: *Biomedical engineering online* 13 (Aug. 2014), p. 111. DOI: [10.1186/1475-925X-13-111](https://doi.org/10.1186/1475-925X-13-111).
- [14] Tunc Akbas, James Sulzer, and Rick Neptune. *Neuromusculoskeletal simulation reveals abnormal rectus femoris-gluteus medius reflex coupling in post-stroke gait: Supplementary figures and tables*. Dec. 2018. DOI: [10.1101/501072](https://doi.org/10.1101/501072).
- [15] Wilberth Alcocer et al. "Major trends in the development of ankle rehabilitation devices". In: *DYNA* 79 (Dec. 2012), pp. 45–55.
- [16] Frank Anderson and MARCUS Pandy. "A Dynamic Optimization Solution for Vertical Jumping in Three Dimensions". In: *Computer methods in biomechanics and biomedical engineering* 2 (Feb. 1999), pp. 201–231. DOI: [10.1080/10255849908907988](https://doi.org/10.1080/10255849908907988).
- [17] Allison Arnold et al. "The role of estimating muscle-tendon lengths and velocities of the hamstrings in the evaluation and treatment of crouch gait". In: *Gait & posture* 23 (May 2006), pp. 273–81. DOI: [10.1016/j.gaitpost.2005.03.003](https://doi.org/10.1016/j.gaitpost.2005.03.003).

- [18] *Basic Sciences*. 2016. URL: <https://musculoskeletalkey.com/basic-sciences/>.
- [19] Nathaniel Bates et al. "Knee Abduction Affects Greater Magnitude of Change in ACL and MCL Strains Than Matched Internal Tibial Rotation In Vitro". In: *Clinical Orthopaedics and Related Research* 475 (Apr. 2017). DOI: [10.1007/s11999-017-5367-9](https://doi.org/10.1007/s11999-017-5367-9).
- [20] Nathaniel Bates et al. "Multiplanar Loading of the Knee and Its Influence on Anterior Cruciate Ligament and Medial Collateral Ligament Strain During Simulated Landings and Noncontact Tears". In: *The American Journal of Sports Medicine* 47 (May 2019), p. 036354651985016. DOI: [10.1177/0363546519850165](https://doi.org/10.1177/0363546519850165).
- [21] Lefteris Benos et al. "A Review on Finite Element Modeling and Simulation of the Anterior Cruciate Ligament Reconstruction". In: *Frontiers in Bioengineering and Biotechnology* 8 (Aug. 2020), p. 967. DOI: [10.3389/fbioe.2020.00967](https://doi.org/10.3389/fbioe.2020.00967).
- [22] B Bigland-Ritchie et al. "Task-Dependent Factors in Fatigue of Human Voluntary Contractions". In: *Advances in experimental medicine and biology* 384 (Feb. 1995), pp. 361–80. DOI: [10.1007/978-1-4899-1016-5_29](https://doi.org/10.1007/978-1-4899-1016-5_29).
- [23] Troy Blackburn and Darin Padua. "Influence of trunk flexion on hip and knee joint kinematics during a controlled drop landing". In: *Clinical biomechanics (Bristol, Avon)* 23 (Mar. 2008), pp. 313–9. DOI: [10.1016/j.clinbiomech.2007.10.003](https://doi.org/10.1016/j.clinbiomech.2007.10.003).
- [24] Troy Blackburn and Darin Padua. "Sagittal-Plane Trunk Position, Landing Forces, and Quadriceps Electromyographic Activity". In: *Journal of athletic training* 44 (Mar. 2009), pp. 174–9. DOI: [10.4085/1062-6050-44.2.174](https://doi.org/10.4085/1062-6050-44.2.174).
- [25] Barry Boden et al. "Mechanisms of Anterior Cruciate Ligament Injury". In: *Orthopedics* 23 (July 2000), pp. 573–8. DOI: [10.3928/0147-7447-20000601-15](https://doi.org/10.3928/0147-7447-20000601-15).
- [26] Muge Bulat et al. "Musculoskeletal Simulation Tools for Understanding Mechanisms of Lower-Limb Sports Injuries". In: *Current Sports Medicine Reports* 18 (June 2019), pp. 210–216. DOI: [10.1249/JSR.0000000000000601](https://doi.org/10.1249/JSR.0000000000000601).
- [27] Matej Daniel et al. "Biomechanical analysis of local and global strengthening of gluteus medius". en. In: *Turk J Phys Med Rehabil* 63.3 (Aug. 2017), pp. 283–285.
- [28] William E. Prentice Daniel Arnheim. *Principles of Athletic Training*. William C Brown Pub, 1997. ISBN: 9780815103264.
- [29] Friedl De Groote et al. "Evaluation of Direct Collocation Optimal Control Problem Formulations for Solving the Muscle Redundancy Problem". In: *Annals of Biomedical Engineering* 44 (Mar. 2016). DOI: [10.1007/s10439-016-1591-9](https://doi.org/10.1007/s10439-016-1591-9).

- [30] Scott Delp et al. "An interactive graphics-based model of the lower extremity to study orthopaedic surgical procedures". In: *IEEE transactions on bio-medical engineering* 37 (Sept. 1990), pp. 757–67. DOI: [10.1109/10.102791](https://doi.org/10.1109/10.102791).
- [31] Christopher Dembia et al. "OpenSim Moco: Musculoskeletal optimal control". In: *PLOS Computational Biology* 16 (Dec. 2020), e1008493. DOI: [10.1371/journal.pcbi.1008493](https://doi.org/10.1371/journal.pcbi.1008493).
- [32] Thomas Donelon et al. "Biomechanical Determinants of Knee Joint Loads Associated with Increased Anterior Cruciate Ligament Loading During Cutting: A Systematic Review and Technical Framework". In: *Sports Medicine - Open* 6 (Nov. 2020). DOI: [10.1186/s40798-020-00276-5](https://doi.org/10.1186/s40798-020-00276-5).
- [33] Victoria Duthon et al. "Anatomy of the anterior cruciate ligament". In: *Knee surgery, sports traumatology, arthroscopy : official journal of the ESSKA* 14 (Apr. 2006), pp. 204–13. DOI: [10.1007/s00167-005-0679-9](https://doi.org/10.1007/s00167-005-0679-9).
- [34] Karsten Engel, Rainer Herpers, and Ulrich Hartmann. "Biomechanical Computer Models". In: Nov. 2011. ISBN: 978-953-307-851-9. DOI: [10.5772/23817](https://doi.org/10.5772/23817).
- [35] Thomas Geijtenbeek. "SCONE: Open Source Software for Predictive Simulation of Biological Motion". In: *Journal of Open Source Software* 4 (June 2019), p. 1421. DOI: [10.21105/joss.01421](https://doi.org/10.21105/joss.01421).
- [36] A.D. Georgoulis et al. "ACL injury and reconstruction: Clinical related in vivo biomechanics". In: *Orthopaedics & traumatology, surgery & research : OTSR* 96 (Oct. 2010), S119–28. DOI: [10.1016/j.otsr.2010.09.004](https://doi.org/10.1016/j.otsr.2010.09.004).
- [37] Rodrigo Goes et al. "Return to play after anterior cruciate ligament reconstruction". In: *Revista Brasileira de Medicina do Esporte* 26 (Nov. 2020), pp. 478–486. DOI: [10.1590/1517-8692202026062019_0056](https://doi.org/10.1590/1517-8692202026062019_0056).
- [38] Letha Griffin et al. "Noncontact Anterior Cruciate Ligament Injuries: Risk Factors and Prevention Strategies". In: *The Journal of the American Academy of Orthopaedic Surgeons* 8 (May 2000), pp. 141–50. DOI: [10.5435/00124635-200005000-00001](https://doi.org/10.5435/00124635-200005000-00001).
- [39] Dana Guy-Cherry et al. "Landing Styles Influences Reactive Strength Index without Increasing Risk for Injury". In: *Sports Medicine International Open* 02 (Feb. 2018), E35–E40. DOI: [10.1055/a-0608-4280](https://doi.org/10.1055/a-0608-4280).
- [40] Dana Guy-Cherry et al. "Landing Styles Influences Reactive Strength Index without Increasing Risk for Injury". In: *Sports Medicine International Open* 02 (Feb. 2018), E35–E40. DOI: [10.1055/a-0608-4280](https://doi.org/10.1055/a-0608-4280).
- [41] Dieter Heinrich, Antonie van den Bogert, and Werner Nachbauer. "Peak ACL force during jump landing in downhill skiing is less sensitive to landing height than landing position". In: *British Journal of Sports Medicine* 52 (June 2018), bjsports–2017. DOI: [10.1136/bjsports-2017-098964](https://doi.org/10.1136/bjsports-2017-098964).

- [42] Luis Hernandez et al. "The Biomechanics of ACL Injury: Progresses toward Prophylactic Strategies". In: *Critical reviews in biomedical engineering* 41 (Jan. 2013), pp. 309–321. DOI: [10.1615/CritRevBiomedEng.2014010460](https://doi.org/10.1615/CritRevBiomedEng.2014010460).
- [43] Timothy Hewett. "Stiff Landings Are Associated With Increased ACL Injury Risk in Young Female Basketball and Floorball Players: Letter to the Editor". In: *The American Journal of Sports Medicine* 45 (Mar. 2017), NP5–NP5. DOI: [10.1177/0363546517692761](https://doi.org/10.1177/0363546517692761).
- [44] Chang Jing et al. "Muscle Fatigue Analysis Using OpenSim". In: May 2017. ISBN: 978-3-319-58462-1. DOI: [10.1007/978-3-319-58463-8_9](https://doi.org/10.1007/978-3-319-58463-8_9).
- [45] Paul Jones, Lee Herrington, and Philip Graham-Smith. "Technique determinants of knee joint loads during cutting in female soccer players". In: *Human Movement Science* 42 (Aug. 2015). DOI: [10.1016/j.humov.2015.05.004](https://doi.org/10.1016/j.humov.2015.05.004).
- [46] Matthew Kelly. "An Introduction to Trajectory Optimization: How to Do Your Own Direct Collocation". In: *SIAM Review* 59.4 (2017), pp. 849–904. DOI: [10.1137/16M1062569](https://doi.org/10.1137/16M1062569). eprint: <https://doi.org/10.1137/16M1062569>. URL: <https://doi.org/10.1137/16M1062569>.
- [47] Matthew Kelly. "Transcription Methods for Trajectory Optimization: a beginners tutorial". In: (July 2017).
- [48] Hideyuki Koga et al. "Hip and Ankle Kinematics in Noncontact Anterior Cruciate Ligament Injury Situations: Video Analysis Using Model-Based Image Matching". In: *The American Journal of Sports Medicine* 46 (Oct. 2017), p. 036354651773275. DOI: [10.1177/0363546517732750](https://doi.org/10.1177/0363546517732750).
- [49] Joanna Kvist. "Rehabilitation Following Anterior Cruciate Ligament Injury". In: *Sports medicine (Auckland, N.Z.)* 34 (Feb. 2004), pp. 269–80. DOI: [10.2165/00007256-200434040-00006](https://doi.org/10.2165/00007256-200434040-00006).
- [50] Adam Kłodowski et al. "Merge of motion analysis, multibody dynamics and finite element method for the subject-specific analysis of cartilage loading patterns during gait: differences between rotation and moment-driven models of human knee joint". In: *Multibody System Dynamics* 37 (July 2015), pp. 1–20. DOI: [10.1007/s11044-015-9470-y](https://doi.org/10.1007/s11044-015-9470-y).
- [51] Mari Leppänen et al. "Stiff Landings Are Associated With Increased ACL Injury Risk in Young Female Basketball and Floorball Players". In: *The American journal of sports medicine* 45 (Sept. 2016). DOI: [10.1177/0363546516665810](https://doi.org/10.1177/0363546516665810).
- [52] Stefan Lindström. *Lectures on Engineering Mechanics: Statics and Dynamics*. June 2019. ISBN: 978-91-981287-4-1.
- [53] Austin Looney et al. "Bioaugmentation in the surgical treatment of anterior cruciate ligament injuries: A review of current concepts and emerging techniques". In: *SAGE Open* 8 (May 2020), pp. 1–13. DOI: [10.1177/2050312120921057](https://doi.org/10.1177/2050312120921057).

- [54] Marieswaran et al. "A Review on Biomechanics of Anterior Cruciate Ligament and Materials for Reconstruction". In: *Applied Bionics and Biomechanics* 2018 (May 2018), pp. 1–14. DOI: [10.1155/2018/4657824](https://doi.org/10.1155/2018/4657824).
- [55] Oishee Mazumder et al. "Musculoskeletal modeling to predict and reduce Anterior Cruciate Ligament injury during single leg drop jump activity: Synergistic muscle co-activation approach". In: vol. 2019. July 2019, pp. 4108–4112. DOI: [10.1109/EMBC.2019.8856321](https://doi.org/10.1109/EMBC.2019.8856321).
- [56] Alistair McBurnie, Thomas Dos'Santos, and Paul Jones. "Biomechanical Associates of Performance and Knee Joint Loads During A 70–90° Cutting Maneuver in Subelite Soccer Players". In: *Journal of Strength and Conditioning Research* Publish Ahead of Print (July 2019), p. 1. DOI: [10.1519/JSC.0000000000003252](https://doi.org/10.1519/JSC.0000000000003252).
- [57] Hossein Mokhtarzadeh et al. "Contributions of the Soleus and Gastrocnemius muscles to the anterior cruciate ligament loading during single-leg landing". In: *Journal of biomechanics* 46 (May 2013). DOI: [10.1016/j.jbiomech.2013.04.010](https://doi.org/10.1016/j.jbiomech.2013.04.010).
- [58] Hossein Mokhtarzadeh et al. "Muscle coordination during single-leg landing: Implications for ACL injuries". In: Feb. 2012.
- [59] Hossein Mokhtarzadeh et al. "The effect of leg dominance and landing height on ACL loading among female athletes". In: *Journal of Biomechanics* 60 (July 2017). DOI: [10.1016/j.jbiomech.2017.06.033](https://doi.org/10.1016/j.jbiomech.2017.06.033).
- [60] Hossein Mokhtarzadeh et al. "Understanding Anterior Cruciate Ligament Injury Due to Drop Landing: Effects of Different Landing Techniques and Muscles' Action at the Knee Joint". In: Aug. 2010. ISBN: 978-3-642-14514-8. DOI: [10.1007/978-3-642-14515-5_44](https://doi.org/10.1007/978-3-642-14515-5_44).
- [61] Andrew Monk et al. "Surgical versus conservative interventions for treating anterior cruciate ligament injuries". In: vol. 4. June 2014. DOI: [10.1002/14651858.CD011166](https://doi.org/10.1002/14651858.CD011166).
- [62] Kristin Morgan, Cyril Donnelly, and Jeffrey Reinbolt. "Elevated gastrocnemius forces compensate for decreased hamstrings forces during the weight-acceptance phase of single-leg jump landing: Implications for anterior cruciate ligament injury risk". In: *Journal of biomechanics* 47 (Sept. 2014). DOI: [10.1016/j.jbiomech.2014.08.016](https://doi.org/10.1016/j.jbiomech.2014.08.016).
- [63] Mark Mounts. "Physics Hypertextbook". In: *Choice* 44 (Jan. 1970), pp. 1946–1947.
- [64] Hamid Naghibi et al. "A novel approach for optimal graft positioning and tensioning in anterior cruciate ligament reconstructive surgery based on the finite element modeling technique". In: *The Knee* 27 (Feb. 2020). DOI: [10.1016/j.knee.2020.01.010](https://doi.org/10.1016/j.knee.2020.01.010).
- [65] Anup Nandy and Pavan Chakraborty. "A study on human gait dynamics: modeling and simulations on OpenSim platform". In: *Multimedia Tools and Applications* 76 (Oct. 2017). DOI: [10.1007/s11042-016-4033-7](https://doi.org/10.1007/s11042-016-4033-7).

- [66] Dung Nguyen, Sandra Shultz, and Randy Schmitz. "Landing Biomechanics in Participants With Different Static Lower Extremity Alignment Profiles". In: *Journal of athletic training* 50 (Feb. 2015). DOI: [10.4085/1062-6050-49.6.03](https://doi.org/10.4085/1062-6050-49.6.03).
- [67] Wenxin Niu et al. "Effect of Dropping Height on the Forces of Lower Extremity Joints and Muscles during Landing: A Musculoskeletal Modeling". In: *Journal of Healthcare Engineering* 2018 (July 2018), pp. 1–8. DOI: [10.1155/2018/2632603](https://doi.org/10.1155/2018/2632603).
- [68] Margareta Nordin and V.H. Frankel. *Basic Biomechanics of the Musculoskeletal System*. July 2013, pp. 1–454.
- [69] Shelby Peel et al. "Effects of Foot Rotation on ACL Injury Risk Variables During Drop Landing". In: *Journal of Science in Sport and Exercise* 2 (Jan. 2020). DOI: [10.1007/s42978-019-00051-3](https://doi.org/10.1007/s42978-019-00051-3).
- [70] Karim Khan Peter Brukner. "Brukner and Khan's clinical sports medicine : injuries". In: 2016. ISBN: 9781743761380.
- [71] Wolf Petersen and Thore Zantop. "Anatomy of the Anterior Cruciate Ligament with Regard to Its Two Bundles". In: *Clinical orthopaedics and related research* 454 (Feb. 2007), pp. 35–47. DOI: [10.1097/BLO.0b013e31802b4a59](https://doi.org/10.1097/BLO.0b013e31802b4a59).
- [72] Chadwick Prodromos et al. "A Meta-analysis of the Incidence of Anterior Cruciate Ligament Tears as a Function of Gender, Sport, and a Knee Injury–Reduction Regimen". In: *Arthroscopy: the journal of arthroscopic & related surgery: official publication of the Arthroscopy Association of North America and the International Arthroscopy Association* 23 (Jan. 2008), 1320–1325.e6. DOI: [10.1016/j.arthro.2007.07.003](https://doi.org/10.1016/j.arthro.2007.07.003).
- [73] Andrea Russo et al. "Sensory modulation of gait characteristics in human locomotion: a neuromusculoskeletal modeling study". In: (Dec. 2020). DOI: [10.1101/2020.12.17.423198](https://doi.org/10.1101/2020.12.17.423198).
- [74] Akira Saito et al. "Influence of the trunk position on knee kinematics during the single-leg landing: implications for injury prevention". In: *Sports Biomechanics* (Feb. 2020), pp. 1–14. DOI: [10.1080/14763141.2019.1691642](https://doi.org/10.1080/14763141.2019.1691642).
- [75] Gil Serrancolí et al. "Subject-Exoskeleton Contact Model Calibration Leads to Accurate Interaction Force Predictions". In: *IEEE Transactions on Neural Systems and Rehabilitation Engineering* PP (June 2019), pp. 1–1. DOI: [10.1109/TNSRE.2019.2924536](https://doi.org/10.1109/TNSRE.2019.2924536).
- [76] Yohei Shimokochi et al. "Changing sagittal plane body position during single-leg landings influences the risk of non-contact anterior cruciate ligament injury". In: *Knee surgery, sports traumatology, arthroscopy : official journal of the ESSKA* 21 (Apr. 2012). DOI: [10.1007/s00167-012-2011-9](https://doi.org/10.1007/s00167-012-2011-9).

- [77] Choongsoo Shin, Ajit Chaudhari, and Thomas Andriacchi. "Shin CS, Chaudhari AM, Andriacchi TP. The influence of deceleration forces on ACL strain during single-leg landing: a simulation study. *J Biomech.*40(5):1145-52". In: *Journal of biomechanics* 40 (Feb. 2007), pp. 1145–52. DOI: [10.1016/j.jbiomech.2006.05.004](https://doi.org/10.1016/j.jbiomech.2006.05.004).
- [78] Choongsoo Shin, Ajit Chaudhari, and Thomas Andriacchi. "Valgus Plus Internal Rotation Moments Increase Anterior Cruciate Ligament Strain More Than Either Alone". In: *Medicine and science in sports and exercise* 43 (Aug. 2011), pp. 1484–91. DOI: [10.1249/MSS.0b013e31820f8395](https://doi.org/10.1249/MSS.0b013e31820f8395).
- [79] Susan Sigward, Guilherme Cesar, and Kathryn Havens. "Predictors of Frontal Plane Knee Moments During Side-Step Cutting to 45 and 110 Degrees in Men and Women: Implications for Anterior Cruciate Ligament Injury". In: *Clinical Journal of Sport Medicine* 25 (Nov. 2015), pp. 529–534.
- [80] Nathaniel Skinner, Karl Zelik, and Arthur Kuo. "Subjective valuation of cushioning in a human drop landing task as quantified by trade-offs in mechanical work". In: *Journal of Biomechanics* 48 (Apr. 2015). DOI: [10.1016/j.jbiomech.2015.04.029](https://doi.org/10.1016/j.jbiomech.2015.04.029).
- [81] GK Smith, DN Biery, and TP Gregor. "New concepts of coxofemoral joint stability and the development of a clinical stress-radiographic method for quantitating hip joint laxity in the dog". In: *Journal of the American Veterinary Medical Association* 196.1 (1990), 59–70. ISSN: 0003-1488. URL: <http://europepmc.org/abstract/MED/2295555>.
- [82] Yu Song et al. "Trunk motion and anterior cruciate ligament injuries: a narrative review of injury videos and controlled jump-landing and cutting tasks". In: *Sports Biomechanics* (Mar. 2021), pp. 1–19. DOI: [10.1080/14763141.2021.1877337](https://doi.org/10.1080/14763141.2021.1877337).
- [83] Dimitar Stanev and Konstantinos Moustakas. "Modeling musculoskeletal kinematic and dynamic redundancy using null space projection". In: (Jan. 2019). DOI: [10.1371/journal.pone.0209171](https://doi.org/10.1371/journal.pone.0209171).
- [84] Dimitar Stanev and Konstantinos Moustakas. "Proprioceptive modeling of the peripheral nervous system as an extension to the biomechanics musculoskeletal models". In: June 2015. DOI: [10.13140/RG.2.1.4044.8160](https://doi.org/10.13140/RG.2.1.4044.8160).
- [85] Dimitar Stanev and Konstantinos Moustakas. "Simulation of Constrained Musculoskeletal Systems in Task Space". In: *IEEE Transactions on Biomedical Engineering* 65 (Feb. 2018), pp. 307–318. DOI: [10.1109/TBME.2017.2764630](https://doi.org/10.1109/TBME.2017.2764630).
- [86] Dimitar Stanev and Konstantinos Moustakas. "Stiffness Modulation of Redundant Musculoskeletal Systems". In: *Journal of Biomechanics* (Jan. 2019). DOI: [10.1016/j.jbiomech.2019.01.017](https://doi.org/10.1016/j.jbiomech.2019.01.017).

- [87] Dimitar Stanev et al. "ACL Reconstruction Decision Support Personalized Simulation of the Lachman Test and Custom Activities". In: *Methods of Information in Medicine* 55 (Dec. 2015), pp. 98–105. DOI: [10.3414/ME14-02-0022](https://doi.org/10.3414/ME14-02-0022).
- [88] Dimitar Stanev et al. "Real-Time Musculoskeletal Kinematics and Dynamics Analysis Using Marker- and IMU-Based Solutions in Rehabilitation". In: *Sensors* 21 (Mar. 2021), p. 1804. DOI: [10.3390/s21051804](https://doi.org/10.3390/s21051804).
- [89] Dai Sugimoto et al. "Specific exercise effects of preventive neuromuscular training intervention on anterior cruciate ligament injury risk reduction in young females: Meta-analysis and subgroup analysis". In: *British journal of sports medicine* 49 (Dec. 2014). DOI: [10.1136/bjsports-2014-093461](https://doi.org/10.1136/bjsports-2014-093461).
- [90] Phillis Teng, Kah Fai Leong, and Pui Kong. "Influence of Foot-Landing Positions at Initial Contact on Knee Flexion Angles for Single-Leg Drop Landings". In: *Research Quarterly for Exercise and Sport* 91 (May 2020), pp. 316–325. DOI: [10.1080/02701367.2019.1669765](https://doi.org/10.1080/02701367.2019.1669765).
- [91] Scott L. Delp Thomas K. Uchida. *Biomechanics of Movement: The Science of Sports, Robotics, and Rehabilitation*. Cambridge, Massachusetts : The MIT Press, 2021. ISBN: 9780262044202.
- [92] Thomas Uchida et al. "Stretching Your Energetic Budget: How Tendon Compliance Affects the Metabolic Cost of Running". In: *PLOS ONE* 11 (Mar. 2016), e0150378. DOI: [10.1371/journal.pone.0150378](https://doi.org/10.1371/journal.pone.0150378).
- [93] Brian Umberger. "Stance and swing phase costs in human walking". In: *Journal of the Royal Society, Interface / the Royal Society* 7 (Mar. 2010), pp. 1329–40. DOI: [10.1098/rsif.2010.0084](https://doi.org/10.1098/rsif.2010.0084).
- [94] Brian Umberger, KARIN GERRITSEN, and Philip Martin. "A Model of Human Muscle Energy Expenditure". In: *Computer methods in biomechanics and biomedical engineering* 6 (May 2003), pp. 99–111. DOI: [10.1080/1025584031000091678](https://doi.org/10.1080/1025584031000091678).
- [95] Dmitry Verniba et al. "The analysis of knee joint loading during drop landing from different heights and under different instruction sets in healthy males". In: *Sports Medicine - Open* 3 (Jan. 2017). DOI: [10.1186/s40798-016-0072-x](https://doi.org/10.1186/s40798-016-0072-x).
- [96] Andreas Wächter and Lorenz Biegler. "On the Implementation of an Interior-Point Filter Line-Search Algorithm for Large-Scale Nonlinear Programming". In: *Mathematical programming* 106 (Mar. 2006), pp. 25–57. DOI: [10.1007/s10107-004-0559-y](https://doi.org/10.1007/s10107-004-0559-y).
- [97] Tadashi Yasuda et al. "Hip rotation as a risk factor of anterior cruciate ligament injury in female athletes". In: *The Journal of Physical Fitness and Sports Medicine* 5 (Mar. 2016), pp. 105–113. DOI: [10.7600/jpfsm.5.105](https://doi.org/10.7600/jpfsm.5.105).

- [98] Raye Chen-Hua Yeow, Peter Lee, and James Goh. "An investigation of lower extremity energy dissipation strategies during single-leg and double-leg landing based on sagittal and frontal plane biomechanics". In: *Human movement science* 30 (Mar. 2011), pp. 624–35. DOI: [10.1016/j.humov.2010.11.010](https://doi.org/10.1016/j.humov.2010.11.010).
- [99] Kwon YH. *Center of pressure (GRF application point) 1998*. URL: <http://www.kwon3d.com/theory/grf/cop.html>.